Numerical modeling and characterization of high-temperature superconductor coils for electrical machines

Zur Erlangung des akademischen Grades eines

DOKTORS DER INGENIEURWISSENSCHAFTEN (Dr.-Ing.)

von der KIT-Fakultät für Elektrotechnik und Informationstechnik des
Karlsruher Instituts für Technologie (KIT)

angenommene

DISSERTATION

von

M.Eng. Carlos Roberto Vargas Llanos
geb. in Aragua, Venezuela

Tag der mündlichen Prüfung:	24.04.2023
Hauptreferent:	Apl. Prof. Dr. Francesco Grilli
Korreferent:	Prof. Dr. Frédéric Sirois

Acknowledgements

First, I would like to thank my supervisor apl. Prof. Dr. Francesco Grilli, for providing excellent guidance and supervision during the development of this work. This research would not have been possible without his continuous support and invaluable discussions, which helped me on a personal and professional level. He always encouraged me to conduct high-quality research and to participate in international conferences and workshops, which allowed me to be a better researcher. I would also like to thank Prof. Dr.-Ing. Mathias Noe, whose assistance and advice helped me to accomplish the goals of this thesis and to improve the quality of the work.

I am also grateful for all the support from the technical staff, researchers, and fellow Ph.D. students of the KIT ITEP. Thanks to Dustin Kottonau, Fabian Schreiner, and Andrej Kudymow for their valuable discussions about AC losses and critical current measurement techniques. Thanks to Uwe Walschburger, Holger Fillinger, and Johann Willms for their great support to gather all the necessary tools and resources that made possible the work in the laboratory. Thanks to Yingzhen Liu and Roland Gyuraki for helping me when I arrived at the institute.

Finally, I would like to express my sincere gratitude to my family. I owe everything to my parents Cipriano Vargas and Dilia Llanos, whose teachings and love created the man that I am today. I learned from them that nothing is impossible for a smart and hardworking person. I would also like to thank my wife for all her support and patience.

Kurzfassung

Die aktuelle Kapazität von Hochtemperatursupraleitern (HTS) hat verschiedene Anwendungen in elektrischen Energiesystemen gefördert. Im Bereich der erneuerbaren Energien haben der weltweit steigende Energieverbrauch und die Energiewende die Forschung zu supraleitenden Generatoren für Windturbinen stark vorangetrieben, wo HTS die Leistungsdichte in Richtung besserer Multi-Megawatt-Lösungen erhöhen könnten. Trotz ihres Gleichstromwiderstands von Null können bei HTS unter zeitlich wechselndem Transportstrom oder Magnetfeld Verluste eintreten. Diese Verluste können bei den meisten HTS-Anwendungen entscheidend sein, da sie den Bedarf an Kühlleistung und den Gesamtwirkungsgrad der Maschine beeinflussen. Daher sind die Modellierung und Charakterisierung von Spulen für die weitere Entwicklung von supraleitenden Systemen von zentraler Bedeutung. Aus diesem Grund konzentriert sich diese Arbeit auf die Untersuchung von HTS-Spulen, um die technologischen Herausforderungen zukünftiger elektrischer HTS-Maschinen zu bewältigen.

Da die Modellierung und Analyse von supraleitenden Spulen ein entscheidender Teil der Entwurfsphase der meisten HTS-Komponenten ist, wird ein neuer 3D-Modellierungsansatz entwickelt, der auf der Homogenisierung der T-A-Formulierung basiert. Die Modellierungsmethodik ermöglicht eine einfachere Implementierung in kommerzieller Software (COMSOL Multiphysics) im Vergleich zu der derzeit verfügbaren 3D-H-Homogenisierung. Zunächst wird der Modellierungsansatz mit 2D-Simulationen und AC-Verlustmessungen in ringförmigen Spulen validiert. Dann wird er zur Abschätzung der Verluste und zur Analyse des elektromagnetischen Verhaltens einer Racetrack-, einer Saddle- und einer Twisted-Spule verwendet.

Es werden mehrere Entwürfe supraleitender Generatoren für Windturbinenanwendungen modelliert und untersucht. Besonderes Interesse gilt der Verringerung der Wechselstromverluste in der HTS-Statorwicklung, wobei drei Hauptstrategien untersucht werden: nicht planare Spulen, Reduktion der Bandbreite und Temperaturreduktion. Es wird eine neue Statorwicklungsanordnung vorgeschlagen, mit der eine 80 prozentige Reduzierung der HTS-Spulenverluste und eine bessere Verteilung der Wärmeverluste in den Spulen im Vergleich zur Standard-Racetrack-Spulenanordnung erreicht wird.

Zuletzt werden zwei Racetrack-Spulen für elektrische Maschinenanwendungen hergestellt und charakterisiert. Jede Spule besteht aus 2 mm dickem Band verschiedener Hersteller, S-Innovations und Fujikura. Als erstes wird die Abhängigkeit des kritischen Stroms der Bänder von der Amplitude und Richtung des Magnetfelds gemessen. Danach werden 2D- und 3D-Modelle entwickelt, um die Induktivität, den kritischen Strom und die AC-Transportverluste in den Spulen abzuschätzen. Diese Charakterisierung wird durch experimentelle Arbeiten ergänzt, die einen direkten Vergleich von Messungen und Simulationsergebnissen ermöglichen. Der Entwurf, die Konstruktion, die Kalibrierung und der Test eines Aufbaus zur Messung der AC-Transportverluste in supraleitenden Hochtemperaturspulen auf der Grundlage eines kalorimetrischen Ansatzes (Boil-off-Methode) werden vorgestellt. Das verdampfte Kryogen (Stickstoff), das mit der Energiedissipation zusammenhängt, wird mit Hilfe eines 3D-gedruckten Blasensammlers aufgefangen, der das Gas in einen Flusssensor leitet. Ein Box-inside-a-Box-Ansatz wird verwendet, um die Messkammer mit einer kryogenen Umgebung zu umgeben. Dieser Ansatz ermöglicht die Umleitung der Wärmeübertragung aus der Umgebung in eine Zwischenzone (Raum zwischen äußerer und innerer Box). Da diese Zwischenzone unter kryogenen Temperaturen arbeitet, werden das Rauschen und die Wärmeübertragung im inneren Teil des Aufbaus reduziert. Eine statistische Analyse der Ergebnisse auf der Grundlage eines Standardlastzyklus, des Mittelwerts und der Berechnung der Standardabweichung ermöglicht es, die Variabilität der Messungen zu bewerten und die Ergebnisse als Mittelwert und Unsicherheitsbereich auszudrücken. Die Kalibrierung und Reproduzierbarkeit der Messungen werden mit einer Reihe von Widerständen unter verschiedenen Bedingungen und während verschiedener Wochen überprüft, und die Wechselstrom-Transportverluste werden gemessen und mit den Ergebnissen der 3D-Simulation verglichen.

Abstract

The current capacity of high-temperature superconductors (HTS) has encouraged several applications in electric power systems. In the renewable energy sector, the increasing worldwide energy consumption and energy transition have driven strong research on superconducting generators for wind turbine applications, where HTS could increase power density towards better multi-megawatt solutions. Despite their zero direct current (DC) resistance, HTS experience energy dissipation under time-changing transport current or magnetic field. These losses can be decisive in most HTS applications since they influence the cooling power requirements and the overall efficiency of the machine. Therefore, the modelling and characterization of coils are essential for the further development of superconducting devices. For this reason, this thesis is focused on the study of HTS coils to face the technological challenges of future HTS electrical machines.

Since the modelling and analysis of superconducting coils is a crucial part of the design stage of most HTS devices, a new 3D modelling approach based on the homogenization of the T-A formulation is developed. The modelling methodology allows an easier implementation in commercial software (COMSOL Multiphysics) in comparison with the currently available 3D H homogenization. First, the modelling approach is validated with 2D simulations and AC loss measurements in circular coils. Then, it is used to estimate losses and to analyse the electromagnetic behaviour of racetrack, saddle, and twisted coils.

Several designs of superconducting generators for wind turbine applications are modelled and studied. Particular attention is given to the reduction of AC losses in the stator HTS winding, where three main strategies are investigated: non-planar coils, tape width and temperature reduction. A new stator winding arrangement is proposed, which achieves an 80 % reduction in HTS coil losses and a better distribution of the dissipation in the coils in comparison with the standard racetrack coil configuration.

Two racetrack coils for electrical machine applications are manufactured and characterized. Each coil is made with 2 mm tape from different manufacturers, S-Innovations and Fujikura. The dependence of the critical current of the tapes on the magnetic field amplitude and direction is measured. Then, 2D and 3D models are developed to estimate the inductance, critical current, and AC transport losses in the coils. This characterization is complemented with experimental work, which allows a comparison between measurements and simulation results.

The design, construction, calibration and test of a setup to measure transport AC losses in high-temperature superconducting coils based on a calorimetric approach (boil-off method) are presented. The evaporated cryogen (nitrogen) related to the dissipation of energy is collected by using a 3D-printed bubble collector that guides the gas into a flow sensor. A box-inside-a-box approach is used to surround the measurement chamber with a cryogenic environment. This approach allows re-directing the heat transfer from the surroundings into an intermediate zone (space between external and internal box). Since this intermediate zone operates under cryogenic temperatures, the noise and the heat transfer in the internal part of the setup are reduced. A statistical analysis of the results based on a standard load cycle, average value, and standard deviation calculations allows assessing the variability in the measurements and expressing the results as average value and uncertainty range. The reproducibility of the measurements is verified with a set of resistors under different conditions and during different weeks. Finally, the AC transport losses in the coils are measured and compared with the 3D simulation results.

Contents

Acronyms and symbols

Acronyms

AC	Alternating current
CC	Curvilinear coordinates
DC	Direct current
DOF	Degrees of freedom
FEM	Finite element method
GdBCO	Gadolinium barium copper oxide
GF	Glass-filled
GUI	Graphical user interface
HTS	High-temperature superconductor
LCR	Inductance, capacitance and resistance
LED	Light-emitting diode
PA	Polyamide
REBCO	Rare-earth barium copper oxide
YBCO	Yttrium barium copper oxide
2D	Two-dimensional

3D	Three-dimensional

Latin symbols and variables

A, $\vec{A}$	Magnetic vector potential
A_q	Area
B, $\vec{B}$	Magnetic flux density
B_x, B_y, B_z	Components of the magnetic flux density in the Cartesian coordinate system
$B_\perp$	Magnetic flux density component perpendicular to the wide face of the tape
$B_{\parallel}$	Magnetic flux density component parallel to the wide face of the tape
$e_\perp$	Unit vector in the direction perpendicular to the wide face of the tape
$e_{\parallel}$	Unit vector in the direction parallel to the wide face of the tape
e_t	Unit vector in the direction tangential to the winding
E, $\vec{E}$	Electric field
E_x, E_y, E_z	Components of the electric field in the Cartesian coordinate system
$E_{\mathbf{c}}$	Critical electric field
f	Frequency
F	Average flow measurement
H, $\vec{H}$	Magnetic field strength

$\hat{\imath}$	Unit vector in the direction of the x axis in the Cartesian coordinate system
I	Current
$I_{\mathbf{peak}}$	Peak current
$I_{\mathbf{c}}$	Critical current
I_k	Current flowing through the kth conductor.
J, $\vec{J}$	Current density
J_x, J_y, J_z	Components of the current density in the Cartesian coordinate system
$J_{\mathbf{c}}$	Critical current density
J_k	Current density in the kth conductor.
J_s, $\vec{J}_s$	Scaled current density in the homogenization of the T-A formulation in 3D
L	Thickness
$\vec{n}$	Unit vector in the direction normal to the wide face of the tape
n_x, n_y, n_z	Components of the unit vector in the normal direction to the wide face of the tape in the Cartesian coordinate system
n	Power law exponent
P	AC loss measurement
$\dot{Q}$	Heat flow
$R_{\mathbf{warm}}$	Resistance measured at ambient temperature
$R_{\mathbf{cold}}$	Resistance measured at 77 K (liquid nitrogen temperature at atmospheric pressure)

r_1	Internal radius of the curved part of the racetrack coil
r_2	External radius of the curved part of the racetrack coil
S_k	Cross-section of the kth conductor.
t	Time
T, $\vec{T}$	Current vector potential
T_x, T_y, T_z	Components of the current vector potential in the Cartesian coordinate system
T_1, T_2	Values of the current vector potential at the edges of the tape after applying the thin strip approximation
$T_{\mathbf{amb}}$	Ambient temperature
$T_{\mathbf{op}}$	Operating temperature
y_0	Half of the length of the straight part of the racetrack coil
$\hat{z}$	Unit vector in the direction of the z axis

Greek symbols and variables

δ	Thickness of the superconducting tape
δP	Uncertainty in the measurement of AC losses
δF	Uncertainty in the measurement of flow
$\eta_{\mathbf{c}}$	Carnot efficiency
θ	Integral of the temperature-dependent thermal conductivity
λ	Thickness of a cell unit in the homogenization of the T-A formulation in 3D
μ	Permeability of the material

μ_0	Vacuum permeability
σ	Standard deviation
$\sigma_{\textbf{flow}}$	Standard deviation in the flow measurements
$\hat{\rho}$	Unit vector in the radial direction in the cylindrical coordinate system
ρ	Resistivity of the material
$\rho_{\textbf{HTS}}$	Resistivity of the high-temperature superconductor
$\hat{\phi}$	Unit vector in the tangential direction in the cylindrical coordinate system

1 Introduction

The continuous increment in the global energy demand, and world ambient temperature, has encouraged the development of sustainable energy sources [1] [2]. As a result, constant technological improvement has arisen in the electric generation sector based on wind energy, as one of the key technologies in the energy transition [3], [4], [5]. In particular, the trends in generators for wind turbine applications are toward more powerful, lighter, and compact designs. This can positively impact the cost of the mast, foundation, transport, and installation of the turbine, especially in the offshore area [6], [7], [8], [9].

The current capacity of high-temperature superconductors (HTS) can help to increase the power density of the generators in wind turbine applications to achieve better multi-megawatt solutions [10], [11], [12], [13]. The electrical properties of HTS have already inspired several applications in multiple fields such as electrical machines [14], fault current limiters [15], magnets for scientific research [16], energy storage [17], and transmission [18]. Therefore, different research and development projects have been carried out to develop new superconducting generators for wind turbine applications [19], [20], [21], [22]. Despite their zero DC resistance, HTS experience energy dissipation when they are exposed to changes in the current or magnetic field [23]. As a consequence, most of these applications involve only HTS in the rotor (field) winding, which is assumed to carry DC-current. In recent years, the interest in the development of fully superconducting generators for wind turbine applications has increased [24], [25]. These new designs aim to use the high current capacity of HTS further to achieve an extra size and weight reduction [26], [27]. However, the complex electromagnetic dynamic in the stator HTS winding can produce significant losses. Moreover, HTS must be cooled at cryogenic temperatures to take advantage of its superconducting properties. Under such operating conditions, the cooling efficiency can increase the cooling power requirements. Therefore, the losses in the superconductor can be decisive for the design and construction of HTS based devices [28].

This work is focused on the numerical modelling and characterization of high-temperature superconducting coils for electrical machines, which allows the development of HTS stator coils for wind turbine generator applications. The thesis starts with the description of a new 3D modelling approach developed to study coils with complex geometries based on the homogenization of the T-A formulation in 3D. This is a necessary tool that encourages the research and development of coils with complex shapes to face the technological challenges of different HTS applications. Then, AC losses are estimated in the stator winding of a generator for a wind turbine applications by considering different configurations. Particular attention is given to AC loss reduction in the stator winding, where a new coil arrangement is proposed. A setup for calorimetric measurements of AC transport losses in HTS coils is designed, constructed, calibrated and tested; which complements the characterization of HTS coils for AC applications. The main contributions of this thesis are the conceptual development of innovative stator HTS windings that allows a major AC loss reduction, as well as the development of simulation and measurement tools that enable the characterization of coils with complex geometries. The thesis is organized into chapters as follows.

Chapter 2 introduces a brief review of superconductivity, HTS and losses in HTS. It also provides a small introduction to superconducting electrical machines for wind turbine applications. This chapter allows identifying the coils and superconductors under study and set the basis for the following sections.

Chapter 3 describes the two most popular formulations used to model HTS, which are used to model the superconducting coils and stator winding of electrical machines in this work. This chapter presents the development of the homogenization of the T-A formulation in 3D, as well as its validation against measurements and 2D simulation results. Different case studies are presented in this section based on four different geometries: circular, racetrack, saddle and twisted coils.

Chapter 4 presents the modelling of superconducting electrical generators for wind turbine applications. The modelling approach is introduced first, and the properties of the materials are described. Then, the electromagnetic behaviour of two designs (with and without iron teeth) is analyzed, and AC losses are estimated in the HTS stator coils. These calculations are complemented with an AC loss reduction study, where three main methodologies are used: non-planar coils, tape width and temperature reduction.

Chapter 5 introduces the basic design and construction of test coils. Measurements of the critical current of the tape that is used in the coils are presented in this section for different magnetic field amplitudes and directions. Two coils are fabricated with tape provided by two different manufacturers. The inductance of the coils is estimated with 3D FEM models and compared with measurements done with an LCR (inductance (L), capacitance (C) and resistance (R)) meter.

Chapter 6 presents measurements of the critical current of the coils. The resistance of the soldered point between the tape and the connector is measured. The results are compared with 2D simulations based on the methodology presented in [29].

Chapter 7 shows the design, construction, calibration and test of a calorimetric setup to measure AC transport losses. The coils fabricated and characterized in Chapters 5 and 6 are modelled by using the homogenization of the T-A formulation in 3D. The transport losses are estimated and compared with 2D modelling results. Then, the setup to measure AC transport losses in these coils is designed and constructed. The setup is calibrated and the reproducibility of the results is verified. Finally, AC transport losses are measured in both coils and compared with the simulation results.

All the main contributions and conclusions of this thesis are summarized in Chapter 8.

2 High-temperature superconductors and AC losses

This chapter introduces a brief review of superconductivity, which allows understanding basic concepts and identifying the type of superconductors under study. It also provides a short explanation of the losses in high-temperature superconductors and a small review of superconducting electrical machines, which set the basis and scope of the work presented in the following chapters.

2.1 Introduction to superconductivity

Superconductivity can be described as a property observed in specific materials to conduct direct current (DC) without resistance or losses. It was discovered by a Dutch physicist (H.K. Onnes) in 1911. He observed that the resistance of mercury abruptly decreased to a non-measurable value when the sample was cooled at 4.2 K [30] [31]. However, this is not the only macroscopic behaviour that defines superconductivity. In 1933, W. Meissner and R. Ochsenfeld discovered that a superconductor completely expels the magnetic field from its interior by generating a screening current on its surface that opposed the external magnetic field, which is called nowadays Meissner effect [32]. The absolute field expulsion happens regardless the magnetic field is applied before or after the material becomes superconductor, which represents a clear difference between a superconductor and a perfect conductor.

The temperature at which the resistance decreased to zero in a superconductor is known as critical temperature. Two additional concepts must be added to describe better the operational limits of the superconducting properties. These are the critical current density and the critical magnetic field. These three variables are related to each other and define a critical surface, which is characteristic of the superconducting material [33]. The superconducting state exists only below this surface.

In 1957 A. A. Abrikosov predicted the behaviour of a new kind of superconductors [34]. These type II superconductors have a more complex behaviour in the presence of magnetic field. Below a first critical magnetic field (named B_{c1}), the material exhibits the Meissner effect and expels completely the magnetic field. However, above B_{c1} very small normal zones (cores) start to appear. The flux inside the cores is produced by a vortex of current that circulates around the core. The current around one normal core interacts with the current of the neighboring cores with repulsion, which results in a regular periodical hexagonal array known as fluxon lattice [35]. If the magnetic field is further increased above B_{c2}, the superconductor finally goes into the normal state. The space between B_{c1} and B_{c2} is known as mixed state.

2.1.1 High-temperature superconductors

Another major discovery in superconductivity happened in 1986 when J. G. Bednorz and K. A. Müller discovered superconducting materials with critical temperatures above $30\,\mathrm{K}$ [36]. Some of these new type II high-temperature superconductors have critical temperatures above the boiling point of nitrogen, which allows liquid nitrogen cooling [37].

The superconducting tapes considered in the next chapters of this thesis are made of rare-earth barium copper oxide (REBCO), which is an HTS superconductor. The mathematical models presented in these chapters describe the macroscopic behaviour of the superconducting material. A good agreement can be found between these models and experimental results, which allows a good prediction of the macroscopic behaviour of the REBCO tapes in HTS devices.

2.1.2 Losses in high-temperature superconductors

The magnetic field in type II superconductors in the mixed state exists through flux vortices, as mentioned in section 2.1. If there is a transport current through the sample, there will be a Lorentz force that will cause movement of the flux vortices. The movement of flux induces an electromotive force that generates a current in the normal cores, which causes dissipation (losses). However, the flux vortices are pinned in the defects of the material. These pinning forces avoid the movement of flux and allow transporting current without dissipation in DC conditions (current and magnetic field constant in time).

If the type II superconductor in the mixed state is exposed to time changing current or magnetic field, a movement of the flux inside the superconductor happens to follow this time-changing excitation. This movement of flux induces a voltage and creates dissipation in the normal cores.

Analytical solutions have been developed to estimate losses in single tapes [38], [39] and infinite stacks of superconducting tapes [40], [41], [42], under transport current or externally applied magnetic field. Appendix A presents a brief summary of the development of two applications with user interfaces in Matlab to estimate losses in infinite stacks of tapes based on analytical solutions. These kinds of resources allow the user to estimate AC losses quickly and to improve the understanding of the AC losses in HTS by modifying basic parameters such as critical current and separation between tapes. However, these expressions do not fully represent the real behaviour of the superconducting coils located in the stator of an electrical machine. For this reason, numerical methods are necessary to study the AC losses in this kind of application. In this work, the finite element method (FEM) based on Maxwell equations is used to study the behaviour of HTS electrical machines and estimate the AC losses in superconducting coils.

2.2 Superconducting electrical generators for wind turbine applications

The increasing worldwide energy consumption and renewable generation have driven strong research on superconducting generators for wind turbine applications, where HTS can increase power density. This improvement can be seen in figure 2.1, which shows a comparison of direct drive permanent magnet synchronous generators, partially superconducting generators (HTS rotor winding and copper stator winding), and fully superconducting generators. In these plots, the mass and volume of multiple designs are presented as a function of the nominal power. The graphs are built with the data presented in [43], [44] and they represent the current state of the art of generators for wind turbine applications.

Since the HTS experience losses under a time-changing current or magnetic field, most of the superconducting generator applications involve only HTS coils in the rotor (field) winding, which carries DC-current in synchronous machines. However, the interest in the development of fully superconducting generators for wind turbine applications has increased [24], [25]. These designs aim to use the current capacity of HTS in the stator to achieve an extra size and weight reduction [26], [27]. Nevertheless, the complex and dynamic electromagnetic environment of the stator of an electrical machine can cause significant losses in the superconducting windings. Moreover, the HTS coils have to operate under cryogenic temperatures to keep the superconducting properties. Under this condition, the cooling efficiency has a great impact on the refrigeration power required to handle the energy dissipation. Therefore, the losses in the superconductor can be decisive for the design and construction of superconducting coils in electrical machines. This work is focused on the numerical modeling and characterization of high-temperature superconducting coils for wind turbine applications. Particular attention is given to the AC loss estimation and reduction in the stator coils.

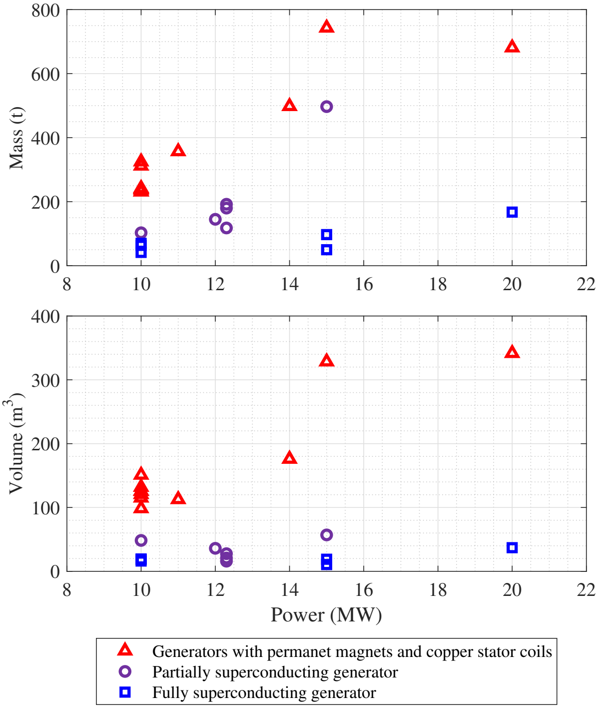

Figure 2.1: Mass and volume of direct drive permanent magnet synchronous generators, partially superconducting generators (HTS rotor winding and copper stator winding), and fully superconducting generators as a function of the nominal power. The graphs are built with the data presented in [43], [44], where some of the volumes are estimated based on the outer diameter and active length of the generators.

3 Modelling of high-temperature superconducting coils

The modeling and analysis of superconducting coils is an essential task in the design stage of most devices based on high-temperature superconductors (HTS). These calculations allow verifying basic estimations and assumptions, proposing improvements, and computing quantities that are not easy to calculate with an analytical approach. For instance, the estimation of losses in HTS is fundamental during the design stage since losses can strongly influence the cooling system requirements and operating temperature. Several analytical solutions have been developed to estimate losses in HTS tapes [42]. However, these solutions are only valid under specific operating conditions such as AC transport current or applied uniform magnetic field. Therefore, they can not be directly used to estimate losses in most superconducting machines and equipment. For these reasons, numerical models are typically used to analyze the electromagnetic behavior and estimate losses in the HTS tapes and coils. Different methods can be used for this purpose, for example: finite-element [45], integral equation [46], variational [47] or spectral [48] methods. Among the various finite-element models, two formulations have become very popular. The first one is based on the magnetic field strength ($\vec{H}$) and has been already used to study numerous applications [49]. The second one was introduced in [50] and is based on the current vector potential ($\vec{T}$), used previously in [45] for AC calculations, and magnetic vector potential ($\vec{A}$). This T-A formulation is mostly used to analyze superconducting layers by applying a thin strip approximation. The approximation allows a reduction of dimensions that decreases the number of degrees of freedom and computation time.

Most of the FEM-based models used to study superconducting devices are 2D. They usually represent the cross-section of an infinite long or axisymmetric arrangement. In the case of racetrack coils, the end effects are frequently not considered. Moreover, complex geometries and operating conditions such as saddle coils and twisted stacks of tapes under an external magnetic field can not be analyzed with a 2D model. For these reasons, several efforts were made for the development of tools and methodologies that allow 3D modeling of HTS coils [51], [52], [53], [54], [55]. As part of these efforts, in 2014 the 3D H homogenization was introduced with the model of a racetrack coil [56]. However, this approach requires the implementation of high resistivity layers in the homogenized domain. Five years later, the 3D homogenized T-A formulation was proposed by Huang et al. [57], who used it to calculate the AC transport losses of HTS racetrack coils. In this chapter, the current knowledge is expanded by using the homogenization of the T-A formulation for the simulation of complex 3D HTS coils. The new modeling approach is based on normal vectors defined by a local curvilinear coordinate system that considers the continuous shape and position of the tape and coil. Therefore, this general definition allows an easy implementation of the model despite the complexity of the geometry.

The derivation of the governing equations of the T-A and H formulations is briefly described first in this chapter. Particular emphasis is given to the implementation of the normal vectors in the T-A formulation, and how they can be defined in a commercial software (COMSOL Multiphysics). Then, the proposed homogenization of the T-A formulation in 3D is described and a set of case studies is presented. The modelling approach is validated first with transport AC loss measurements in circular coils, and simulation results from 2D T-A axisymmetric models. Subsequently, the racetrack coil presented in [56] is modelled with the proposed homogenization of the T-A formulation in 3D, and a comparison with the homogenization of the H formulation in 3D is introduced. Finally, the model and analysis of more complex geometries such as saddle and twisted coils are presented.

3.1 T-A Formulation

The first applications of the T-A formulation to study superconducting devices by using FEM were introduced in [50], [58]. These works presented the T-A formulation as an efficient approach to model HTS tapes with a high aspect ratio. This formulation of Maxwell's equations couples the current vector potential $\vec{T}$ and magnetic vector potential $\vec{A}$, which are defined by the current density $\vec{J}$ and magnetic flux density $\vec{B}$:

$$\vec{J} = \nabla \times \vec{T} \tag{3.1}$$

$$\vec{B} = \nabla \times \vec{A}. \tag{3.2}$$

The magnetic vector potential is computed in all the domains under study by using Maxwell-Ampere's law (μ is the permeability of the material):

$$\nabla \times (\frac{1}{\mu}\nabla \times \vec{A}) = \vec{J}. \tag{3.3}$$

The magnetic flux density is computed based on the magnetic vector potential and equation (3.2). The current vector potential is calculated only in the superconducting domain by using Maxwell-Faraday's law:

$$\nabla \times (\rho_{\mathrm{HTS}}\nabla \times \vec{T}) = -\frac{\partial \vec{B}}{\partial t}. \tag{3.4}$$

The current density in the superconducting domain is computed based on the current vector potential and equation (3.1). Then, $\vec{J}$ can be used to calculate $\vec{A}$, which couples equation (3.3) and equation (3.4).

The resistivity of the superconducting material is typically modeled with a power-law $\vec{E} - \vec{J}$ relation [59]:

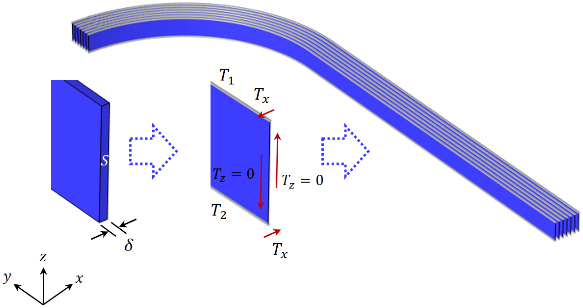

Figure 3.1: T-A formulation in 3D. $\vec{T}$ is computed only in the superconducting domain (depicted in blue) while $\vec{A}$ is computed everywhere. The thickness of the tape is collapsed into a superconducting layer and the current is enforced by giving proper values of T at the edges of the tape [60].

$$\rho_{\text{HTS}} = \frac{E_\text{c}}{J_\text{c}(\vec{B})} \left| \frac{\vec{J}}{J_\text{c}(\vec{B})} \right|^{n(\vec{B})-1} . \tag{3.5}$$

In this work, the magnetic field dependence of $n(\vec{B})$ has not been considered. Therefore, constant values of n have been used in all the simulations.

An approximation is done by considering that in the tapes under study the superconducting layer (for instance rare-earth barium copper oxide/REBCO tapes) has a very large width-to-thickness ratio. Therefore, we can collapse the thickness of the tape (δ) as shown in figure 3.1. As a consequence, the current is able to flow only in a superconducting sheet and $\vec{T}$ is always perpendicular to this sheet. For this reason, the current vector potential can be expressed as $T \cdot \vec{n}$ ($\vec{n}$ is a unit vector perpendicular to the superconducting layer) [50].

The transport current can be imposed by setting the boundary conditions for T at the edges of the tape, as it is shown in equations (3.6) and (3.7):

$$I = \iint_S \vec{J} \cdot \mathrm{d}\vec{s} = \iint_S (\nabla \times \vec{T}) \cdot \mathrm{d}\vec{s} = \oint_{\partial S} \vec{T} \cdot \mathrm{d}\vec{l} \tag{3.6}$$

$$I = (T_1 - T_2)\delta. \tag{3.7}$$

Therefore, the transport current can be imposed with a non-unique combination of values for T_1 and T_2, such as: $T_2 = 0$ and $T_1 = I/\delta$, $T_1 = \frac{I}{2\cdot\delta}$ and $T_2 = -\frac{I}{2\cdot\delta}$ or any other values that express the same condition [61].

In all the calculations presented in this chapter, the order of the elements used for discretization is the one described in [60] (linear elements for $\vec{T}$ and quadratic elements for $\vec{A}$) to avoid possible spurious oscillations.

3.2 Homogenization of the T-A formulation in 3D

The homogenization technique assumes that the superconducting tapes that are wound in coils can be represented by an anisotropic bulk that can reproduce the overall electromagnetic behavior of the coil [62]. This allows reducing the number of degrees of freedom and the computation time. The technique was implemented by using the T-A formulation in 2D in [60], [63]. Therefore, we follow a similar approach to extend the homogenization into the 3D analysis of superconducting coils.

The procedure is summarized in figure 3.2. We start from the arrangement of tapes modeled in the T-A 3D formulation as sheets and define a cell unit around them (with the same height of the superconducting tape and thickness Λ). The main characteristics of the tape will be impressed in this cell unit to transform the stack of tapes into a block. For the $\vec{A}$ calculation, the scaled current in the homogenized bulk is defined as:

$$\vec{J}_s = \frac{\delta}{\Lambda}\vec{J}. \tag{3.8}$$

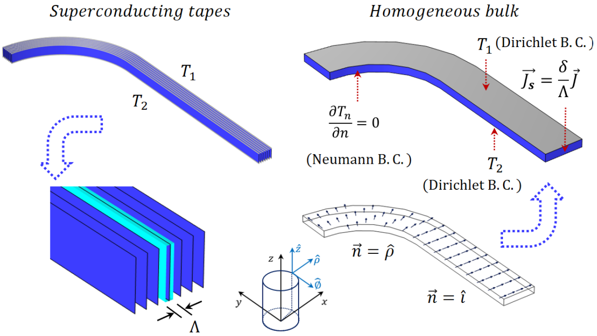

Figure 3.2: T-A homogenization in 3D. The superconducting sheets are replaced by a homogeneous block. The scaled current density $\vec{J_s}$ is introduced as a source term and boundary conditions T_1 and T_2 are applied to the upper and lower boundaries.

In principle, the homogenization makes use of Maxwell's equations in the same way as the 3D T-A formulation. Therefore, we keep the thin strip approximation of the tape that allows reducing the current vector potential into a scalar quantity. This means that even if the tapes are replaced by a homogeneous bulk, the current can only flow in the plane parallel to the original superconducting sheets. For example, if we refer to the straight part of the coil shown in the zoom in the bottom left corner of figure 3.2, the current has only have J_y and J_z components and the current vector potential only has a T_x component. The new homogenized block can be seen as a highly compressed group of superconducting tapes. In the curve regions of this example, more general expressions are necessary to compute $\vec{J}$ and $\vec{T}$. Therefore, we can assume $\vec{n} = \begin{bmatrix} n_x \\ n_y \\ n_z \end{bmatrix}$ and express equation (3.1) as:

$$\begin{bmatrix} J_x \\ J_y \\ J_z \end{bmatrix} = \begin{bmatrix} \frac{\partial(T \cdot n_z)}{\partial y} - \frac{\partial(T \cdot n_y)}{\partial z} \\ \frac{\partial(T \cdot n_x)}{\partial z} - \frac{\partial(T \cdot n_z)}{\partial x} \\ \frac{\partial(T \cdot n_y)}{\partial x} - \frac{\partial(T \cdot n_x)}{\partial y} \end{bmatrix}. \tag{3.9}$$

The magnetic vector potential is calculated in all the domains and we solve the current vector potential only in the superconducting domain by using Maxwell-Faraday's law:

$$\begin{bmatrix} \frac{\partial(E_z)}{\partial y} - \frac{\partial(E_y)}{\partial z} \\ \frac{\partial(E_x)}{\partial z} - \frac{\partial(E_z)}{\partial x} \\ \frac{\partial(E_y)}{\partial x} - \frac{\partial(E_x)}{\partial y} \end{bmatrix} \cdot \vec{n} + \begin{bmatrix} \frac{\partial(B_x)}{\partial t} \\ \frac{\partial(B_y)}{\partial t} \\ \frac{\partial(B_z)}{\partial t} \end{bmatrix} \cdot \vec{n} = 0, \tag{3.10}$$

where $\vec{n}$ can be easily determined in the T-A formulation because it is the vector perpendicular to the superconducting sheet. Therefore, it is usually defined by default in commercial software like COMSOL Multiphysics. However, once the homogenization technique is applied and the stack of tapes is replaced by the homogenized domain, it is not easy to define $\vec{n}$ inside the bulk. We have no longer a reference surface from which we can define the normal vector. A similar issue can be found in the 2D T-A homogenization when complex (rotated or curved) cross-sections are modeled in 2D. In this work, we present two alternatives to address this issue. First, we can analytically calculate $\vec{n}$ by following the geometrical path of the tape before homogenization. If the tape is parallel to the $y - z$ plane then:

$$\vec{n} = \hat{\imath} = \begin{bmatrix} 1 \\ 0 \\ 0 \end{bmatrix}. \tag{3.11}$$

If the tape is wound in a circular shape with the center in the origin, then $\vec{n}$ will be parallel to the radial vector in cylindrical coordinates $\hat{\rho}$:

$$\vec{n} = \hat{\rho} = \begin{bmatrix} \frac{x}{\sqrt{x^2+y^2}} \\ \frac{y}{\sqrt{x^2+y^2}} \\ 0 \end{bmatrix}. \tag{3.12}$$

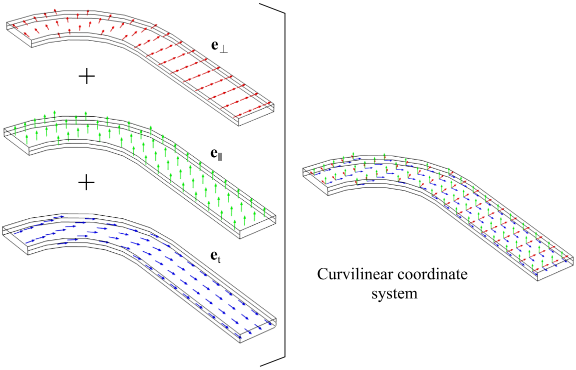

Figure 3.3: Curvilinear coordinate (CC) system example for the geometry shown in figure 3.2. The CC system is defined based on the surface/boundaries of the 3D domain, which allows the definition of the base (unit) vectors of the system. These vectors can be used as references of the directions perpendicular to the wide face of the tape ($e_\perp$), parallel to the wide face of the tape ($e_{||}$), and tangential to the winding direction (e_t).

The normal vector can also be analytically defined by domains to represent more complex geometries as the one shown in the right corner of figure 3.2. In this case, $\vec{n} = \hat{\imath}$ in the straight section and $\vec{n} = \hat{\rho}$ in the circular one. However, these analytic expressions can become very complex if we change the geometry of the coil, for example by introducing twisted or curved non-circular sections. Therefore, a second and more general solution is a curvilinear coordinate system defined in the superconducting domain. This approach creates a local coordinate system with curved lines that follow the shape of the superconducting domain [64], as it can be observed in figure 3.3 for the geometry described in figure 3.2. The unit vectors of this local coordinate system can be defined for all possible geometries and used as normal, parallel and tangential vectors. This approach can be implemented in COMSOL Multiphysics by using the curvilinear coordinate module.

Finally, the boundary conditions need to be established to solve our problem. The homogenized bulk represents a densely packed group of HTS sheets. Each one of these sheets should transport the same current as its original counterpart [60]. Therefore, Dirichlet boundary conditions are applied to the boundaries that correspond to the edges of the tape, as expressed in equation (3.7). Neumann boundary conditions are applied to the boundaries that correspond to the flat side of the tape:

$$\frac{\partial T_n}{\partial n} = 0, \tag{3.13}$$

as it is explained in the diagram presented in figure 3.2. In this equation, T_n is the normal component of T at the boundary calculated as $T_n = n_x \cdot T_x + n_y \cdot T_y + n_z \cdot T_z$.

It is worth pointing out that this modelling approach is valid under low-frequency (transport current and magnetic field) conditions. Since the methodology is based on homogenization and thin strip approximation, the detailed structure of the HTS tape is not modelled. For high-frequency conditions, the different layers and materials of the tape play a key role in the estimation of AC losses [65], [66], [67]. Therefore, the homogenization of the T-A formulation in 3D might no longer be accurate for AC loss estimations.

3.3 H Formulation

This formulation of the Maxwell equations is based on the magnetic field strength ($\vec{H}$). The first applications of the H formulation for modelling superconductors were introduced by Kajikawa *et al* [68] and Pecher *et al* [69]. Then, Brambilla *et al* [70] and Hong *et al* [71] independently implemented it in commercial software (Comsol Multiphysics). The H formulation has been used to study numerous HTS applications in 2D and 3D [49], [72]. Therefore, it represents one of the most popular options to model HTS by using FEM.

In this formulation, Maxwell-Faraday equation is solved by considering the magnetic field strength components as state variables:

$$\nabla \times \vec{E} = -\frac{\partial(\mu\vec{H})}{\partial t}. \tag{3.14}$$

The electric field ($\vec{E}$) can be substituted by $\vec{E} = \rho\vec{J}$ (ρ is the resistivity of the material and $\vec{J}$ is the current density). Finally, the current density can also be replaced by Maxwell-Ampere equation ($\nabla \times \vec{H} = \vec{J}$), which results in the governing equation of the formulation:

$$\nabla \times (\rho\nabla \times \vec{H}) = -\frac{\partial(\mu\vec{H})}{\partial t}. \tag{3.15}$$

The resistivity of the superconducting material can be modelled with a power-law $\vec{E} - \vec{J}$ relation as shown in equation (3.5) [59]. The current in each conductor can be imposed with integral constraints [70] [73]

$$I_k(t) = \int_{S_k} J_k(t)\, dS, \tag{3.16}$$

and appropriate boundary conditions allow imposing an external magnetic field with or without transport current. In equation (3.16), $I_k(t)$ represents the current, $J_k(t)$ is the current density, and S_k is the cross-section of the kth conductor.

The homogenization technique can be applied in this formulation for 2D [62] and 3D [56] simulations too. Since the H formulation has already been used and validated in multiple applications, it is used in this chapter to validate the racetrack coil simulation results presented in the following section.

3.4 Case studies

This section introduces a group of case studies modelled and analyzed with the proposed homogenization of the T-A formulation in 3D. The complexity of the geometry is increasing in each case by starting with circular coils and finishing with a geometry that has no straight sections, only curved and twisted parts. The first simulations validate the modelling approach, and the last ones represent

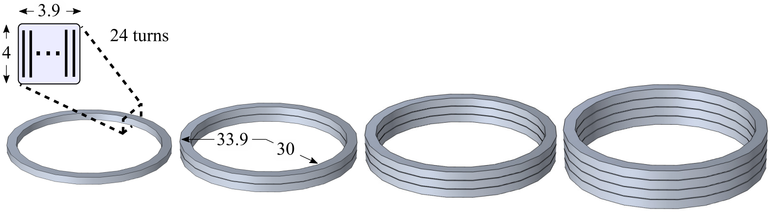

Figure 3.4: Geometry and dimensions of the circular coils under study [74]. The circular coils are made with 24 turns of a $4\,\mathrm{mm}$ HTS tape. Four arrangements of coils are analyzed, one individual coil and groups of two, three and four coils stacked one on top of each other. The separation between the coils is $0.3\,\mathrm{mm}$. All the dimensions are in millimeters.

some of the most complex 3D HTS coils modelled with time dependent 3D FEM simulations.

3.4.1 Circular coils

The first analyzed cases with the homogenization of the T-A formulation in 3D are the circular coils presented in [47]. This geometry can be studied with an axisymmetric model. Therefore, the losses and the overall electromagnetic behavior can be compared between the homogenization of the T-A formulation in 3D and the 2D T-A formulation. In addition to this comparison, we can validate the model with the AC losses measurements shown in [47].

The geometry and dimensions of the coils are presented in figure 3.4. Four configurations of coils are studied, one individual coil and groups of two, three, and four coils stacked one on top of each other. They are built with a $4\,\mathrm{mm}$ REBCO tape that has a $1\,\mu\mathrm{m}$ superconducting layer. The critical current of the tape at $77\,\mathrm{K}$ and self-field is $128\,\mathrm{A}$. More information about the coils and measurements can be found in [47].

The critical current density dependence on the magnetic field magnitude and direction is modeled as [75]:

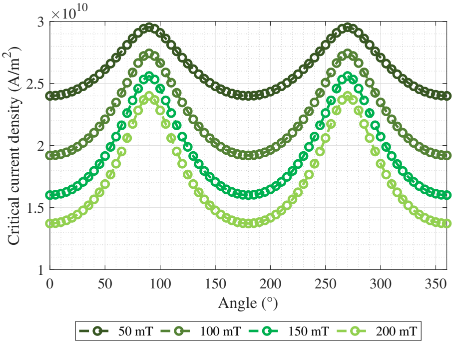

Figure 3.5: Critical current density behavior of the HTS tape used to model the circular coils for an external magnetic field magnitude of $50\,\mathrm{mT}$, $100\,\mathrm{mT}$, $150\,\mathrm{mT}$ and $200\,\mathrm{mT}$. An angle of 0° represents a field perpendicular to the wide face of the tape; an angle of 90° represents a parallel one.

$$J_\mathrm{c}(B_{||}, B_\perp) = \frac{J_\mathrm{c0}}{\left[1 + \sqrt{(B_{||}k)^2 + B_\perp^2}/B_\mathrm{c}\right]^b}. \tag{3.17}$$

In this equation, $B_{||}$ and $B_\perp$ are the parallel and perpendicular components (to the wide face of the tape) of the magnetic flux density. The parameters J_c0, k, b, and B_c are equal to $3.2 \times 10^{10}\,\mathrm{A\,m^{-2}}$, 0.25, 1, and $150\,\mathrm{mT}$. The behavior of the critical current density can be better appreciated in figure 3.5, where $J_\mathrm{c}(B_{||}, B_\perp)$ is plotted by considering four different magnetic field magnitudes with different directions.

Since the resistivity of the superconductor is several orders of magnitude lower than the resistivity of other materials in the tape, the HTS tape is modelled in 2D by considering only the superconducting layer surrounded by a homogeneous medium with a resistivity of $1\,\Omega\,\mathrm{m}$ and vacuum permeability. This approximation is valid for low-frequency applications [66]. The resistivity of the superconducting material is modeled with a power-law $\vec{E} - \vec{J}$ relation (equation (3.5)) and $n = 25$.

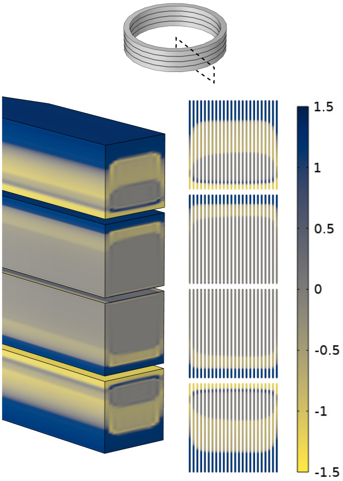

Figure 3.6: Normalized current density (J/J_c) in four circular coils stacked one on top of each other for transport current (55 A peak) when the current is equal to zero and after the first half period of the sinusoidal cycle. A comparison between the T-A 3D homogenization and a T-A 2D axisymmetric solution is presented when the current is equal to zero and after half cycle.

Figure 3.6 shows the behavior of the normalized current density (J/J_c) for the four coils configuration and peak transport current of $55\,\mathrm{A}$. The current distribution inside the coils is very similar between the 3D T-A homogenization and the 2D T-A axisymmetric model when the current is equal to zero and after the first half period of the sinusoidal cycle. A similar behavior was observed for other instants in time and circular coil arrangements.

Figure 3.7 presents a comparison of the losses measured in [47] and estimated with the 3D T-A homogenization and 2D T-A axisymmetric models for all the configurations shown in figure 3.4. The results of the homogenization of the T-A formulation in 3D are in good agreement with the 2D axisymmetric model (maximum error lower than $6.23\,\%$ for all the configurations) and measurement results (maximum error lower than $35\,\%$ for all the configurations) for all the studied current ranges. These results validate the modelling approach and allow

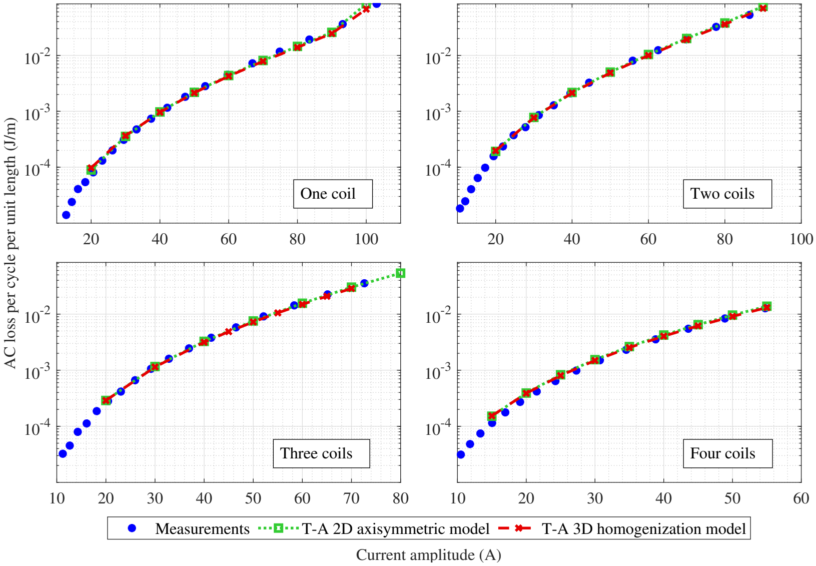

Figure 3.7: Comparison of the estimation of losses due to AC transport current in the circular coils by using the T-A 2D axisymmetric, the homogenization of the T-A formulation in 3D, and measurements. The calculation was done for a single coil and groups of two, three, and four coils stacked one on top of each other.

moving forward to model more complex geometries that can not be investigated in 2D.

3.4.2 Racetrack coil

The racetrack coil presented in [56] is studied in this subsection. This kind of coil is used for example in the rotor of superconducting electrical machines for wind turbine applications [76]. It has two straight and two round parts as shown in figure 3.8, where the dimensions of the racetrack coil under analysis are also given.

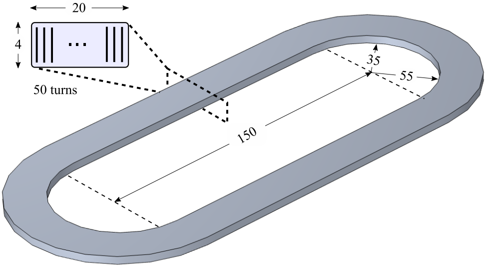

Figure 3.8: Geometry and dimensions of the racetrack coil under study [56]. The coil is made with 50 turns of HTS tape, which creates a stack $4\,\mathrm{mm}$ wide and $20\,\mathrm{mm}$ height in the cross-section of the coil. All the dimensions are in millimeters.

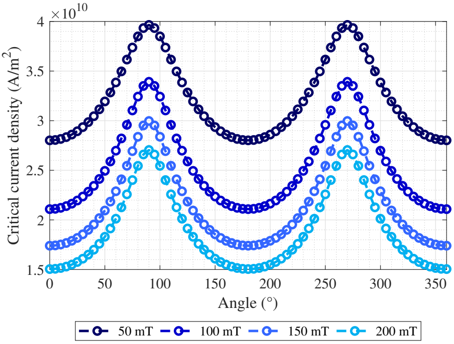

Figure 3.9: Critical current density behavior of the HTS tape used to model the racetrack, saddle and twisted coils for an external magnetic field magnitude of $50\,\mathrm{mT}$, $100\,\mathrm{mT}$, $150\,\mathrm{mT}$ and $200\,\mathrm{mT}$. An angle of 0° represents a field perpendicular to the wide face of the tape; an angle of 90° represents a parallel one.

In this study, the tape is modelled by considering the same parameters presented in [56]. This allows a direct comparison with the well-established 3D H homogenization. The critical current density dependence on the magnetic field amplitude and direction is described by equation 3.17, where the parameters J_{c0}, k, B_c and b have the following values $49\,\mathrm{GA\,m^{-2}}$, 0.275, $32.5\,\mathrm{mT}$ and 0.6. This is a tape with a critical current of $160\,\mathrm{A}$ at $77\,\mathrm{K}$ self-field. The behavior of the critical current density of the tape can be better appreciated in figure 3.9, where

$J_{\mathrm{c}}(B_{||}, B_{\perp})$ was plotted by considering four different magnetic field magnitudes with different directions. The HTS resistivity is modeled with a power-law $\vec{E} - \vec{J}$ relation (equation (3.5)) and $n = 21$.

The critical current of the coil was estimated by using the methodology described in [29], in a 2D model that represents the cross-section of the middle of the straight part of the coil. This technique has been applied before to estimate the critical current of HTS coils [77], and it presents two criteria to calculate the critical current. The maximum criterion indicates that I_{c} is the current that produces a voltage drop per unit length equal to the critical electric field ($E_{\mathrm{c}} = 1\,\mathrm{\mu V\,cm^{-1}}$) in at least one turn of the coil. On the other hand, the average criterion indicates that I_{c} is the current that produces an average voltage drop in the coil (all turns) equal to E_{c} [29]. The critical current of the coil is $98.3\,\mathrm{A}$ and $99.9\,\mathrm{A}$, by considering the maximum and average criteria respectively.

The parallel ($B_{||}$) and perpendicular ($B_{\perp}$) components of the magnetic flux density were calculated by domain. In the circular section, they were computed as $B_{||} = B_z$ and $B_{\perp} = B_{\rho}$, by assuming that the circular region is centered at the origin. In the straight section, they were computed as $B_{||} = B_z$ and $B_{\perp} = B_x$, by considering that the straight region is parallel to the y axis. Similar to what was done in [56], one-eighth of the coil was modelled by taking advantage of the symmetries.

The normal vector ($\vec{n}$) can be defined in this case by domain by following the original path of the superconducting tape or by using a curvilinear coordinate system, as it was mentioned in section 3.2. Both approaches were used in this case study and identical results were obtained. For this reason, the results of the model that uses the curvilinear coordinate system are the only ones presented in this subsection.

The normalized current density in the cross-sections of the racetrack coil for AC transport current ($f = 50\,\mathrm{Hz}$ and $I_{\mathrm{peak}} = 100\,\mathrm{A}$) without external magnetic field, when the current is equal to zero (after the first half period of the sinusoidal cycle), is shown in figure 3.10. In this figure, a comparison of the normalized current density distribution obtained with the 3D H homogenization and 3D T-A

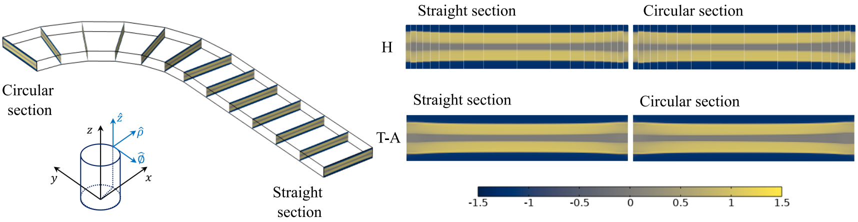

Figure 3.10: Normalized current density (J/J_c) in one-fourth of the racetrack coil for AC transport current ($f = 50$ Hz and $I_{\text{peak}} = 100$ A) when the current is equal to zero, after the first half period of the sinusoidal cycle. A zoom in the middle of the circular section and the straight section of the racetrack coil is shown on the right, where a comparison between the 3D H and T-A homogenization results is presented.

homogenization is presented at the middle of the straight and circular sections. The current density distribution obtained by using the 3D T-A homogenization is in good agreement with the one computed with the 3D H homogenization. The small differences close to the edges can be related to the considerations and assumptions made in the implementation of the homogenization of the T-A and H formulations in 3D. The implemented T-A formulation is based on a thin strip approximation that constraints the current to flow only in the plane parallel to the flat face of the tape (it does not allow current sharing between tapes or subdomains of the homogenized coil) and allows reducing the current vector potential $\vec{T}$ to a scalar quantity. However, it can not properly consider the influence of the magnetic field parallel to the superconducting tape [50]. Moreover, the currently available 3D homogenization of the H formulation [56] can not prevent current sharing between tapes or subdomains of the homogenized coil. The current inside the homogenized domain can move freely in any direction, which does not represent the behavior of a coil with turn-to-turn insulation. For this reason, it requires the implementation of high resistivity layers, which discretize the homogenized domain to minimize current sharing between tapes (subdomains). This approach requires as many divisions as necessary to reflect the real behavior of the coil. Therefore, it does not represent an optimal solution. Moreover, these necessary separations in the geometry constrain the mesh in the 3D homogenization of the H formulation. For instance, no coarser mesh is feasible because a discretization

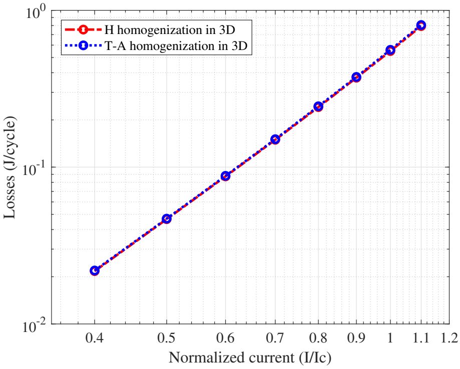

Figure 3.11: Estimation of losses in the racetrack coil due to AC transport current ($f = 50\,\mathrm{Hz}$) as a function of the current amplitude by using the T-A 3D homogenization and the H 3D homogenization.

with high resistivity layers is necessary to match the behavior of the model with the behavior of the coil with turn-to-turn insulation.

The current density distribution is similar along the coil. There is only a small difference between the middle of the straight and circular sections when the current is close to its maximum value, as it was reported in [56]. Figure 3.11 shows the losses due to AC transport current estimated with the 3D T-A homogenization model. The results are in good agreement with the 3D H homogenization calculation for all the studied current values, with a maximum relative error lower than $2\,\%$.

The homogenization of the T-A formulation in 3D has two main benefits. First, the computation time is lower in comparison with the homogenization of the H formulation in 3D. In the case of the racetrack coil, the calculation is three to four times faster with the T-A formulation. However, a direct comparison between these two models is not easy. Since the mesh in the 3D H homogenization is constrained by the geometrical discretization with high resistivity layers to minimize current sharing between subdomains, the mesh of the 3D H homogenization is finer than the mesh of the 3D T-A homogenization. If the same mesh is used in both cases, the degrees of freedom and computation time of the T-A formulation model are much higher than the H model. This behavior can be related to the number of state variables to be solved (H formulation H_x, H_y, H_z and T-A formulation A_x, A_y, A_z, and T) and type of elements used in each case (linear curl elements in the H formulation and quadratic elements for A and linear elements for T in the T-A formulation) [73], [60]. Nevertheless, the mesh of the H formulation is not an optimal solution for the T-A model, since the same results can be achieved with the homogenization of the T-A formulation in 3D with a coarser mesh. Therefore, a fair comparison between the T-A and H homogenization in 3D is not trivial and is still missing. The second advantage of the 3D T-A homogenization is that it is relatively easy to implement. In particular, it does not require 2D integral constraints or high resistivity zones to prevent current sharing between subdomains of different groups of tapes. This restriction, which is quite tricky to implement in the 3D H homogenization [56], is included in the essence of the T-A homogenization by applying the thin strip approximation which constraints the current to flow in the plane parallel to the tape and allows reducing the current vector potential to a scalar quantity. Moreover, the proposed normal vector approach (based on a curvilinear coordinate system definition) allows simulating any geometrical arrangement. Therefore, it represents an effective and practical tool for the analysis of coils with complex geometries.

3.4.3 Saddle coil

Since the modeling technique was already validated in the previous section, we can proceed with the analysis of more complicated geometries that are currently being investigated for the development of superconducting devices.

The third case of study is a saddle coil. This is a non-planar coil with two straight and two curved parts, which allow a $90°$ rotation of the cross-section between the middle of the circular and the straight region. The geometry and dimensions of the coil are presented in figure 3.12. Only one-fourth of the coil was modeled by taking advantage of the symmetries. As it was done in the previous section, the critical current was estimated with a 2D model by following the procedure

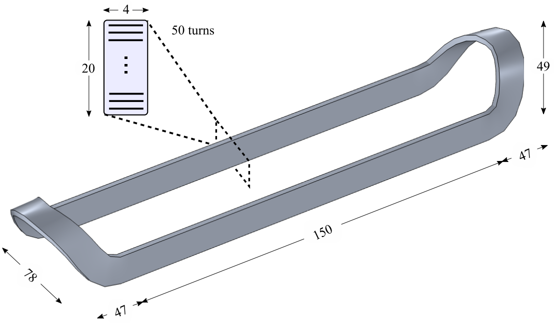

Figure 3.12: Geometry and dimensions of the saddle coil under study. The coil is made with 50 turns of HTS tape, which creates a stack $4\,\mathrm{mm}$ wide and $20\,\mathrm{mm}$ height in the cross-section of the coil. All the dimensions are in millimeters.

described in [29]. The critical current of the coil is $99.8\,\mathrm{A}$ by considering the average criterion.

The geometry of the saddle coil is more complex than the racetrack coil. Moreover, the ratio of the coil dimension to the HTS conductor generates a problem with a large number of degrees of freedom. Therefore, a compromise between mesh density (which influences the computation time) and accuracy must be found. In the simulations presented in this section, a quadrilateral mesh with 36 elements along the tape width and 10 elements along the stack height is used in the cross-section of the coil. Free tetrahedral mesh is used in the surrounding air domain and the whole geometry has 16322 elements in total, which results in 230898 degrees of freedom.

This type of coil is used in the magnet sector and was proposed for the rotor and stator of superconducting electrical machines, where a proper inclination of the straight section can lead to a significant reduction in AC losses [78], [79], [80]. Two operating conditions are analyzed in this section, AC transport current with and without AC externally applied magnetic field.

- *AC transport current without magnetic field*

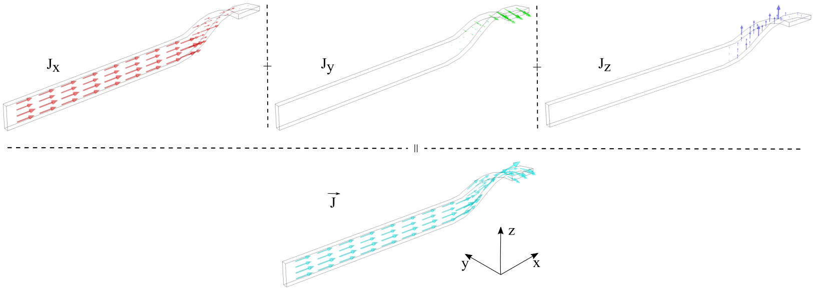

Figure 3.13: Distribution of the current components inside the saddle coil when the current reaches the maximum value. On the top of the figure and from left to right: x-component (J_x), y-component (J_y) and z-component (J_z). The total current is depicted in light blue arrows at the bottom.

The AC transport current operating condition is easier to analyze for this complex geometry. Therefore, it was chosen as the first step in the analysis of the coil. Since this is a non-planar coil, the current vector has x-component, y-component and z-component (figure 3.13). In the middle of the straight section, the current flows parallel to the x-axis. The curved section works as a transition zone for the current vector from the x-direction to the y-direction, by following the winding and position of the tapes. Due to the complex behavior of the current density ($\vec{J}$) in 3D geometries, the cartesian components (J_x, J_y, J_z) are not suitable for representation purposes. A possible way to overcome this problem is to use the norm of $\vec{J}$. However, it would not be possible to appreciate the two fronts of currents in opposite directions during the AC cycle. Therefore, the dot product between the current density vector and the tangential vector parallel to the winding direction ($\vec{e}_t$) is used in this case:

$$\frac{\vec{J} \cdot \vec{e}_t}{J_{\mathrm{c}}(B_{\|}, B_{\perp})}. \tag{3.18}$$

The dot product between this unit vector, parallel to the longitudinal direction of the tape, and the current density keeps the same module and

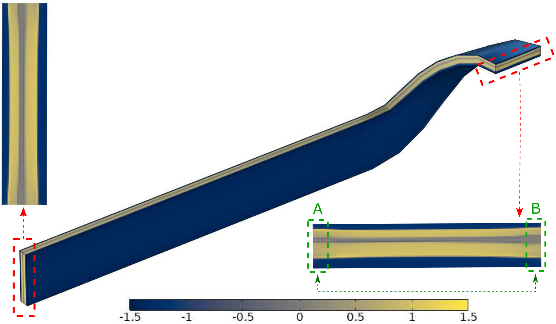

Figure 3.14: Normalized current density in the saddle coil computed with the 3D T-A homogenization model, for AC transport current ($f = 50\,\mathrm{Hz}$ and $I_{\mathrm{peak}} = 100\,\mathrm{A}$) when the current is equal to zero, and after the first half period of the sinusoidal cycle. The current density is normalized with the critical current density by using equation (3.18) to reflect the two fronts of current (positive and negative) in the direction tangential to the winding.

direction of $\vec{J}$, by having a positive/negative value when the current density is in the same/opposite direction of $\vec{e}_t$. The parallel and perpendicular (to the wide face of the tape) components of the magnetic field required for the local computation of $J_c(B_{\|}, B_{\perp})$ can also be calculated in a more general expression with the dot product between the magnetic field and the other two unit (base) vectors associated to the definition of the curvilinear coordinate system:

$$B_{\|} = \vec{B} \cdot \vec{e}_{\|} \tag{3.19}$$

$$B_{\perp} = \vec{B} \cdot \vec{e}_{\perp}. \tag{3.20}$$

Figure 3.14 presents the current density behavior in the coil for an AC transport current with a peak value of 100 A and frequency $f = 50\,\mathrm{Hz}$, when the current is equal to zero, and after the first half period of the sinusoidal cycle. The current density penetration and behavior are very similar in the middle of the straight and circular sections. There is only

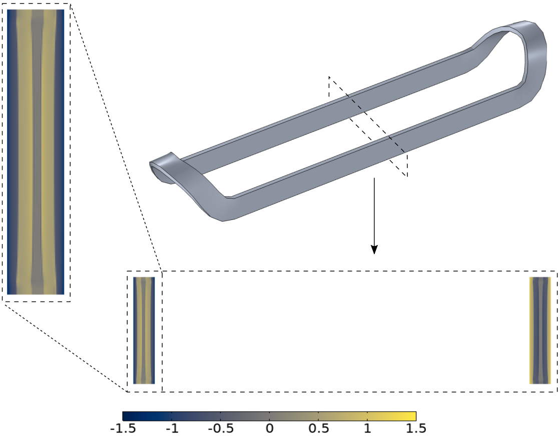

Figure 3.15: Normalized current density in the middle of the straight section of the saddle coil computed with the 2D T-A homogenization model, for AC transport current ($f = 50$ Hz and $I_{\text{peak}} = 100$ A) when the current is equal to zero, and after the first half period of the sinusoidal cycle.

a very small difference between the inner and the outer part of the curved section, indicated with green arrows as A and B in figure 3.14. This small difference is an effect of the self-field of the coil, which tends to be higher inside the coil than outside. According to these results, a 2D model that represents the middle of the straight section of the saddle coil can provide a good approximation of the current density behavior and a first estimation of the AC losses. This bi-dimensional model is simpler, faster, and easier to implement; and is commonly used to have first estimations of important parameters such as AC losses and magnetic field. Therefore, a 2D model was built to verify whether this assumption is valid for the proposed case study.

Figure 3.15 shows the current density behavior obtained with the 2D model that represents the middle of the straight section of the coil, for the same operating point and condition used in figure 3.14. The current density behavior is similar between the 2D and 3D models for the straight part of the coil. In the curved section, there is a small difference. As mentioned

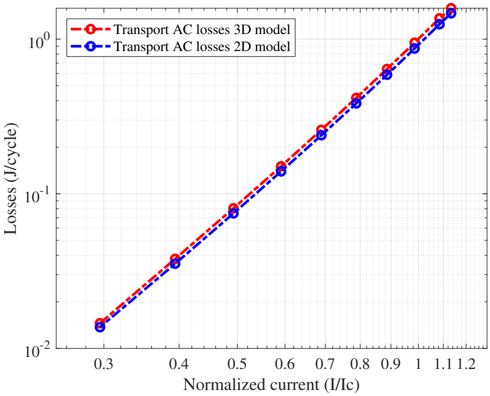

Figure 3.16: AC transport losses comparison in the saddle coil between the 3D T-A homogenization and the 2D T-A homogenization model that considers the cross-section of the middle of the straight part of the coil.

before, this difference is related to the self-field in 3D, which is a result of the interaction of the different parts (straight and curved) of the coil and can not be taken into account by a 2D model.

Figure 3.16 presents the behavior of the AC transport losses calculated with the T-A 3D and 2D homogenized models. The losses estimated with both models are in good agreement for all the range of current amplitudes under analysis, with a maximum relative difference of $8.4\,\%$. The small differences in the current density in the curved section do not have a meaningful impact on the AC transport losses. These differences vanish in the behavior of the whole coil, where the straight part behavior is dominant in the AC transport losses. This effect can be related to the length of the straight section in comparison with the curved one. For this reason, the 2D approximation can not be directly extrapolated to more curved and complex geometries. These results confirm the aforementioned hypothesis. The 2D model can be used as a first estimation of important parameters such as AC transport current losses for this specific case. However, the magnetic field around the coils in most of the practical applications is a combination of self-field and interaction with the environment. This yields a more complex operating condition that a 2D model can not fully predict.

- *AC transport current and AC external magnetic field*

  In this sub-section, the behavior of the saddle coil in the case of AC transport current (with a peak value of $100\,\mathrm{A}$ and frequency $f = 50\,\mathrm{Hz}$) and AC external magnetic field is analyzed. The external magnetic field is uniform, sinusoidal ($100\,\mathrm{mT}$ in magnitude and frequency $f = 50\,\mathrm{Hz}$) and applied in the z-direction, in phase with the magnetic field produced by the coil. This can be seen as the magnetic field produced by the rotor of an electrical machine that reaches one of the stator superconducting coils. However, the magnetic field in the stator of a superconducting electrical machine is more complex than the presented operating condition. In an electrical machine, the magnetic field changes around the stator and is not necessarily sinusoidal in time (it depends on the properties of the materials, the machine and the coil design) [80]. Therefore, the case presented in this subsection is a simplified version of a more complex operating condition, which allows us to study the behavior of the coil with AC transport current and AC external magnetic field. The analysis is not intended to predict the behavior of the coil in an electrical machine environment.

  Figure 3.17 presents a diagram of the applied magnetic field in the coil. The external magnetic field is depicted with dashed blue arrows and the self field of the coil with black continuous arrows. The transport current direction inside the coil is represented with red arrows. Since the external magnetic field is in the z-direction and in phase with the self-field of the coil, we can expect a higher magnetic field magnitude in the inner part (where the external and self field are in the same direction) and lower in the outer part of the coil (where the external and self field are in opposite direction). Moreover, the external magnetic field will be perpendicular to the tape in the straight section and parallel in the curved one. This will create a more complex behavior than in the transport current operating condition.

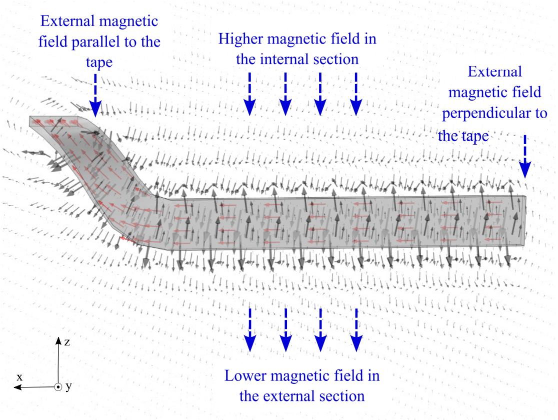

Figure 3.17: Diagram of the applied magnetic field in the saddle coil. The external magnetic field is depicted with dashed blue arrows and the self field of the coil with black continuous arrows. The transport current direction inside the coil is represented with continuous red arrows.

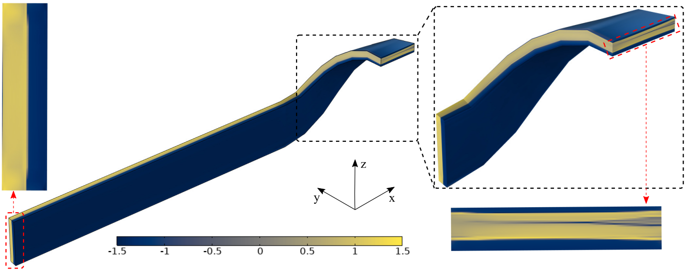

Figure 3.18: Normalized current density in one-fourth of the saddle coil for AC transport current ($f = 50\,\mathrm{Hz}$ and $I_{\mathrm{peak}} = 100\,\mathrm{A}$) and external magnetic field ($f = 50\,\mathrm{Hz}$ and $B_{\mathrm{ext}} = 100\,\mathrm{mT}$) in z-direction and in phase with the coil self-field, when the current is equal to zero and after the first half period of the sinusoidal cycle. A Zoom in the curved section of the coil is presented on the right to show the transition between a full and partially penetrated area.

Figure 3.18 shows the current density behavior when the transport current is equal to zero, and after the first half period of the sinusoidal cycle. As can be observed, the straight section is fully penetrated with critical current density. We can notice one front of current coming from the inner side of the homogenized stack, and a very thin current front in the outer part of the middle of the straight section (where the external and self field are in opposite directions). The curved section shows a transit behavior in space from a fully penetrated zone (straight part) to a partially penetrated one. In the middle, we can notice two fronts of current penetrating the stack at the top and bottom. The inner part is fully penetrated, but the outer part has gray areas that show a partial penetration of the current in the coil. In comparison with the transport current operating condition (figure 3.14), this behavior indicates that the external magnetic field has a stronger influence in the straight section of the coil than in the curved one, due to the torsion of the stack in the geometry of the coil from the straight part (where the external magnetic field is perpendicular to the tape) into the curved part (where the external magnetic field is parallel to the tape).

The total AC losses in the coil for this operating condition are $3.62\,\mathrm{J}$ per cycle, which represents more than three times the AC losses of the transport current case with the same current amplitude ($0.95\,\mathrm{J}$ per cycle).

As it was done in the transport current simulation, a 2D model of the middle of the straight section was built with transport current and an external magnetic field applied in the z-direction. An average turn length is considered to extrapolate the results and estimate the losses of the whole coil with the 2D model. The total AC losses estimated with the 2D model are $4.03\,\mathrm{J}$ per cycle. The 2D model overestimates then the losses by $10.17\,\%$ in this case. This difference can be related to the previously explained behaviour in the curved part of the coil and can be more significant if the ratio between the straight part length and the curved part length is lower.

The complex current density behavior and the big increase in the AC losses observed in this sub-section (compared with the transport losses case) suggest that a 3D approach is better suited for the analysis of this operating condition. This 3D approach provides a more accurate estimation of losses and allows an electromagnetic analysis that can not be done with a 2D approximation.

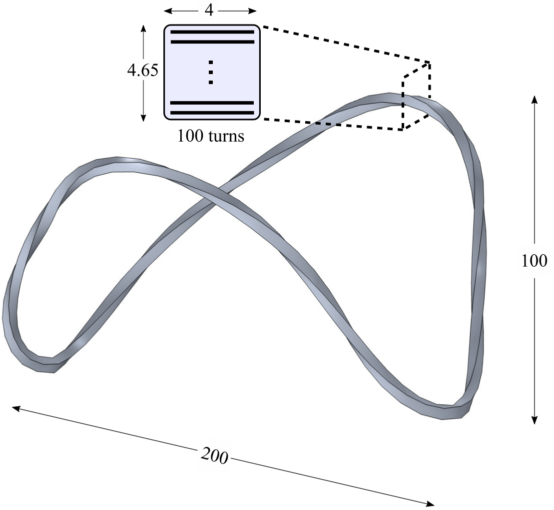

Figure 3.19: Geometry and dimensions of the twisted coil under study. The coil is made with 100 turns of HTS tape, which creates a stack 4 mm wide and 4.65 mm height in the cross-section of the coil. All the dimensions are in millimeters.

3.4.4 Twisted coil

In this case, a more complex geometry without straight parts is studied. The twisted coil has only curved sections with a continuous twist along the length of the coil. The model and development of coils with this kind of geometry can be beneficial for the fusion sector [81], [82]. However, the case under analysis is not part of any specific application. As it was shown in the saddle coil case, the detailed geometry and electromagnetic environment are necessary for any analysis of superconducting devices and applications, since they can strongly influence the losses and electromagnetic behavior of the coils. Therefore, this case of study can be seen as a complete curved and twisted coil analysis that shows the potential application of the modeling approach in a coil similar to the one used in the fusion sector.

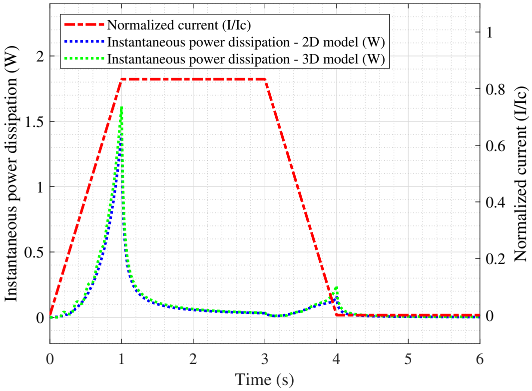

Figure 3.20: Current ramp-up/down process (load cycle) and instantaneous power dissipation behavior in the twisted coil computed with the 3D and 2D T-A homogenization models.

The geometry and dimensions of the coil are presented in figure 3.19. Due to the presence of one symmetry plane, only one-half of the coil was modeled. The critical current of this coil is $60\,\mathrm{A}$.

Due to the complex shape and general dimensions of the coil, the mesh of this geometry must be done carefully to keep the problem within a manageable number of degrees of freedom that provides a good compromise between accuracy and computation time. In the simulations presented in this section, a quadrilateral mesh with 16 elements along the tape width and 5 elements along the stack height is used in the cross-section of the coil. The number of elements along the length of half of the coil is 36 and a free tetrahedral mesh is used in the surrounding air domain. The whole mesh has 25828 elements, which results in 327891 degrees of freedom. The model has a computation time of $57\,\mathrm{h}$ with an Intel Xeon Gold 6242 2.80GHz - 2 processors - computer with 64 logical processors and 384 GB of RAM.

The operating condition considered for this coil is DC transport current. For this reason, the current ramp-up/down process is simulated as one possible test or operating cycle. The ramp-up process of the current is simulated first. The current is increased from $0\,\mathrm{A}$ to $50\,\mathrm{A}$ ($83.33\,\%$ of the critical current) in one

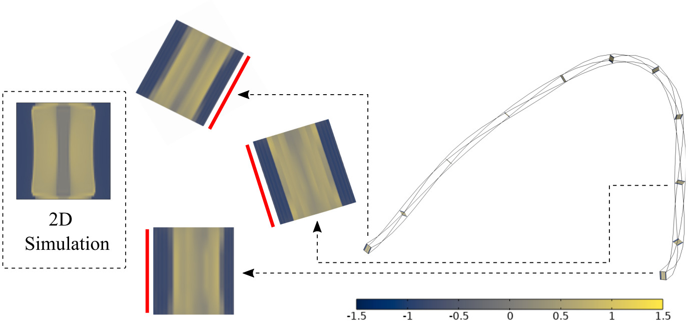

Figure 3.21: Normalized current density in one half of the twisted coil at $t = 5.5\,\mathrm{s}$ (during the relaxation time after the ramp-down process). A zoom in the cross-section of the coil at three different locations is presented on the left together with the behavior of the normalized current density in the 2D model at the same instant in time.

second. Then, the current is kept constant for $2\,\mathrm{s}$ as relaxation time. Afterwards, the ramp-down process is simulated. Therefore, the current is decreased from $50\,\mathrm{A}$ to $0\,\mathrm{A}$ in one second and kept constant for $2\,\mathrm{s}$ as relaxation time. The overall load cycle and instantaneous power dissipation can be observed in figure 3.20. There are two peaks in the losses of the coil related to the ramp-up/down periods of the current. These losses were estimated by using the aforementioned 3D approach and a simplified 2D T-A homogenized model of the cross-section of the coil. The 3D model estimates a peak in the instantaneous power dissipation due to the first ramp of $1.61\,\mathrm{W}$ and the 2D model estimates a peak of $1.40\,\mathrm{W}$. This difference can be related to the fact that the 2D model can not consider the continuous twist and curves along the length of the coil. Similarly, the 3D model also estimates a slightly higher value for the second peak in the instantaneous power dissipation due to the second ramp ($0.24\,\mathrm{W}$), in comparison with the 2D model ($0.16\,\mathrm{W}$). The losses estimated in the whole load cycle are $0.70\,\mathrm{J}$ and $0.61\,\mathrm{J}$, for the 3D and 2D models respectively. The 2D model underestimates the total losses by $13.29\,\%$.

Figure 3.21 shows the behavior of the current density in half of the coil at t=5.5 s (during the relaxation time after the ramp-down). In this figure, the red line highlights the position of the same side of the coil cross-section along the twist.

The current penetration is sometimes higher on one side of the homogenized stack, sometimes higher on the other side, and in some cases it looks symmetrical. This behavior is related to the interaction of the current density with the self-field produced by different parts of the curved and twisted geometry, which can cause local higher penetration and saturation of current. This behavior can not be reproduced by a 2D model. Figure 3.21 also shows the current penetration in the 2D T-A homogenized model at the same time instant. As it can be observed, the current penetration is more symmetrical in the 2D model. This can cause the discrepancies in the estimation of losses presented before. These discrepancies can be higher depending on the geometry, local effects, and operating conditions.

In this case of study, the 2D T-A homogenized model can provide a first estimation of the losses due to the current ramp-up/down process (without external magnetic field). However, a 3D model can provide a better electromagnetic analysis of local effects (current saturation and high penetration zones) that can cause higher losses in different operating conditions or electromagnetic environments.

4 Modelling of HTS stator winding and AC loss estimation

This chapter introduces the methodology used to study the electromagnetic behaviour of HTS stator winding of a superconducting generator. The modelling approach is based on the T-A formulation of the Maxwell equations. This formulation requires the current as a function of time in each superconducting tape as an input. A methodology to calculate this current distribution is presented in this chapter. The procedure introduces a previous step in the building model process and allows a better connection of the machine design with the estimation of losses in the superconductor in order to get a more efficient machine. The approach is applied to a $10\,\mathrm{MW}$ superconducting generator design, where over one thousand tapes cross-sections are modelled in 2D. The superconductor's non-linear behaviour and critical current density anisotropy are considered. Losses are estimated for different designs and several improvements to reduce the losses in the superconducting winding are shown. In this chapter, the modelling approach is presented first with a brief description of the materials and symmetries considered in the models. Then, two main design proposals are analysed, an air gap winding design and a design with iron teeth. Finally, three approaches to reduce AC losses in the superconducting coils are analysed: tape width reduction, use of non-planar coils and temperature reduction.

4.1 Modelling approach

The models presented in this chapter are a 2D representation of the cross-section of an electrical machine. Therefore, the end-effects (winding heads) in the machine are not considered. We estimate the total losses by multiplying the 2D results by the effective length of the electrical machine.

The T-A formulation is used to study the electromagnetic behaviour and estimate the losses in the superconducting tapes. This formulation has already been used in previous studies to model cross-sections of superconducting electrical machines with a few hundred tapes [83], [84], [85], [86]. This methodology requires the current as a function of time in each superconducting tape. For problems involving electrical machines, this input is traditionally computed with an external software/model. Therefore, a direct connection of the estimation of losses with the basic machine design is not easy to achieve. Here, an approach that estimates the required current distribution as a step to build the numerical model is followed. This allows estimating losses, calculating torque and proposing design improvements with the same program (Comsol Multiphysics). Since the cross-sections of the electrical machines under study involve thousands of superconducting tapes, symmetries are considered to reduce the size of the problem.

4.1.1 Symmetries

The cross-sections of the $10\,\mathrm{MW}$ superconducting generators under analysis have several thousands of tapes, permanent magnets and magnetic materials with non-linear $B-H$ relation. Moreover, the resistivity of the HTS tapes is modelled by using a non-linear $E-J$ power-law relation, where the critical current density depends on temperature and magnetic field amplitude and direction. The number of degrees of freedom (DOF) arising from modelling the whole cross-section of these electrical machines is very large. Therefore, the simulated models are reduced to one pole pair as illustrated in Figure 4.1, where the whole cross-section of a 20 pole pairs electrical machine is shown. A zoom in one pole pair is depicted

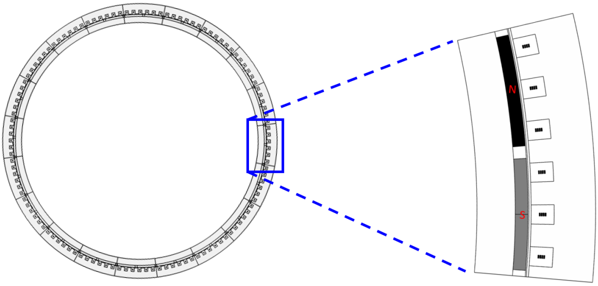

Figure 4.1: Zoom-in one pole pair of an electrical machine.

in blue (north and south poles are in black and gray colors). Continuity periodic conditions are taken in the upper and lower boundaries of this pole pair. Hence the whole cross-section can be re-built in the post-processing through rotation of the computed solution.

4.1.2 Materials

The magnetic material used in the design of the electrical machine is M330-50A. Measurements of the magnetic and electrical properties are presented in [87] and the relative permeability uploaded in the model is shown in figure 4.2. We assume that the magnetic material will be at room temperature, by taking into account that only the superconductor is operating under cryogenic temperatures in the proposed designs.

The stator coils are wound with a $4\,\mathrm{mm}$ HTS REBCO tape manufactured by SuperPower Inc, more detailed information about it can be found in [88]. This tape is modelled by considering only the superconducting layer surrounded by a homogeneous medium with a resistivity of $1\,\Omega\,\mathrm{m}$ and vacuum permeability ($\mu_0 = 4\pi 10^{-7}\mathrm{H\,m^{-1}}$), by taking into account that the resistivity of the superconducting material is several orders of magnitude lower than the resistivity of other materials forming the tape.

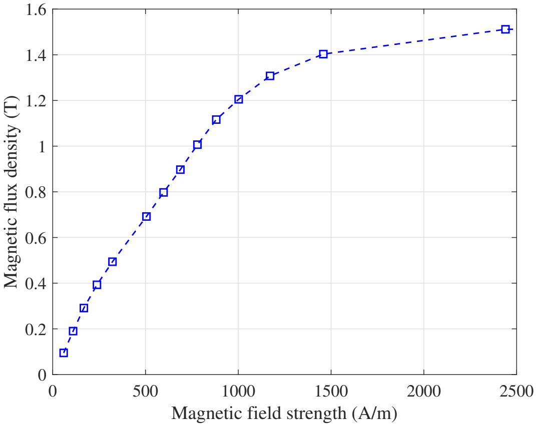

Figure 4.2: B-H curve of M330-50A at room temperature.

A critical current density of $3\,\mathrm{MA\,cm^{-2}}$ at $77\,\mathrm{K}$ and an average temperature of $65\,\mathrm{K}$ is considered in the presented simulations. Since the tape's critical current density depends on temperature (T) and magnetic field ($\vec{B}$), we use a lift factor that models the anisotropic dependence on the local magnetic field [89]:

$$L = \frac{J_\mathrm{c}(\vec{B},T)}{J_\mathrm{c}(77\,\mathrm{K})} = \frac{L_0(T)}{\left(1 + \frac{\sqrt{k(T)^2 B_\parallel^2 + B_\perp^2}}{B_{c0}(T)}\right)^{b(T)}}. \tag{4.1}$$

In this equation, $J_\mathrm{c}(\vec{B},T)$ is the critical current density for a given temperature and magnetic field, L is the lift factor and the parameters: $L_0(T)$, $k(T)$, $B_{c0}(T)$ and $b(T)$ express the temperature dependence according to table 4.1 [89]. $B_\parallel$ and $B_\perp$ are the parallel and perpendicular (to the wide face of the tape) components of the magnetic flux density. We compute these parallel and perpendicular components by employing the dot product between the magnetic flux density and unitary vectors defining normal and tangential directions to each tape.

Table 4.1: Lift factor parameters for different temperatures [89].

$T(\mathrm{K})$	L_0	k	B_{c0}	b
30	6.12	0.07	3.23	1.41
40	5.29	0.10	1.86	1.12
50	4.12	0.17	1.26	0.96
65	2.44	0.61	0.59	0.77

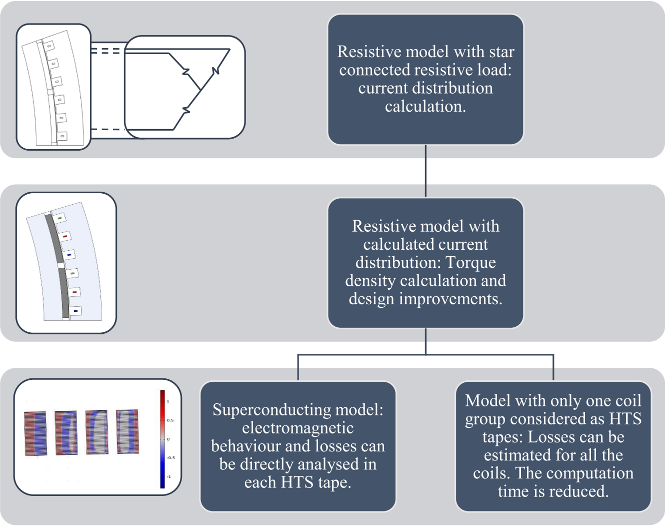

Figure 4.3: Diagram of the building model process.

4.1.3 Models

Since the current in each HTS tape is needed as an input for the T-A formulation, in this section an approach is proposed where the stator coils current distribution is computed in a basic model by connecting a load to the generator. Once we have the current distribution, the load is disconnected (resistive model) and superconducting coils details are added (superconducting model). As a consequence, we built one model to make design improvements and one to estimate losses in a single process. A schematic description of the building model procedure is presented in figure 4.3. An additional superconducting model is considered in this section, which allows reducing the computation time by modelling only one coil group cross-section as HTS material.

- *Resistive model:* the geometry of the cross-section of the coils is typically homogenized when modelling conventional machines. Each coil cross-section is represented by a homogeneous block with approximately the same electromagnetic behaviour as a fully detailed cross-section [90], [91], [92]. Therefore, a simplified resistive model (without the superconducting material) is developed first based on this approach. Initially, a resistive load is connected to the model and the current flows as a result of induced voltage in the coils. These induced currents are the necessary input for the T-A formulation. In the following step, the induced current distribution is fed into the same model, the load is disconnected and the amplitude of the current is adjusted to the nominal power of the machine if necessary.

  The induced currents, arising from the connected resistive load, can include several harmonics that can be analysed by using Fourier Transform. However, we assume that the amplitude of the harmonics is too low to generate an important impact on the estimation of losses as they could be significantly reduced in this or previous stages of the design. Moreover, the main objective of our study is not related to harmonic content analysis or mitigation, but to electromagnetic modelling and loss estimation. Therefore, we only consider the fundamental signal.

  In this model, the torque density and the general electromagnetic behaviour can be analysed. Since the computation time is within the range of minutes, several improvements and re-runs can be quickly done.

- *Superconducting model:* once the current distribution is available, it can be imported into a model that considers the HTS material. The homogenized coils cross-sections are replaced by detailed stacks of tapes, the T-A formulation is used and the current distribution is imposed through boundary conditions as described in chapter 3.

The electromagnetic behaviour and loss estimation can be directly analysed in each HTS tape of the machine by using this model. However, the computation time is still too high (in the range of days) with conventional commercially available computers.

- *Model with only one coil group considered as HTS tapes:* as it will be shown in the following sections, the electromagnetic behaviour in each group of phase coils cross-section is very similar (shifted in time and/or space). As a consequence, we can model only one group of coils with details. This model allows estimating losses in all the superconducting tapes within a reasonable time (in the range of hours) with conventional commercially available computers.

4.2 Design with iron teeth

This machine design is based on distributed coils located in a stator with iron teeth. Each coil has a racetrack form, and four racetrack coils are stacked on top of each other inside a slot to conform one phase in one pole pair. Each of these coils are connected in series. The whole machine has an effective length of $2.4\,\mathrm{m}$ and an external radius of $2.7\,\mathrm{m}$. A brief summary of the characteristics of this machine is presented in table 4.2. The geometry of one pole pair cross-section is shown on the left side of figure 4.4.

The electric frequency of the generator depends on the rotation speed of the rotor and the number of pole pairs of the generator. In wind turbine applications, the speed is usually between $8\,\mathrm{min}^{-1}$ and $18\,\mathrm{min}^{-1}$ and it depends on the design of the system [93]. A nominal speed of $10\,\mathrm{min}^{-1}$ and 20 pole pairs are considered in this case. Therefore, the nominal frequency of the generator is $3.33\,\mathrm{Hz}$.

Table 4.2: Main parameters of the superconducting generator, design with iron teeth.

Number of slots	120
Number of pole pairs	20
Number of slots per pole pair	6
Remanent induction of permanent magnets	1.28 T
Number of coils per phase per pole pair	4
Number of turns per coil	50
Peak current in each coil	141.4 A
Nominal electrical frequency	3.33 Hz
Target nominal power	10 MW

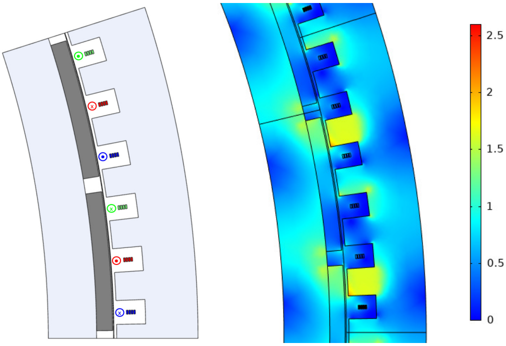

Figure 4.4: One pole pair cross-section of the machine design with iron teeth. The geometry is presented on the left. Phase A is depicted in blue, B in red and C in green. The direction of the current is indicated in a circle close to the coils. The magnetic flux density norm in T is shown on the right, when phase A current is maximum (time = 0.375 s).

The resistive model approach is followed to get the appropriated current distribution in the coils of the machine, which is then imported into the T-A formulation in order to compute losses in the HTS tapes. The fully superconducting model is built first. The right side of figure 4.4 presents the magnetic flux density norm in one pole pair when phase A current is maximum. The main advantage of the fully superconducting model is that losses can be estimated and electromagnetic behaviour can be analysed in each superconducting tape cross-section of the generator. However, a similar electromagnetic behaviour (shifted in space and time)

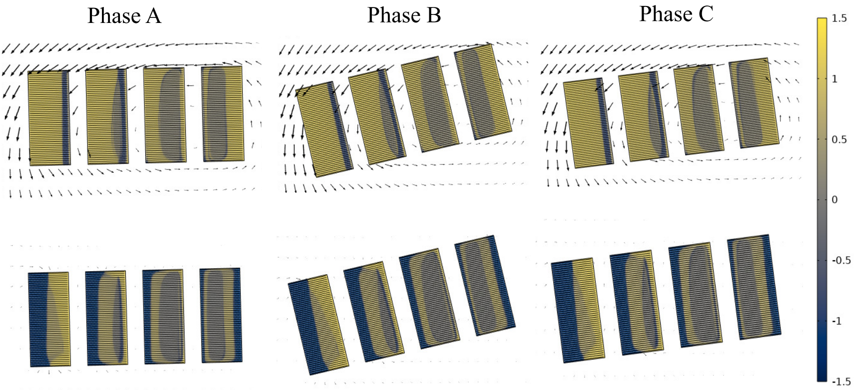

Figure 4.5: Behaviour of the normalized current density $(J/J_c(\mathbf{B}))$ and magnetic field (black arrows) in the cross-section of each phase coil when the current of each phase is maximum (top) and zero (bottom) for the superconducting model of the electrical machine design with iron teeth.

can be expected for the different coils cross-section of all the phases, by taking into consideration the aforementioned characteristics and geometry. In order to verify this hypothesis, the normalized current density and magnetic field distributions were compared in the different coils cross-section for different instants in time. As it can be seen in figure 4.5, the current penetration and magnetic field behaviour are similar in the different phase coils cross sections (rotated in space for the different phases) when the current in each one of them reaches its maximum and zero values (shifted in time for each phase).

The instantaneous power dissipation can be estimated in all the stator coils by using this model. In figure 4.6 losses in the first coil (from left to right in figure 4.4) for the different phases are plotted. They have the same periodic shape in the different phases, which can be expected given the behaviour mentioned above. From these results, it can be concluded that the electromagnetic behaviour and losses can be analysed with the same accuracy when the calculations of one phase coil group are extrapolated into the other phases. Therefore, the computation time can be reduced (with the same general electromagnetic behaviour) if only

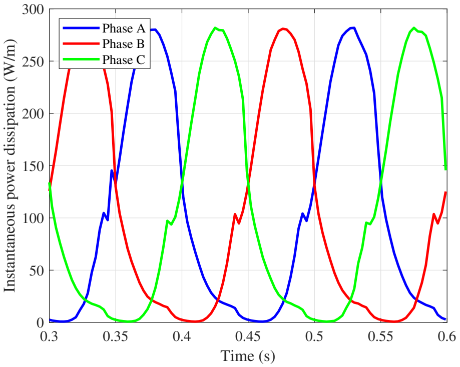

Figure 4.6: Instantaneous power dissipation in the first racetrack coil, from left to right in figure 4.4, for each phase of the design with iron teeth.

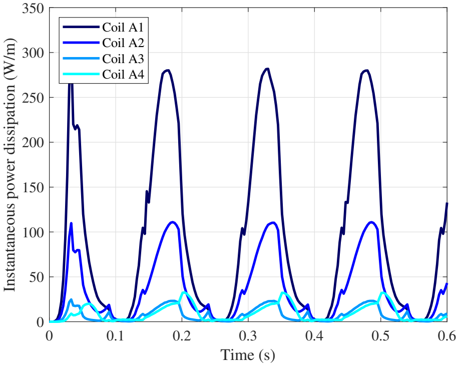

Figure 4.7: Instantaneous power dissipation in the coils of phase A for the design with iron teeth, in figure 4.4 the first coils from bottom to top numbered from left to right as A1, A2, A3 and A4.

one group of coils is modeled as superconducting material, and all the other coils are homogenized.

Figure 4.7 shows the instantaneous power dissipation in the four coils cross-section of phase A, where the coils have been numbered from left (closer to rotor) to right (closer to stator). The first coil experiences higher losses compared to coils 3 and

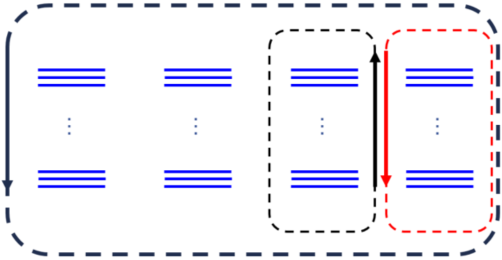

Figure 4.8: Basic schematic behaviour of the self field in the coils cross-section for the design with iron teeth.

4. The tapes in this coil also experience a higher current penetration and a higher perpendicular (to the wide face of the tape) magnetic field.

In order to better understand the behaviour of the losses and magnetic field in one coil group, a short review of the field produced by the current flowing through the coils is presented in figure 4.8. If only the interaction between two coils is considered, the perpendicular magnetic field between the coils is reduced since both carry the same current. However, when we consider 3 or more coils, the perpendicular magnetic field increases in the first and last coils of the array. The magnetic field norm may further increase in the first coil, since this is closer to the rotor. However, coils 3 and 4 are closer to stator iron, which could provide a low reluctance path for the magnetic field to turn not so close to the stack, and they are also partially shielded by coils 1 and 2.

The overall behaviour of the losses can be better appreciated in figure 4.9, where the average power density dissipation (calculated as the dot product between current density and electric field) is shown in the cross-section of phase A coil group. It can be noticed from this picture that coil 1 will have a higher dissipation, hence it may be under higher thermal stress.

The losses in phase A coil group can be calculated by integrating the dissipation, and the losses in all the coils of the machine in W can be estimated by multiplying this value by the number of coil groups (6), number of pole-pairs (20), active

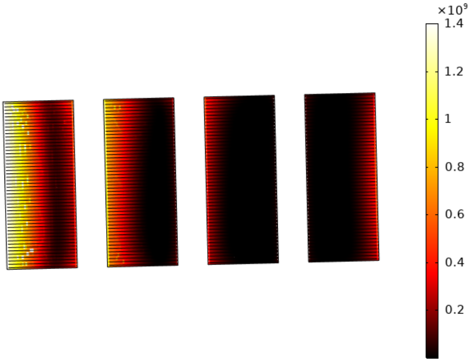

Figure 4.9: Average in time power density dissipation ($\mathrm{W\,m^{-3}}$) of the phase A coil group for the machine design with iron teeth.

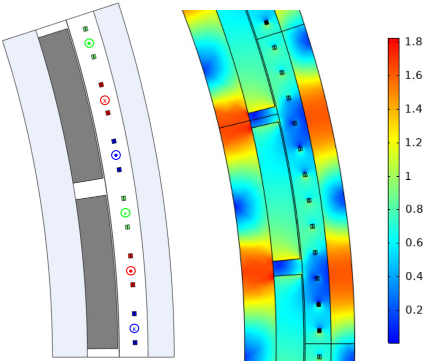

Figure 4.10: One pole pair cross-section of the machine design without iron teeth. The geometry is presented on the left. Phase A is depicted in blue, B in red and C in green. The direction of the current is indicated in a circle close to the coils. The magnetic flux density norm in T is shown on the right, when phase A current is maximum (time = $0.375\,\mathrm{s}$).

length of the machine ($2.4\,\mathrm{m}$) and nominal frequency ($3.33\,\mathrm{Hz}$). This results into a total loss in the stator superconductive coils of $46.85\,\mathrm{kW}$.

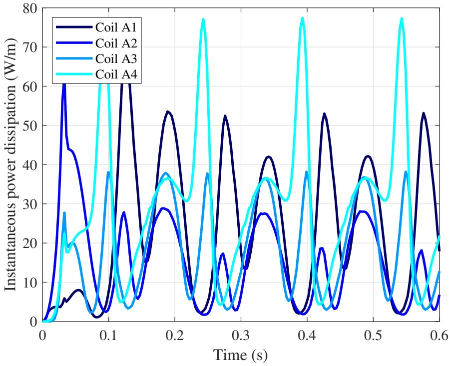

Figure 4.11: Instantaneous power dissipation in the coils of phase A for the design without iron teeth, in figure 4.4 the first coils from bottom to top numbered from left to right as A1, A2, A3 and A4.

4.3 Air gap winding design

The air gap winding design is very similar to the previous one. It uses the same coils, number of turns, number of pole pairs and magnets. However, the stator has no teeth, the racetrack coils are distributed in the stator in groups of two, it has an effective length of $3.7\,\mathrm{m}$ and external radius of $2.62\,\mathrm{m}$. The geometry of one pole pair cross-section of this design is presented on the left side of figure 4.10.

The model of this design is built by following the same approach. The fully superconducting model gives the same behaviour per coil group in this design too, shifted in space and/or time. For this reason, the analysis is focused only on one phase coil group. The coil group under study is integrated by the first four coils cross-section (from bottom to top) depicted in blue on the left side of figure 4.10.

The magnetic flux density norm in the cross-section of one pole pair can be seen on the right side of figure 4.10, and instantaneous power dissipation in the four coils cross-section are shown in figure 4.11, where the coils have been numbered from left (closer to rotor) to right (closer to stator), and from bottom to top.

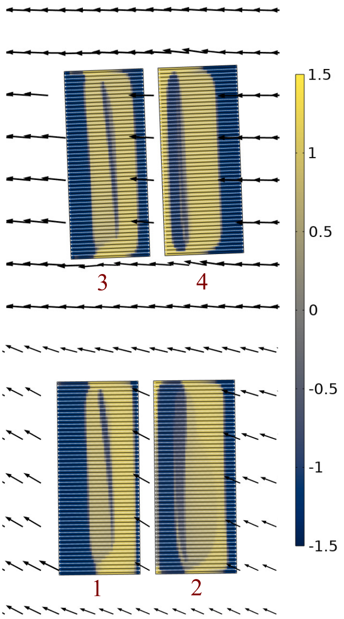

Figure 4.12: Behaviour of the normalized current density $(J/J_c(\mathbf{B}))$ and magnetic field (black arrows) in the cross-section of the coils of phase A for the machine design without iron teeth, when the current in the coil group is zero.

In this design, the current penetration is more similar in all the four coils cross-section, as shown in figure 4.12. Moreover, the average power density dissipation, shown in figure 4.13, is better distributed compared to the previous design. Only coil number four seems to experience slightly higher losses compared to the others. This behaviour supports the aforementioned analysis regarding the interaction between only two coils.

As it was done in the previous design, the losses in phase A coil group can be calculated by integrating the dissipation and the losses in all the coils of the machine in W can be estimated by multiplying this value by the number of coil groups (6), the number of pole-pairs (20), the active length of the machine ($3.7\,\mathrm{m}$) and the nominal frequency ($3.33\,\mathrm{Hz}$). This results into a total loss in the stator superconductive coils of $39.81\,\mathrm{kW}$.

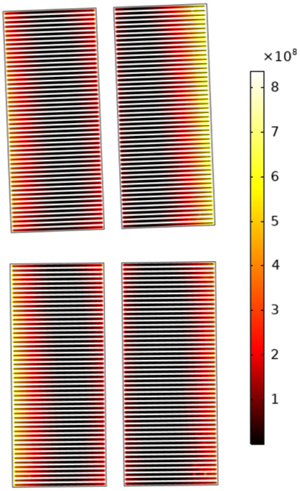

Figure 4.13: Average power density dissipation ($\mathrm{W\,m^{-3}}$) of the phase A coil group for the machine design without iron teeth.

4.4 AC loss reduction

The reduction of the AC losses in the stator superconducting winding is beneficial for the development of superconducting electrical machines. However, this AC loss reduction is not easy to achieve. The coils are exposed to time changing transport current and magnetic field. The horizontal array of coils presented in the first design yields a higher dissipation that is concentrated in the coils closer to the rotor. The second design achieves a $15\,\%$ reduction in losses. However, the active length of the machine increases by $54\,\%$. This section explores how to obtain a stator coil design optimized for low AC losses by considering a design with iron teeth. Three main approaches to reduce AC losses in the stator superconducting winding are presented: use of non-planar coils, tape width and temperature reduction. A detailed analysis of the current penetration and the behaviour of the magnetic field around the coils is introduced in this section. Particular attention is given to the position of the coils inside a slot and several coil configurations are presented. It is shown that certain coil arrangements lead

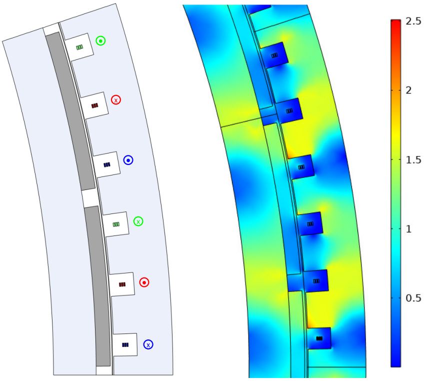

Figure 4.14: One pole pair cross-section of the machine design used to analyse the AC loss reduction in the stator superconductive winding. The geometry is presented on the left. Phase A is depicted in blue, B in red and C in green. The direction of the current is indicated in a circle close to the coils. The magnetic flux density norm in T is shown on the right, when phase A current is maximum (time = $0.375\,\mathrm{s}$).

to a significantly lower total loss, and a more uniform loss distribution, which ultimately leads to the possibility of increasing the operating temperature.

The basic design of the machine used in this section is very similar to the one described in section 4.2. It uses the same magnetic material (M330-50A), superconducting tape, number of slots, pole pairs, and magnets. The main difference is that the number of coils per phase per pole pair was reduced from 4 to 3, to minimize the horizontal effect shown in the design with iron teeth. This machine has an external radius of $3.29\,\mathrm{m}$ and an active length of $2.4\,\mathrm{m}$ to achieve a rated torque of $10\,\mathrm{MN\,m}$. The geometry of one pole pair cross-section of this design is presented on the left side of figure 4.14, and the magnetic flux density norm in the cross-section of one pole pair can be seen on the right side by assuming coils with a racetrack shape.

4.4.1 Non-planar coils

In this subsection, different shapes of the stator coils are studied to verify whether changes in the orientation of the cross-section of the coils can reduce the AC losses in the stator winding.

- *Typical arrangement:* The first configuration under analysis uses coils with a racetrack form. This shape is considered typical in superconducting electrical machines. Three coil layers are stacked one on top of the other in rectangular slots for one phase in one pole pair. These coils are wound with a $4\,\mathrm{mm}$ tape for an initial calculation. Figure 4.15-A shows the behaviour of the normalized current density (left), average power density dissipation (center) and AC loss per tape (right). There is a high current penetration in the first coil from left to right (closer to the rotor). This coil experiences a higher perpendicular component (to the wide face of the tape) of the magnetic field in comparison with the other two. It can also be noticed that most of the dissipation is located in the same coil. Losses are higher on the left side, where the magnetic field is higher. The total losses in the superconducting stator winding are $28\,\mathrm{kW}$.
- *90-degree inclined coils:* In this arrangement, we have rotated the cross-section of the coils 90 degrees in comparison with the previous solution. Therefore, the tapes closer to the rotor are better aligned with the magnetic field. Figure 4.15-B shows the behaviour of the normalized current density (left), average power density dissipation (center) and AC loss per tape (right). The first coil from top to bottom has now a high current penetration and it is exposed to a high perpendicular component of the magnetic field. Therefore, the highest average dissipation is located now in this coil. The total losses for this alternative are $22.85\,\mathrm{kW}$, which represents a $18\,\%$ reduction in comparison with the typical arrangement.
- *Top and bottom inclined coils:* In the previous configuration there is still an uneven distribution of the losses that can be related to the orientation of the coils cross-section with respect to the magnetic field. Therefore,

A - Typical arrangement

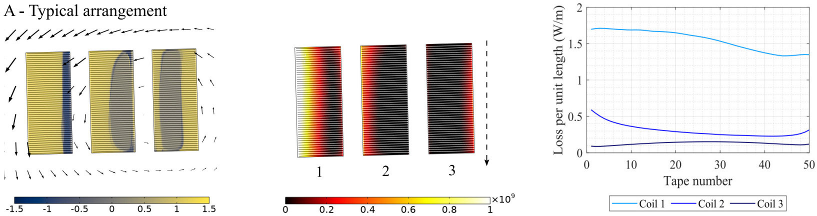

B - 90-degree inclined coils

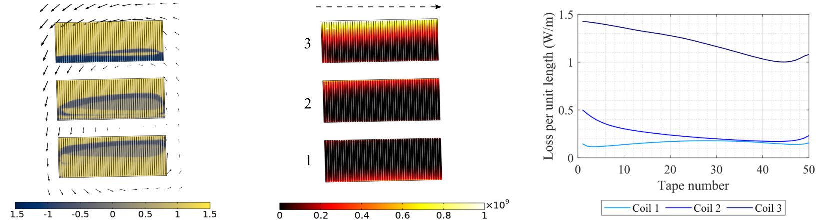

C - Top and bottom inclined coils

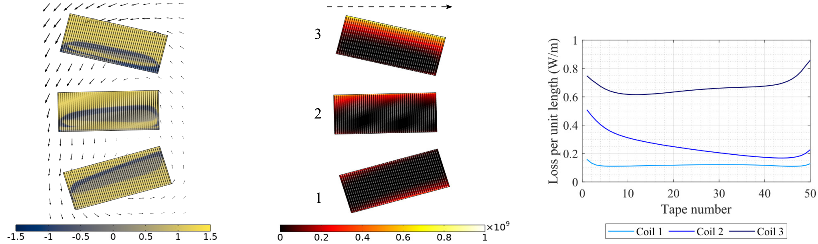

D - Star Configuration

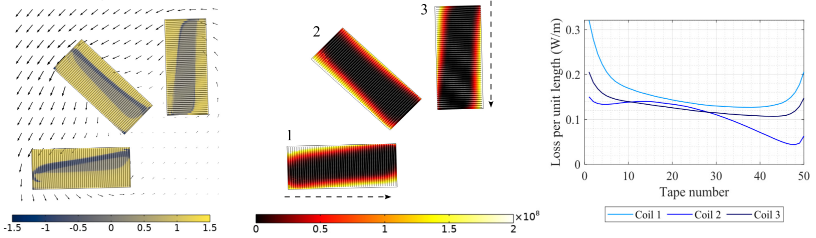

Figure 4.15: Current density and AC loss behaviour in the machine design used to analyse the AC loss reduction in the stator coils with non-planar coils. From left to right: Behavior of the normalized current density ($J/J_c(\vec{B})$) and magnetic field (black arrows) in the coils of phase A when the current in the coil group is maximum, average power density dissipation ($\mathrm{W\,m^{-3}}$) in the coils of phase A, and AC loss per tape (numbered in the direction of the arrow) per coil.

the top and bottom coils are further inclined in this arrangement. This approach allows reducing the perpendicular component of the magnetic field around the coils, which further reduces the losses. In figure 4.15-C we can appreciate the behaviour of the normalized current density (left), average power density dissipation (center) and AC loss per tape (right) for this configuration. As it can be seen, the current penetration and average power density dissipation have decreased in comparison with the previous arrangement. Moreover, the losses per unit length in the tapes of coil number 3 are also lower. The total losses in the superconducting coils for this configuration are $14.73\,\mathrm{kW}$. This means a $47.4\,\%$ reduction of losses in comparison with the typical arrangement.

- *Star Configuration:* It was shown in the previous configuration analysis that the orientation of the tape can play a key role in the average power density dissipation. For this reason, we propose a new arrangement of the cross-section of the coils by trying to better align the tapes with the magnetic field. This approach allows reducing further the perpendicular component of the magnetic field. Figure 4.15-D shows the behaviour of the normalized current density (left), average power density dissipation (center) and AC loss per tape (right) of this new star configuration. We can observe in this figure that the current penetration is now similar between coils, and the dissipation is better distributed. Furthermore, the total losses in the superconducting winding are $5.57\,\mathrm{kW}$, which represents a $80\,\%$ reduction in comparison with the typical arrangement.

4.4.2 Tape width reduction

The AC losses can also be reduced by decreasing the width of the tape. This approach can bring a reduction in the magnetization losses of single tapes under a uniform perpendicular magnetic field [39]. For this reason, in this subsection the AC losses in the four previous configurations are estimated again by considering a $2\,\mathrm{mm}$ tape instead of $4\,\mathrm{mm}$. In these calculations, the same parameters of the

A - Typical arrangement

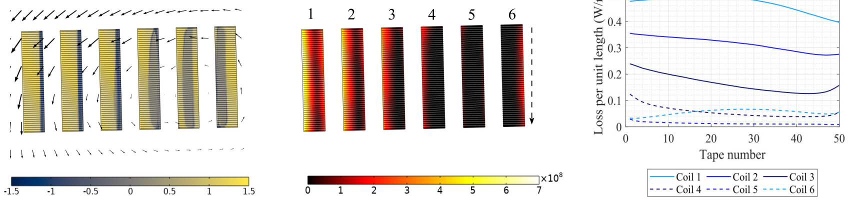

B - 90-degree inclined coils

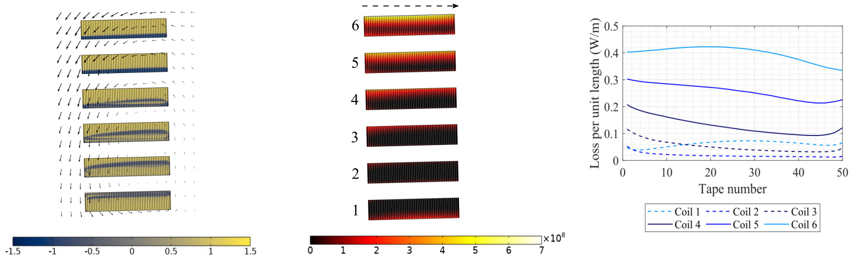

C - Top and bottom inclined coils

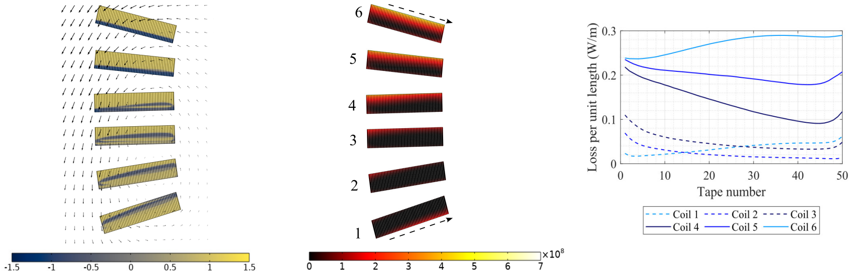

Figure 4.16: Current density and AC loss behaviour in the machine design used to analyse the AC loss reduction in the stator coils with non-planar coils and tape width reduction. From left to right: Behavior of the normalized current density ($J/J_c(\vec{B})$) and magnetic field (black arrows) in the coils of phase A when the current in the coil group is maximum, average power density dissipation ($\mathrm{W\,m^{-3}}$) in the coils of phase A, and AC loss per tape (numbered in the direction of the arrow) per coil.

$4\,\mathrm{mm}$ HTS tape have been used (only the transport and critical current are reduced to half). The number of coils per phase per pole pair are doubled to keep the same amount of current per slot and the same basic design.

- *Typical arrangement with 2 mm tape:* Figure 4.16-A presents the behaviour of the normalized current density (left), average power density dissipation (center) and AC loss per tape (right) of the typical arrangement with a 2 mm tape. There are now six layers stacked one on top of the other for each phase in one pole pair. This figure shows a similar behaviour between 2 mm and 4 mm alternatives. There is a higher current penetration and dissipation in the first coils from left to right (closer to the rotor). This uneven distribution of losses can be related to the high perpendicular component of the magnetic field in these coils. However, the total losses in the superconducting coils are 15.42 kW, which represents a 45 % reduction in comparison with the 4 mm tape typical arrangement.

- *90-degree inclined coils with 2 mm tape:* The behaviour of the normalized current density (left), average power density dissipation (center) and AC loss per tape (right) of the 90-degree inclined coils with a 2 mm tape are shown in figure 4.16-B. In this case, the last coils from bottom to top are still experiencing a higher current penetration in comparison with coils number 3, 2 and 1. At the same time, coils 5 and 6 have a higher dissipation and losses per unit length, which shows a strong relation between the perpendicular component of the magnetic field and the dissipation. The total losses in the superconducting coils for this 2 mm tape alternative are 13.21 kW. This means a 42 % reduction in the losses in comparison with the 90-degree inclined coils arrangement with 4 mm tape coil, and 14 % reduction in comparison with the typical arrangement with 2 mm tape.

- *Top and bottom inclined coils with 2 mm tape:* The behaviour of the normalized current density (left), average power density dissipation (center) and AC loss per tape (right) of the top and bottom inclined coils arrangement with a 2 mm tape is presented in figure 4.16-C. It can be noticed from a direct comparison between figure 4.16-C and figure 4.16-B that the average power density dissipation and overall losses per tape in coils 5 and 6 have decreased as a result of the alignment of the tapes with the magnetic field. The total losses in the superconducting coils are 10.3 kW. This represents a 30 % reduction in the losses in comparison with the top and bottom inclined

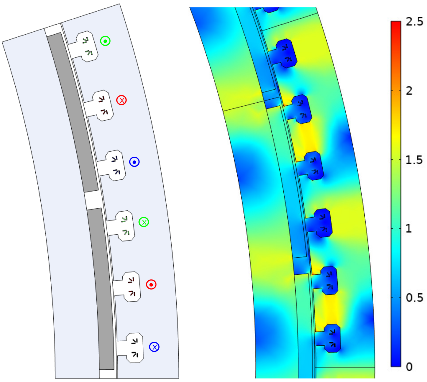

Figure 4.17: One pole pair cross-section of the machine design used to analyse the AC loss reduction in the stator superconductive winding with the star configuration and 2 mm tape. The geometry is presented on the left. Phase A is depicted in blue, B in red and C in green. The direction of the current is indicated in a circle close to the coils. The magnetic flux density norm in T is shown on the right, when phase A current is maximum (time = 0.36 s).

coils arrangement with 4 mm tape, and a 33.2 % reduction in comparison with the typical arrangement with 2 mm tape.

- *Star Configuration with 2 mm tape:* The rectangular shape of the slot is modified in this final arrangement to distribute the coils with a star configuration inside the slots and reduce losses. Figure 4.17 presents the geometry of the cross-section of one pole pair on the left side, and the behaviour of the magnetic flux density norm on the right side. An angular separation was kept between each star arrangement inside the slot. This introduces a high reluctance that can decouple the magnetic field between sub-group of coils. Moreover, the shape of the slot was modified by trimming the corners to provide a better path for the magnetic field to turn in the magnetic material.

The behaviour of the normalized current density (left), average power density dissipation (center) and AC loss per tape (right) of the star configuration with a 2 mm tape are shown in figure 4.18. These results are similar to the 4 mm tape alternative. The star configuration achieves lower losses per unit length and a better distribution of the dissipation in the cross-section of the

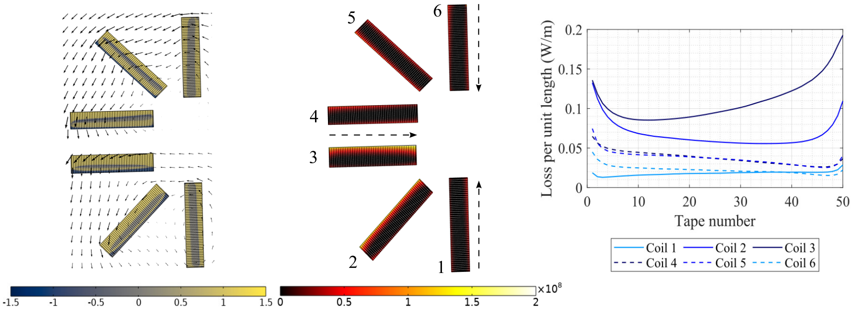

Figure 4.18: Current density and AC loss behaviour in the machine design used to analyse the AC loss reduction in the stator coils with the star configuration and 2 mm tape. From left to right: Behavior of the normalized current density ($J/Jc(\vec{B})$) and magnetic field (black arrows) in the coils of phase A when the current in the coil group is maximum, average power density dissipation ($\mathrm{W\,m^{-3}}$) in the coils of phase A, and AC loss per tape (numbered from outside to inside) per coil (numbered from bottom to top).

coils. The total losses in the superconducting winding for this configuration are 4.15 kW, which represents a 26 % reduction in comparison with the star configuration with 4 mm tape, and a 73 % reduction in comparison with the typical arrangement with 2 mm tape. If the AC losses in the superconducting stator winding of this design are compared with the original typical arrangement with 4 mm tape, the total reduction is equal to 85 %.

4.4.3 Temperature reduction

The AC losses in the stator superconducting winding can also be reduced by increasing the critical current of the tape, for instance, by decreasing the average operating temperature. A parametric study over a wider range of temperatures in the typical arrangement with 2 mm tape was conducted. The critical current of the tape at self-field has been calculated for each temperature. As it can be seen in figure 4.19, the AC losses in the stator winding of the typical arrengement with 2 mm tape can decrease down to 6.16 kW at 5 K. This corresponds with an increase of the critical current of the tape up to 420.8 A. However, it means operating at much lower temperatures where the efficiency of the cooling system

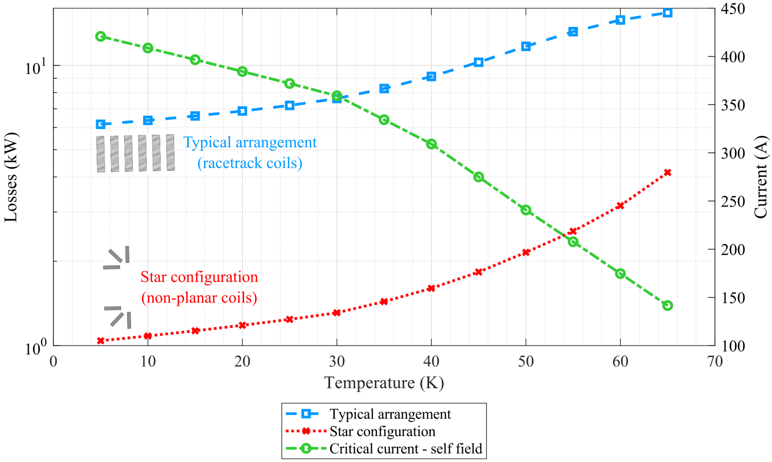

Figure 4.19: Comparison of the AC loss reduction in the typical arrangement with a 2 mm tape by decreasing the average temperature with the losses of the Star configuration with a 2 mm tape. AC losses in the typical arrangement are depicted in blue, AC losses in the Star configuration are depicted in red and the critical current of the tape at self field in green.

will decrease. It can be concluded from these calculations that the level of losses of the star configuration at 65 K can not be achieved with the typical arrangement even if the critical current of the tape is doubled, or the operating temperature of the coils is decreased down to 5 K. Furthermore, there are potential hot spots in the coil's cross-section in the typical arrangement that could be avoided in the design stage with the star configuration.

Since the reduction in the operating temperature can have a strong influence on the efficiency of the cooling system, the study presented in figure 4.19 is complemented by considering the Carnot efficiency (η_c) [94] and an ambient temperature of 298 K:

$$\eta_c = \frac{T_{\text{op}}}{T_{\text{amb}} - T_{\text{op}}}. \tag{4.2}$$

The inverse of equation (4.2) is called Carnot specific power, and it represents the power required at ambient temperature to provide 1 W of refrigeration at the given

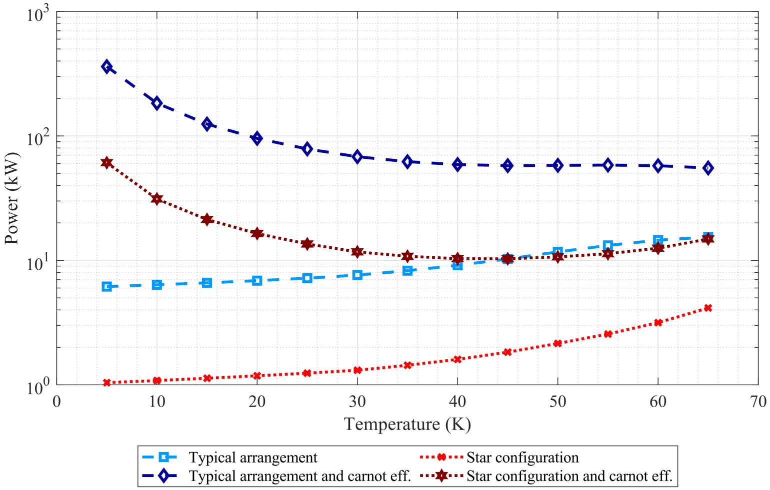

Figure 4.20: Estimation of the cooling power requirements for the typical arrangement and the star configuration with a 2 mm tape, based on the Carnot efficiency [reference]. The AC losses are depicted in light blue (square symbol) and the cooling power requirements are in dark blue (diamond symbol) for the typical arrangement. For the star configuration, light red (x symbol) represents the AC losses and dark red (star symbol) represents the cooling power requirements.

lower operating temperature [95]. Based on this equation, a first estimation of the required cooling power is done. Figure 4.20 shows the comparison of the temperature behavior of the AC loss in the typical arrangement and star configuration with a 2 mm tape, and it also shows how the cooling power requirement increases if we consider the Carnot efficiency. At 5 K the cooling power requirement increases up to 361.2 kW for the typical arrangement. Therefore, the temperature reduction results in a decrease in the AC losses but a significant increase in the cooling power requirement. In the case of the star configuration, the cooling power requirements are significantly lower in comparison with the typical arrangement for all the studied ranges of temperatures. Moreover, the behaviour indicates that a possible optimum operating temperature can be selected. If the minimum cooling power requirements presented in Figure 4.20 are compared, the minimum power required by the typical arrangement (55.28 kW at 65 K) is more than five times higher than the minimum power required by the star configuration (10.29 kW at

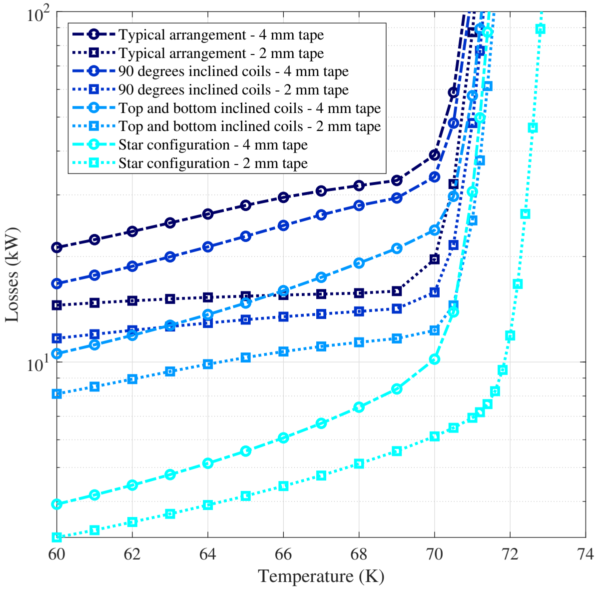

Figure 4.21: Behavior of the losses in the HTS coils in the machine design used to analyse the AC loss reduction for different temperatures and rated frequency of 3.33 Hz.

45 K). These estimations of the cooling power requirements may further increase around 10 to 50 times more depending on the cryocooler efficiency and cooling system design [96].

Figure 4.21 shows the results of a parametric study to investigate the behaviour of total losses in all the presented configurations for different average temperatures. It can be noticed in this plot that a decrease in the tape's width can allow increasing the operating temperature, by keeping the same level of losses. A further increase in temperature is feasible in the star configuration. This advantage can be related not only to the decrease in the losses but also to the better distribution of the dissipation. Therefore, this arrangement offers a more secure and efficient operation of the superconducting coils.

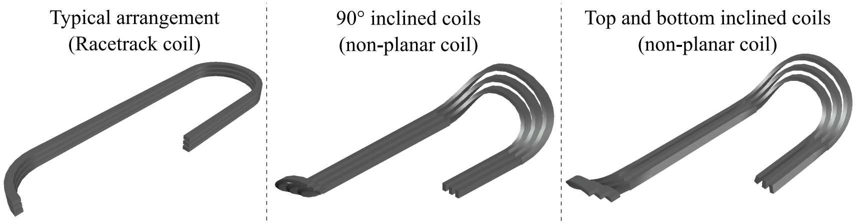

Typical arrangement (Racetrack coil)

90° inclined coils (non-planar coil)

Top and bottom inclined coils (non-planar coil)

Figure 4.22: Feasibility review of the coils. From left to right: three-dimensional rendering of a coil with a typical racetrack shape, three-dimensional sketch proposal of the 90° inclined and top and bottom inclined configurations.

4.4.4 Feasibility review

The design and construction of non-planar and inclined coils is an area under strong development. There are several configurations under research. However, these coils are not easy to build and have been implemented mostly in the magnet technology sector [97], [98], [99], [78]. The introduction of this approach in the stator of a superconducting electrical machine by considering the anisotropy of the critical current is new.

The detailed design and construction of all the presented configurations are not within the scope of this research, since it is necessary to closely study the bending and torsional limits of the tape to wind the coil [100]. These studies can be done based on a specific application or shape [101].

3D renderings and sketches have been made to help the reader understand how the configurations could look like. These drawings are just representations of possible winding and will require detailed calculations and analysis before construction. For simplicity, only the 4 mm tape solutions are represented. However, the same approach can be followed for the 2 mm tape alternatives. The first arrangement that was introduced is based on coils with a classic racetrack shape, like the one shown on the left side of figure 4.22. The winding heads can be bent in this typical configuration to arrange all the coils in the stator of an electrical machine [102], [103].

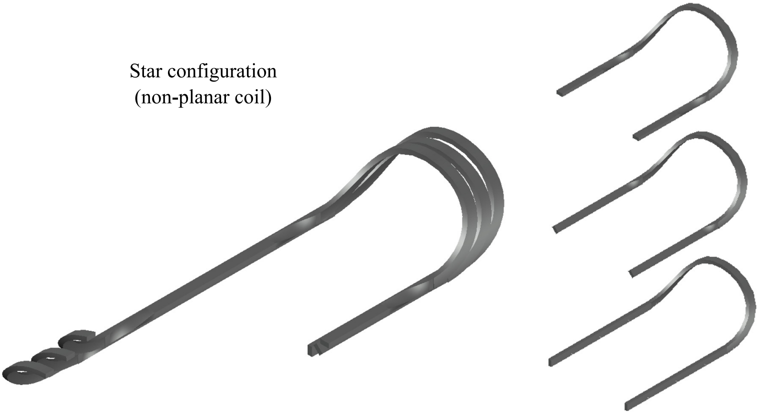

Figure 4.23: Three-dimensional sketch proposal of the star configuration.

The next configuration is based on a 90-degree rotation of the typical racetrack coil cross-section. This can be achieved by following a similar approach to the one presented in [79]. This methodology can also handle the winding heads in the stator if different bending formers are used for each coil [104]. A more visual representation is given in the center of figure 4.22, where the three coils have been integrated into a single drawing.

The next two configurations require a more controlled and specific inclination of the cross-section of the coils. For that reason, it is necessary to rotate the tape along its longitudinal axis. The torsion and rotation of superconducting tapes has already been considered and applied for the development of superconducting cables [105], [106] and it has been proposed on coils for magnet applications [78], [107].

The top and bottom inclined coils configuration can be built by considering a small torsion in two coils of the second arrangement. This proposal is shown in the 3D rendering presented on the right side of figure 4.22.

Finally, the star configuration can be realized by further exploring the torsion of the tapes, as shown in the sketch of figure 4.23. In this drawing, the three coils with different inclinations are mounted one on top of the other to build the 4 mm star arrangement in the straight section.

The findings of this research encourage the further development of non-planar and inclined coils based on the current state of the art in the magnet sector. Therefore, this investigation provides a solid base for further research activities that will enable these and more complex coils arrangements to face the technical challenges of superconducting renewable generators and magnet development.

5 Basic design of the coil and tape description

The previous chapters have introduced different tools to model and design coils for superconducting electrical machines. The developed tools set a base for electrical machine studies and provide approaches for AC loss reduction and 3D modelling of HTS coils. This development is complemented from the practical perspective in this and the consecutive chapters with the design, construction, and characterization of coils for electrical machine applications. This work is related to the SupraGenSys project, which aims to develop a new superconducting generator for a wind turbine application. The most beneficial configuration of stator coils from the AC losses point of view presented in the previous chapter is the star configuration. However, the construction of this stator winding requires a more complex analysis of the mechanical bending and torsion limits of the tape in the coil. Therefore, a coil with $2\,\mathrm{mm}$ tape was designed and constructed. The manufacturing of coils with such a small tape is still a challenge. For this reason, this represents the first step necessary to address more complex arrangements.

In this chapter, the HTS tape that is used in the coils is described first and measurements of the critical current of the tape are presented. This basic data is essential to build the models that allow estimating the critical current and AC losses as part of the characterization of the coil. The tape was supplied by two different manufacturers, S-Innovations LLC and Fujikura Europe Ltd. Then, the design of a coil is introduced as a scaled-down version of a stator coil of an electrical machine. A small test coil is built first to verify the manufacturing process. Afterwards, two versions of the scaled-down coil are manufactured, one

Table 5.1: Main characteristics of the HTS tape manufactured by S-Innovations LLC [108].

Dimensions	Width	$2\,\mathrm{mm}$
	Thickness	$0.12\,\mathrm{mm}$
Structure	Copper stabilizer	$20\,\mu\mathrm{m}$ per side
	Silver layer HTS side	$2\,\mu\mathrm{m}$
	Silver layer substrate side	$1\,\mu\mathrm{m}$
	Superconducting layer (YBCO)	$2.5\,\mu\mathrm{m}$
	Substrate (Hastelloy C-276)	$40\,\mu\mathrm{m}$
Electrical properties	Nominal I_c (77 K self-field)	60 A
	I_c measured by manufacturer (77.3 K self-field)	$I_\text{c-min} = 80\,\mathrm{A}$ $I_\text{c-avg} = 83\,\mathrm{A}$ $I_\text{c-max} = 88\,\mathrm{A}$
Mechanical properties	Minimum bending radius	$10\,\mathrm{mm}$

with the tape from S-Innovations LLC and one with the tape from Fujikura Europe Ltd.

5.1 Tape description and characterization

The first tape was manufactured by S-Innovations LLC. It is an YBCO tape $2\,\mathrm{mm}$ width $0.12\,\mathrm{mm}$ thickness with copper stabilizer on both sides [108]. The main characteristics of the tape are summarized in table 5.1, which also shows basic critical current measurements of the production batch and a brief description of the structure of the tape.

One of the most important parameters of the tape is the critical current (I_c) since it provides the maximum current capacity of the individual tape. Moreover, a proper characterisation of the I_c of the tape for different applied magnetic field amplitudes and directions is necessary to estimate the critical current of the coil, and to build models that allow studying the electromagnetic behaviour and estimate losses. For these reasons, a sample of the tape is taken for further characterisation. Figure 5.1

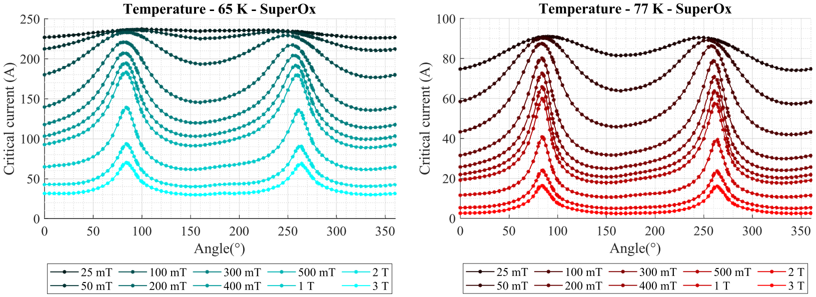

Figure 5.1: Measurements of the critical current of the HTS tape manufactured by S-Innovations LLC. An angle of 0° represents a field perpendicular to the wide face of the tape; an angle of 90° represents a parallel one.

Table 5.2: Main characteristics of the HTS tape manufactured by Fujikura Europe Ltd. [109].

Dimensions	Width	2 mm
	Thickness	0.11 mm
Structure	Copper stabilizer	20 µm per side
	Silver layer	2 µm
	Superconducting layer (GdBCO)	2 µm
	Buffer layer	0.7 µm
	Substrate (Hastelloy C-276)	50 µm
Electrical properties	Nominal I_c (77 K self-field)	50 A
	I_c measured by manufacturer	$I_{\text{c-min}} = 75$ A
	(77.5 K self-field)	$I_{\text{c-avg}} = 95$ A
Mechanical properties	Minimum bending radius	10 mm

shows the I_c measurement results of the sample. As it was shown in chapter 4, a reduction in temperature can have a positive impact on the AC losses of the HTS generator coils. Therefore, the critical current is measured at 77 K (liquid nitrogen) and lower temperatures. For simplicity, figure 5.1 shows only the I_c measurement results at 77 K and 65 K. These measurements were conducted in New Zealand by Robinson Research Institute, Victoria University of Wellington.

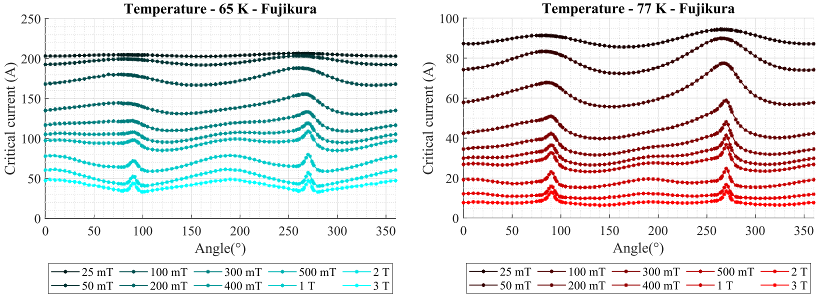

Figure 5.2: Measurements of the critical current of the HTS tape manufactured by Fujikura Europe Ltd. An angle of 0° represents a field perpendicular to the wide face of the tape; an angle of 90° represents a parallel one.

The second tape was produced by Fujikura Europe Ltd. It is an GdBCO tape $2\,\mathrm{mm}$ width $0.11\,\mathrm{mm}$ thickness with copper stabilizer on both sides [109]. The main characteristics of this tape are summarized in table 5.2. A sample is also taken in this case for I_c measurements under different magnetic field amplitudes and directions. Figure 5.2 shows the I_c measurement results at $77\,\mathrm{K}$ and $65\,\mathrm{K}$. These measurements were also conducted by Robinson Research Institute, Victoria University of Wellington.

5.2 Coil description

The basic design of the coil is presented in figure 5.3 and it is based on a scaled-down version (1:3) of the stator coil of an electrical machine. Chapter 4 shows that the most effective way to reduce the AC losses in the stator superconducting coils is by using an inclination of the coils that follows the behaviour of the magnetic field in the slot. This approach leads to the star configuration. However, this arrangement of the coils requires not only a mechanical analysis of the torsion and bending limits of the tape, but also a more complex manufacturing procedure. For these reasons, the coil presented in this work has a racetrack shape and represents one of the three types of coils necessary to build the star configuration.

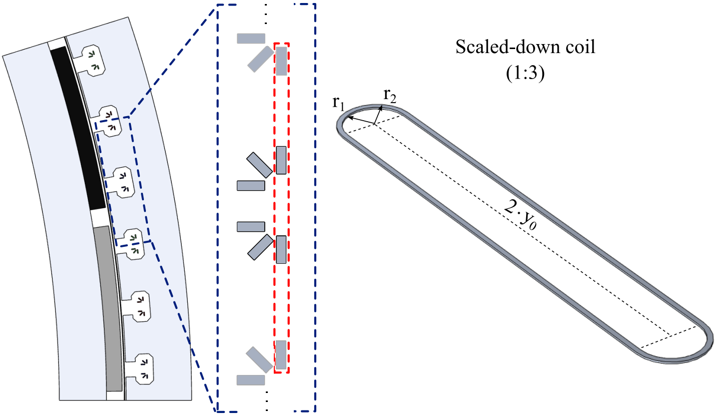

Figure 5.3: Geometry and basic design of the coil. The basic design is a scaled-down (1:3) version of the stator coils of an electrical machine. Since the construction of the star configuration requires a more detailed mechanical analysis, only planar coils are considered in this study. This planar coil represents one of the coils of the star configuration.

The geometry of the coil is shown on the right side of figure 5.3. The number of turns is 50, the same number of turns as the original coil of the electrical machine. The dimensions of the scaled-down coil are: $r_1 = 36\,\mathrm{mm}$, $r_2 = 42\,\mathrm{mm}$ and $2 \cdot y_0 = 500\,\mathrm{mm}$.

5.3 Coil construction and inductance

This subsection introduces the construction and estimation of the inductance in the scaled-down coils. Since the construction of a coil with a $2\,\mathrm{mm}$ tape can be a challenging task, a small test coil with 20 turns is manufactured first. The main objective is to verify whether the winding procedure is adequate, and does not produce a major degradation in the critical current. A picture of this first coil is presented on the left side of figure 5.4. A metallic former is used in this case to wind the HTS tape delivered by S-Innovations LLC. Copper connectors soldered to the tape allow a standard connection with cables to energize the coil. Voltage taps are added to each copper connector to measure the critical current.

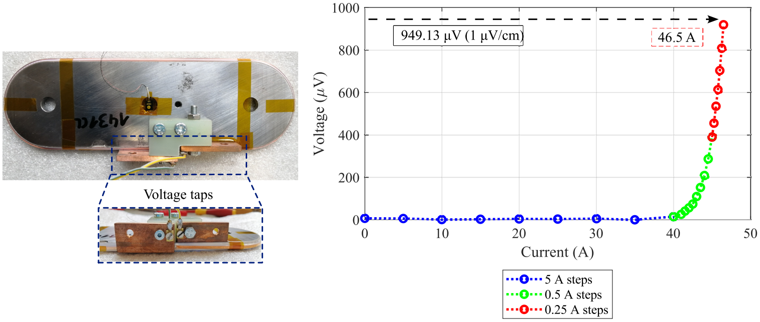

Figure 5.4: The small test coil (fabricated to verify the manufacturing process). A picture of the test coil is shown on the left, with a zoom on the voltage taps used to measure the critical current. The results of the critical current measurements are shown on the right.

The measurement results are presented on the right side of figure 5.4. The critical current of the coil is $46.5\ \mathrm{A}$ by considering a $1\ \mu\mathrm{V\,cm}^{-1}$ criterion.

Once the winding procedure is verified with the small test coil, the construction of the scaled-down coil starts with the tape provided by S-Innovations LLC. For simplicity, this coil is named A. In this case, the metallic former is replaced with G-10 to avoid induced currents that can increase the overall AC losses. Voltage taps are soldered to the tape and added to the copper connectors for critical current and connector resistance measurements (chapter 6). Due to instabilities during the winding process, the coil has only 48 turns (two turns less than expected). A picture of this coil is presented on the top side of figure 5.5. The second scaled-down coil is made with the tape delivered by Fujikura Europe Ltd. and uses the same type of former as in coil A. For simplicity, this coil is named B. Two small pieces of G-10 are added at both circular ends of this coil to improve the winding procedure. This approach allowed achieving the 50 turns. As it was done in coil A, voltage taps are added to the tape and in the copper connectors. A picture of this coil is presented on the bottom side of figure 5.5.

The inductance of coils A and B is first estimated with a stationary 3D finite element model developed in Comsol Multiphysics. The inductances estimated with

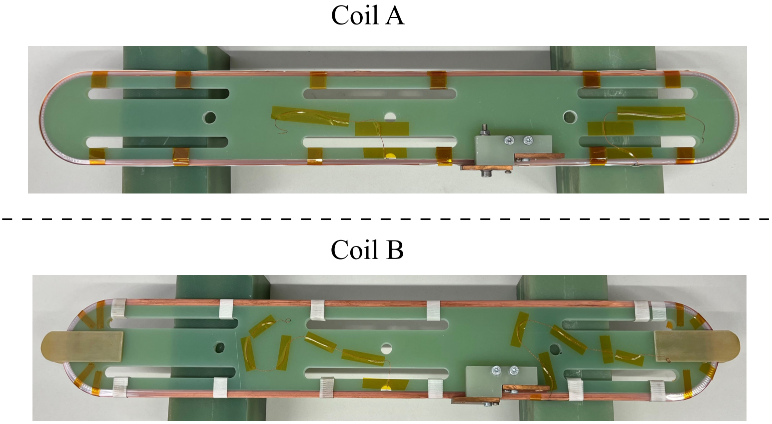

Figure 5.5: Coil A (top), made with 48 turns of 2 mm tape manufactured by S-Innovations LLC. Coil B (bottom), made with 50 turns of 2 mm tape manufactured by Fujikura Europe Ltd.

these simulations are $2.13\,\mathrm{mH}$ for coil A and $2.30\,\mathrm{mH}$ for coil B. These estimations are verified with measurements done with a LCR meter (Agilent U1733C) in cold (covered by liquid nitrogen) and warm (ambient temperature) conditions. The measured inductance of coil A is $L_{\text{cold}} = 1.97\,\mathrm{mH}$ ($L_{\text{warm}} = 2.01\,\mathrm{mH}$), which represents a deviation of $8.12\,\%$ in cold conditions ($5.97\,\%$ in warm conditions). The measured inductance of coil B is $L_{\text{cold}} = 2.18\,\mathrm{mH}$ ($L_{\text{warm}} = 2.26\,\mathrm{mH}$), which represents a deviation of $5.50\,\%$ in cold conditions ($1.77\,\%$ in warm conditions).

6 Critical current estimation and measurements

The estimations and measurements of the critical current of coils A and B are summarized in this chapter. The critical current of the coils is estimated first by using a 2D model that considers the middle of the straight section of the coil. Then, a brief description of the setup used to measure the critical current is presented, followed by the results of the measurements. The voltage in the coil is measured at four points (at the internal and external copper connectors, and voltage taps soldered on the tape close to the connectors). This approach allows measuring the voltage drop and resistance between the connector and the voltage tap in the tape, which includes the resistance of the soldered point between tape and connector.

6.1 Simulations

The critical current (I_c) in the coils is estimated with simulations based on the methodology presented in [29]. This approach was already used to estimate the critical current of HTS coils [77], [110], [111]. The methodology establishes two criteria to estimate the critical current in the coil, the maximum and the average. The maximum criterion indicates that I_c is the current that produces a voltage drop per unit length equal to the critical electric field ($E_\mathrm{c} = 1\,\mu\mathrm{V\,cm^{-1}}$) in at least one turn of the coil. On the other hand, the average criterion indicates that I_c is the current that produces an average voltage drop in the coil (all turns) equal to E_c [29].

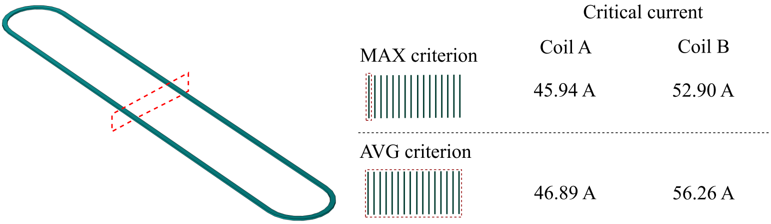

Figure 6.1: Summary of the 2D simulations to estimate the critical current in coils A and B.

A 2D model is used to calculate I_c by following a similar approach to [77], [93]. This model considers only the middle of the straight section of the coil. The critical current is estimated with the maximum criterion by monitoring the ratio between voltage drop per unit length and E_c in each turn. The voltage drop per unit length in each turn is multiplied by the length of the turn. The sum of this quantity divided by the total length of the coil is compared with E_c to estimate I_c according to the average criterion [29]. The modelling approach and results are summarized in figure 6.1. Both criteria give similar results with a maximum deviation lower than $3\,\%$ for coil A, and lower than $7\,\%$ for coil B.

6.2 Measurements

Since the critical current was already estimated with simulations, it can be measured in both coils and compared with the results of the 2D models. This section presents first a brief description of the measurement setup and location of the voltage taps. Then, the measurement results are introduced and compared with the simulations.

6.2.1 Setup and measurement procedure

The four point measurement technique is used to measure the critical current of the coil [112]. Before the measurements, the total length of the tape in the coil is calculated and multiplied by the critical electric field ($E_\mathrm{c} = 1\,\mu\mathrm{V\,cm^{-1}}$). This

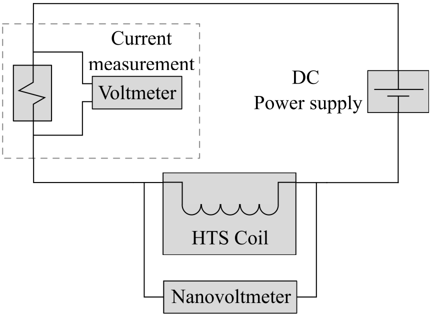

Figure 6.2: Sketch of the measurement system of the critical current of the coils.

provides the voltage drop in the coil at which I_c is reached. Then, the coil is placed in a cryostat and filled with liquid nitrogen. A direct current is injected into the coil, the voltage drop in the coil is measured with a nanovoltmeter and the current is measured with a series resistor and a voltmeter. A sketch of the measurement setup is shown in figure 6.2.

The current injected in the coil is increased slowly ($0.1\,\mathrm{A\,s^{-1}}$ ramp-rate) every 5 minutes. The transient behaviour due to the current ramp lasts usually less than 1 minute. However, the first 3 minutes of each measurement step are discarded to avoid any possible transient behaviour. The last 2 minutes are averaged in time and saved as the measurement result of each current step.

In the beginning, the voltage in the coil is close to zero. For this reason, the current is increased in $5\,\mathrm{A}$ steps. The voltage increases with a sharp behaviour once the injected current is close to the critical one. Therefore, the current steps are reduced to $0.5\,\mathrm{A}$ when the measured voltage is different than zero. This approach protects the coil from possible damage and provides a better resolution for the graphs and measurements. The current is increased until the voltage is close or equal to the $1\,\mathrm{\mu V\,cm^{-1}}$ criterion. Finally, the critical current is calculated as the linear interpolation of the last measurement points.

The voltage in the coil is measured at four different points, which are indicated in figure 6.3. There are two voltage taps soldered to the tape, named A1 and D2 in figure 6.3. The voltage between these two points is used to measure the critical

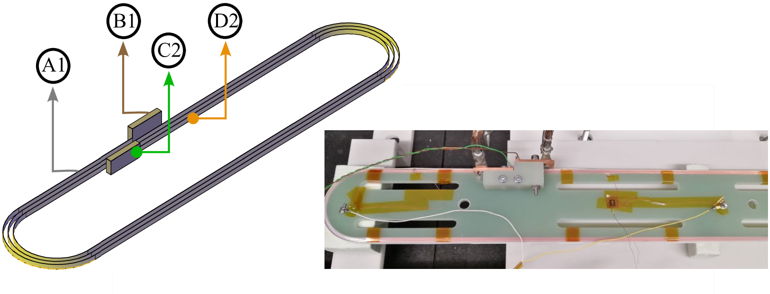

Figure 6.3: Diagram of the voltage taps connections in the coil to measure the critical current and terminal resistance.

current of the coil, since they do not consider the voltage drop in the copper (resistive) connectors. There are also voltage taps in each copper connector. The voltage tap located in the internal part is named C2 and the one located in the external part is named B1. The voltage between the internal copper connector (C2) and the internal voltage tap in the tape (D2) is used to measure the resistance between these two points, which includes the soldered point between the tape and the connector. The same approach is followed for the voltage taps located in the external part of the coil.

6.2.2 Results and comparison with simulations

The results of the critical current measurements in coil A are summarized in figure 6.4. As it was mentioned in the previous sub-section, the current is increased with $5\,\mathrm{A}$ steps at the beginning of the measurements (depicted in light red color) and with $0.5\,\mathrm{A}$ steps during the sharp increase of the voltage (depicted in dark red color). The $1\,\mathrm{\mu V\,cm^{-1}}$ criterion indicates that the critical current in coil A is reached once a voltage of $5974\,\mathrm{\mu V}$ is measured in the coil. The black dashed arrow in figure 6.4 shows this point in the graph, which indicates a critical current of $44.27\,\mathrm{A}$. This result is in good agreement with the simulations. It has a deviation of $3.77\,\%$ and $5.92\,\%$ with respect to the maximum and average criterion respectively, by considering the measurement result as the reference.

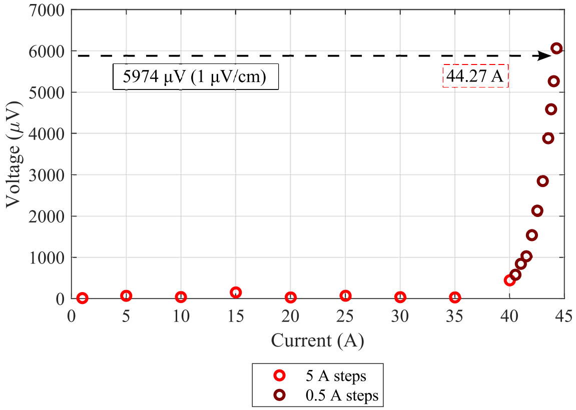

Figure 6.4: Result of the critical current measurement in coil A.

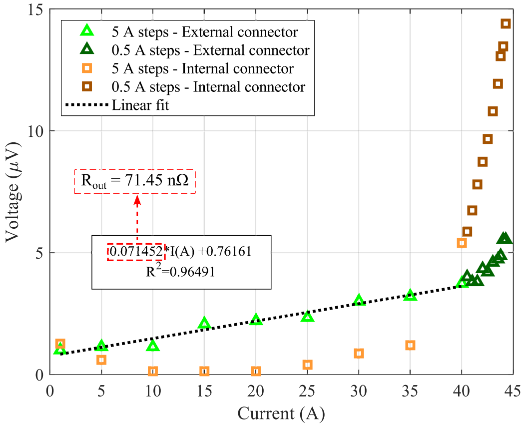

Figure 6.5: Result of the terminal resistance measurement in coil A.

Figure 6.5 shows the behavior of the voltage in the internal and external connectors of coil A during the critical current measurements. The voltage drop in the external connector (green triangles) exhibits a linear increase with the current during the first measurements, when the voltage in the coil (between the soldered taps) is close

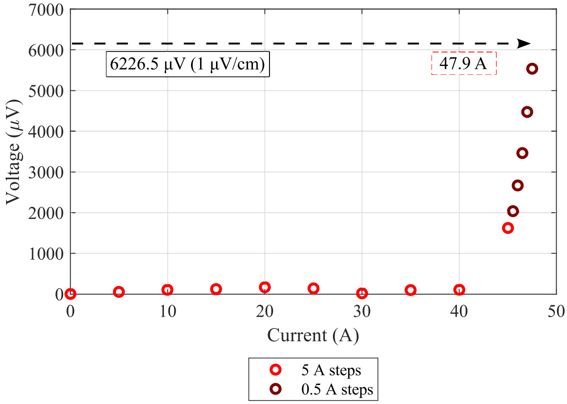

Figure 6.6: Result of the critical current measurement in coil B.

to zero. This linear increase in the voltage suggests a resistive behaviour that can be estimated with the linear fit presented in the graph. According to this approach, the resistance between the two external voltage taps is $71.45\,\mathrm{n\Omega}$. However, the voltage in the internal connector (orange squares) exhibits a random behaviour during the first measurements. This behaviour suggests that the resistance between the two internal voltage taps is so low that it can not be properly measured with this approach.

The results of the critical current measurements in coil B are presented in figure 6.6. In this case, the $1\,\mathrm{\mu V\,cm^{-1}}$ criterion indicates that the critical current in coil B is reached once a voltage of $6226.5\,\mathrm{\mu V}$ is measured in the coil. The black dashed arrow in figure 6.6 shows this point in the graph, which indicates a critical current of $47.9\,\mathrm{A}$. This result has a deviation of $10.44\,\%$ and $17.45\,\%$ with respect to the simulations and the maximum and average criterion respectively, by considering the measurement result as the reference.

The differences between the simulations and the critical current measurements in the coils can have several causes. First, the models are not a perfect representation of reality. They do not consider the non-uniformities of the critical current along

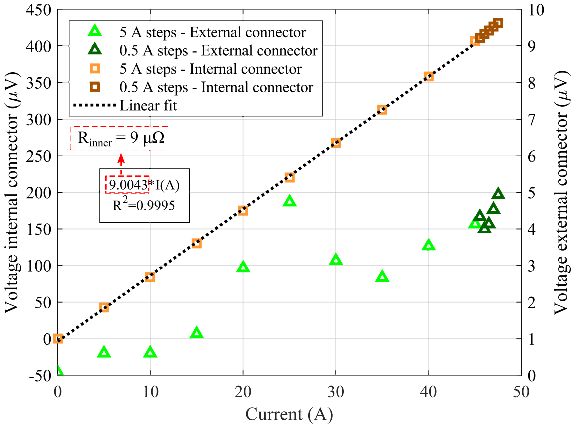

Figure 6.7: Result of the terminal resistance measurement in coil B.

length of the tape. Moreover, they are only a representation of the middle of the straight section of the coil. Therefore, an acceptable level of deviation is expected between the simulations and the measurement results.

The resistance in the internal and external copper connectors is also measured in coil B. Figure 6.7 presents the voltage drop in the internal connector (orange squares) and external connector (green triangles). In this case, the resistance between the two internal voltage taps is 9 µΩ. The voltage in the external connector exhibits a random behaviour, which indicates that the resistance between the two external voltage taps is so low that it can not be measured with this approach.

7 AC transport losses estimation and measurements

This chapter summarizes the AC transport losses estimations and measurements of coils A and B. First, the losses are estimated by using the homogenization of the T-A formulation in 3D and compared with its 2D counterpart. This provides an estimation of the level of the losses to be measured, and allows analyzing the electromagnetic behaviour of the coil. Then, the design and construction of a setup to measure AC transport losses with a calorimetric approach are presented. This setup is calibrated by using a set of resistors and the reproducibility is verified with multiple measurements. Finally, the AC transport losses are measured in coils A and B, and compared with the 3D simulation results.

7.1 Simulations

The first estimations of the AC transport losses in coils A and B are based on finite element models. These simulations provide an estimation of the levels of losses to be measured and represent a reference to compare with the measurement results. Moreover, the study of coils through simulations provides an electromagnetic analysis that is only feasible with numerical models.

Coils A and B have a racetrack shape. This geometry has two straight and two circular parts. Therefore, it can not be directly reduced into a 2D arrangement without a careful review. Moreover, the magnetic field tends to be higher in the inner part of the circular section [56], which can cause a higher current penetration in this zone. For these reasons, a 3D model was initially developed to analyze the

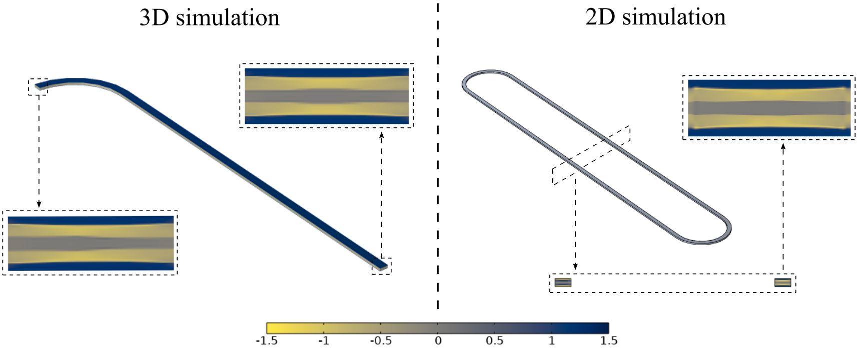

Figure 7.1: Normalized current density (J/J_c) in coil A for transport current ($f = 18\,\mathrm{Hz}$ and $I_\mathrm{peak} = 40\,\mathrm{A}$) when the current is equal to zero, after the first half period of the sinusoidal cycle. The results of the 3D simulation approach are shown on the left side, with a zoom in the middle of the straight and circular sections. The results of the 2D simulation approach are shown on the right.

coils. These simulations are based on the homogenization of the T-A formulation in 3D, described in detail in the previous chapters. As it was done in [56], only one-eighth of the coil is modelled by taking advantage of the symmetries.

The left side of figure 7.1 shows the behaviour of the normalized current penetration (J/J_c) obtained with the 3D simulation. The behaviour of the current penetration is very similar along the length of the coil. Based on these results, it can be assumed that a 2D simulation can also provide a good approximation, even if the geometry is not suitable for a 2D representation. For this reason, a 2D model based on the homogenization of the T-A formulation in 2D was built [60]. This model considers only the middle of the straight section of the coil as an infinite long arrangement. The normalized current penetration behaviour obtained with this 2D simulation is presented on the right side of figure 7.1. It is in good agreement with the 3D simulation, which confirms the previous hypothesis. A 2D simulation can provide a good approximation in this case.

The AC transport losses estimated for coil A with the 2D and the 3D simulations are summarized in figure 7.2. The results of the 3D model are presented in blue (triangle symbol) and the 2D model in red (square symbol). The relative error

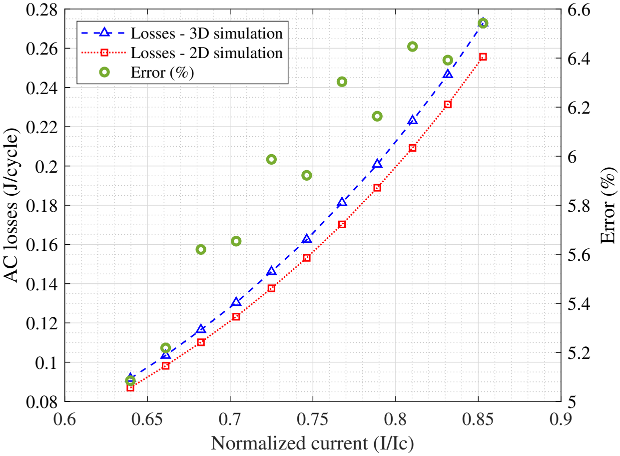

Figure 7.2: Results of the estimation of AC transport losses in coil A made with 3D and 2D models based on the homogenization of the T-A formulation. The green circles represent the relative error calculated by considering the 3D simulation as the reference.

calculated by considering the 3D simulation as the reference is depicted in green (circle symbol). In the 2D simulation case, the results are extended by considering an average turn length to estimate the total losses in the coil. The estimation of the losses done with the 2D and 3D models are in good agreement, with a maximum relative error lower than $7\,\%$.

The same modelling approach is followed to analyze coil B. The behaviour of the normalized current penetration (J/J_c) is presented in figure 7.3. The current penetration is also very similar along the length of the coil, and it is in good agreement with the 2D model. The estimations of the transport losses in coil B are summarized in figure 7.4. The 2D simulation results are similar to the results of the 3D models, with a maximum relative error lower than $4\,\%$. As a consequence, it can be concluded that the 2D simulation offers a good approximation of the transport losses and electromagnetic behaviour for coils A and B, despite the 3D geometry. Moreover, the 3D models have a computation time between one and two days for one and a half cycles of a sinusoidal transport current of a given amplitude, and the computation time of the 2D counterpart is lower than $30\,\mathrm{min}$.

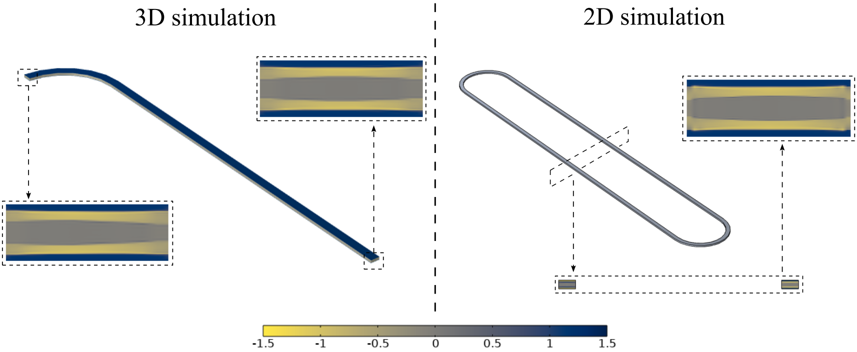

Figure 7.3: Normalized current density (J/J_c) in coil B for transport current ($f = 18\,\mathrm{Hz}$ and $I_{\mathrm{peak}} = 48$ A) when the current is equal to zero, after the first half period of the sinusoidal cycle. The results of the 3D simulation approach are shown on the left side, with a zoom in the middle of the straight and circular sections. The results of the 2D simulation approach are shown on the right.

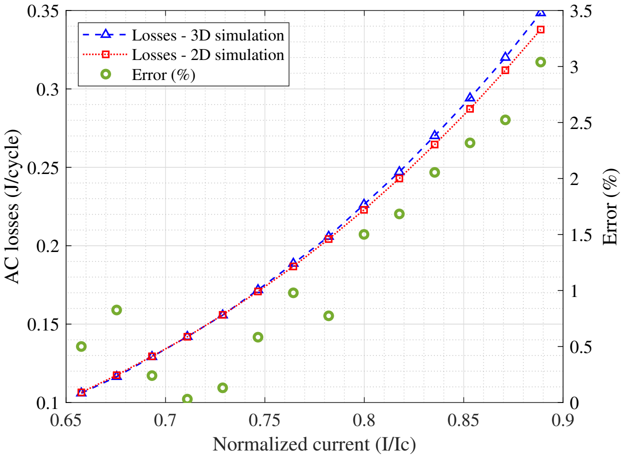

Figure 7.4: Results of the estimation of AC transport losses in coil B made with 3D and 2D models based on the homogenization of the T-A formulation. The green circles represent the relative error calculated by considering the 3D simulation as the reference.

7.2 Design and construction of a setup for calorimetric measurements of AC transport losses

There are two main methodologies commonly used to measure AC transport losses in HTS coils, the electric method and the calorimetric method [113], [114]. The electric method is based on the measurement of the current and the voltage in the coil. The voltage can be separated in two parts, a pure inductive component (90° shifted with respect to the current) and a loss component (in phase with the current) [115], [116]. The inductive component is usually larger than the loss component. Therefore, the efficiency of the method relies on cancelling the inductive component of the voltage to measure accurately the real component. For this purpose, a compensation circuit (pick-up coil or variable transformer) and a lock-in amplifier are generally used. However, the inductive component of the voltage in HTS coils can be several orders of magnitude larger than the AC loss component [117], [118]. Therefore, it can be difficult to cancel the inductive component. Moreover, the measurement approach can be strongly influenced by the electromagnetic conditions of the environment (metallic and ferromagnetic parts, energized magnets, experiments, or cranes close to the setup) [113], [119]. For these reasons, the calorimetric method was adopted in this case. This approach does not require a compensation circuit, it is not strongly influenced by the electromagnetic conditions of the environment and is faster to implement [119], [120], [121]. In the implemented calorimetric approach, the evaporation of the cryogen (nitrogen) due to the AC losses in the coil is collected and measured. The flow of evaporated nitrogen is translated into dissipated power by using a previously measured calibration curve. This approach is known as the boil-off method and has been applied to measure the AC losses in superconducting samples [122]; cables [123], [124], [125] and HTS coils under different operating conditions [121], [126], [127], [128], [129], [130].

The design, construction, and calibration of the calorimetric setup to measure the AC transport losses are presented in this section. Finally, the AC transport losses are measured in coils A and B, and compared with the simulation results presented in the previous section.

7.2.1 Components

The design and construction of the calorimetric setup to measure AC transport losses was divided into five main parts: cryostat and bubble collector, power supply, current measurement, flow measurement and data and acquisition system. Figure 7.5 shows a schematic of the setup with all its components. The coil is located inside a rectangular box that represents the cryostat and bubble collector, and it is energized through an AC voltage source and a current transformer. The current through the coil is measured with a Rogowski coil and the evaporation of the cryogen is directed into a flow sensor. The main variables are collected and recorded with the data acquisition system (indicated with dashed lines) and plotted in real-time on the computer. In this subsection, we will focus on the description, design, and selection of each of these components.

Figure 7.5 shows also a DC voltage source and a resistance that is used for calibration. This part of the setup will be explained in subsection 7.2.2, which describes the calibration of the setup and the reproducibility of the results.

7.2.1.1 Cryostat and bubble collector

One of the main sources of noise that can affect the flow of evaporated nitrogen is the interaction with the environment. Since the coil is at cryogenic temperature, there is a continuous heat transfer from the surroundings into the internal part of the cryostat. This phenomenon causes an additional evaporation of the cryogen that can influence the measurements. Moreover, the heat transfer depends on ambient conditions. It changes through the day and between different days and weeks (it can not be fully predicted or controlled). Therefore, the design of the cryostat and bubble collector plays a key role in the accuracy of the measurement setup.

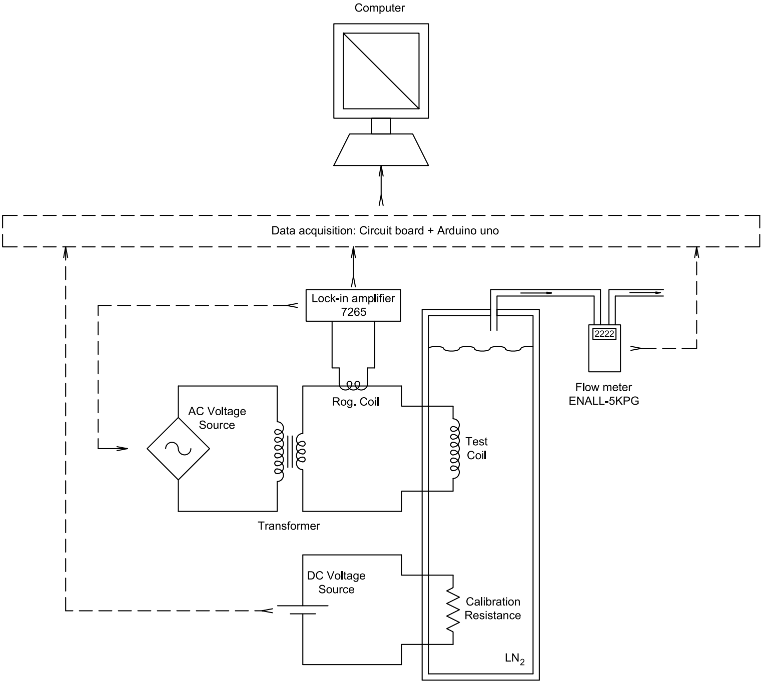

Figure 7.5: Diagram of the setup to measure AC transport losses in HTS coils through a calorimetric approach.

A possible way to minimize the influence of the environment on the measurements is to improve the thermal insulation of the cryostat. For this reason, an estimation of the heat transfer from the environment was done. For this estimation, we considered G-10 as a possible cryostat material due to its good thermal resistivity [131], and used the following equation which represents a 1D approximation that considers only the conduction heat transfer [132], [133], [134].

$$\dot{Q} = G(\theta_1 - \theta_2) \tag{7.1}$$

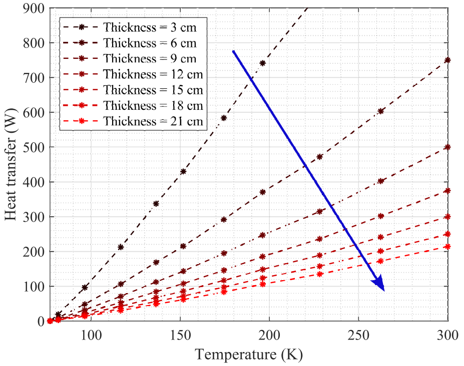

Figure 7.6: Results of the parametric study to estimate the conduction heat transfer from the environment done with a 1D approximation (equation (7.1)) by considering a G-10 $0.45\,\mathrm{m}^2$ slab, which represents the bottom part of the cryostat. The arrow indicates the direction in which the thickness of the cryostat increases.

In this equation, $\dot{Q}$ is the heat flow through a G-10 slab of area A_q and thickness L, θ is the integral of the temperature-dependent thermal conductivity, and $G = A_q/L$.

A parametric study was done by considering different thicknesses of the cryostat and ambient temperatures to estimate the conduction heat transfer through an area of $0.45\,\mathrm{m}^2$, which represents only the bottom part of the cryostat. Figure 7.6 summarizes the results of these estimations. The heat transfer is higher than $100\,\mathrm{W}$ for ambient temperatures higher than $250\,\mathrm{K}$, even if the thickness of the cryostat is increased up to $21\,\mathrm{cm}$. For this reason, a box inside a box approach was implemented to minimize the heat transfer and avoid a thick cryostat. During the experiments, the internal box is completely filled and the external box is partially filled with liquid nitrogen. This approach allows re-directing the heat transfer from the surroundings into an intermediate zone (space between external and internal box). Since this intermediate zone operates at cryogenic temperatures, the heat transfer to the internal part of the setup is reduced despite the thickness or material of the cryostat. Therefore, two commercial EPP (expanded polypropylene) boxes were used for this application.

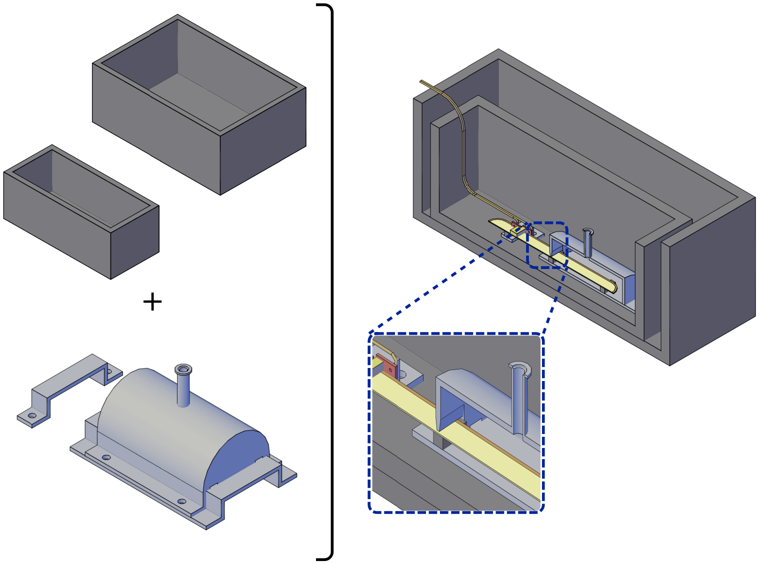

Figure 7.7: Assembly of the cryostat and bubble collector of the setup to measure AC transport losses in HTS coils through a calorimetric approach.

Figure 7.7 shows a 3D rendering of the assembly of the setup. The bubble collector has a semi-cylindrical shape that allows gathering the evaporated cryogen. It is raised $5\,\mathrm{cm}$ to avoid any additional heat transfer from the bottom of the setup. The bubbles are collected on half of the coil to avoid the evaporation coming from the connectors and to measure the losses only in the superconducting turns. These parts of the setup were 3D printed by using PA 12 GF (glass-filled fine polyamide), which withstands thermal stress and provides good sealing.

There are four small slots between the top and bottom parts of the bubble collector that allow the refilling of the cryogen. A basic estimation of the hydrostatic pressure was done and compared with the drop of pressure in the flow meter to ensure a proper flow of the gas. As a result, a minimum level of $25\,\mathrm{cm}$ of liquid nitrogen was kept in the inner box during all the measurements.

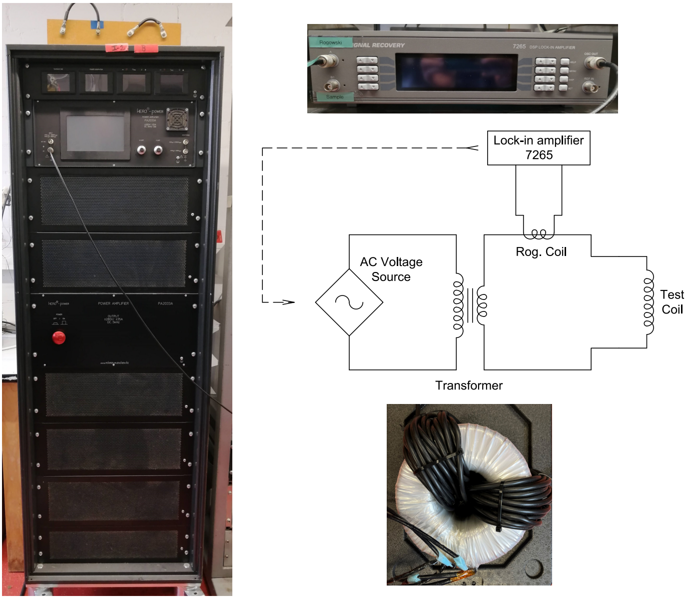

Figure 7.8: Schematic of the AC power supply used in the setup to measure AC transport losses in HTS coils through a calorimetric approach.

7.2.1.2 Power supply

The power supply consists of a lock-in amplifier (model 7265 manufactured by AMETEK®) that generates a reference sinusoidal signal (with variable amplitude and frequency) and measures the voltage in a Rogowski coil used to measure the transport current in the superconductive coil. The reference output from the lock-in amplifier is connected with a power amplifier (HERO®- power, model PA2033A) which provides the power to energize the coil. Finally, the output of the power amplifier is connected with the superconducting coil through a current transformer that provides insulation and adjusts the voltage and current capacity of the power supply to the requirements of the coil. A basic schematic of the power supply assembly is shown in figure 7.8.

7.2.1.3 Current measurement

The current that flows through the HTS coil is measured by using two approaches. The first one is represented in the power supply schematic (figure 7.8) and is based on a Rogowski coil that works as a current transducer. This coil captures the magnetic field around the cable that feeds the current into the coil. Therefore, the voltage at the terminals of the Rogowski coil is directly related to the current flowing through the cable. This voltage is measured with the lock-in amplifier and it is translated into current in ampere with a previously measured calibration curve. The current is also measured with a commercially available clamp meter (model U1212A manufactured by Agilent), which provides a local visual measurement of the current.

7.2.1.4 Flow measurement

The evaporated nitrogen is measured with a flowmeter manufactured by Teledyne Hastings Instruments, which consists of a power supply with a local indication of flow (model ENALL-5KPG) and a transducer (model HS-5KS) calibrated for nitrogen with a measurement range of 5 standard litres per minute [135]. The power supply also has an analog output of 0 to 5 V DC linearly related to the measured flow (0 to 5 standard litres per minute). This analog output is used by the data and acquisition system to plot and record the measurements.

The measurement principle of the flow sensor is described in figure 7.9. There is one heat sink and one temperature sensor on each side of the transducer. If there is no flow, the temperature measured at both points will be equal. If there is flow through the transducer, the temperature will be different. Therefore, the flow is measured based on this difference in temperature [135].

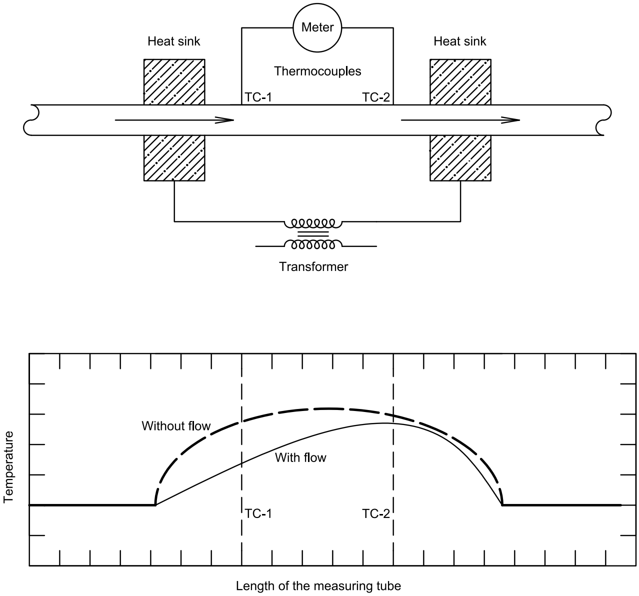

Figure 7.9: Diagram of the operating principle of the flow meter [135].

7.2.1.5 Data acquisition system

The main variables are collected in a small circuit board manufactured internally, which consists of a set of voltage dividers used to adapt the range of the voltage to be measured to the maximum analog voltage input of an Arduino Uno. This small board also incorporates one green LED that indicates the system is ON, one yellow LED that indicates the system is recording, and three red LEDs that provide warnings in over-voltage conditions. The board is connected to an Arduino Uno, which communicates with a computer to plot and record the signals (figure 7.10).

A graphical user interface (GUI) was created in MATLAB® to plot and record the collected data, as shown in the top right corner of figure 7.10. In this GUI, the user can give a name to the output file and select a possible delay between measurements. It also shows the current values of the flow in standard litre per minute, current in ampere, and DC voltage (used for calibrations) together with a

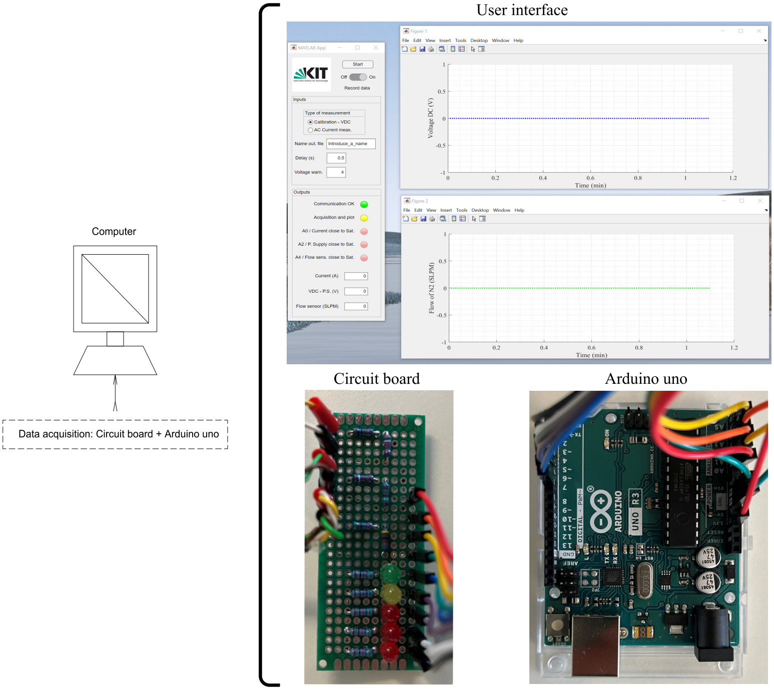

Type of measurement
● Calibration - VDC
○ AC Current meas.
Name out. file: Introduce_a_name
Delay (s): 0.5
Voltage warn.: 4
Current (A): 0
VDC - P.S. (V): 0
Flow sensor (SLPM): 0

Figure 7.10: Data acquisition system of the setup to measure AC transport losses.

visual representation of the LEDs included in the small circuit board. A plot of the recorded values is shown while the program is recording, and when it stops a file (in Microsoft Excel format) is created with all the recorded data.

7.2.2 Calibration and reproducibility

Before measuring the AC transport losses in the coil, it is necessary to build a calibration curve that allows translating the evaporation of nitrogen (in standard litre per minute) into dissipation (in watt). Moreover, it is important to check the reproducibility of the measurements by repeating and comparing different

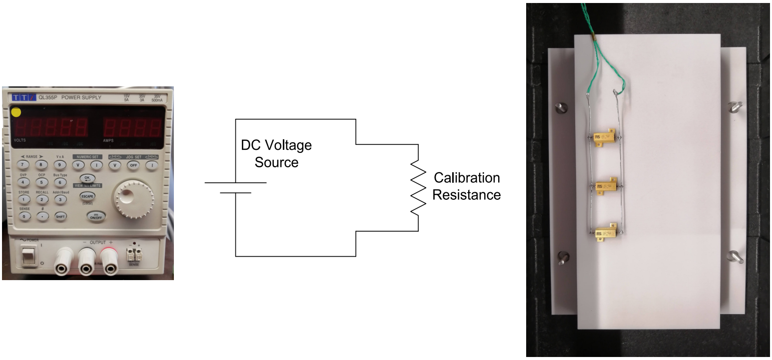

Figure 7.11: Schematic of the calibration circuit of the setup to measure AC transport losses.

measurements under different conditions. This verifies the influence of the environment on the measurements and the reliability of the measurement setup. In this subsection, the construction of the calibration curve and the verification of the reproducibility are presented. Since these are the first measurements with the setup, the post-processing procedure and load cycles of the measurements are described.

7.2.2.1 Calibration resistor

The calibration curve of the setup is built by producing a controlled dissipation of energy inside the bubble collector. For this reason, an arrangement of three $25\,\mathrm{W}$ $39\,\Omega$ resistors connected in parallel is used. The resistance of the arrangement is measured previously in cold (covered by liquid nitrogen) and warm (ambient temperature) conditions multiple times with variations lower than $0.3\,\Omega$. This configuration of resistors is energized with a DC power supply (model QL355P manufactured by Aim and Thurlby Thandar Instruments). Since the value of the equivalent resistance is known, the dissipation of energy can be controlled by changing the DC voltage in the power supply. A picture of the resistors and a schematic of the calibration circuit are shown in figure 7.11.

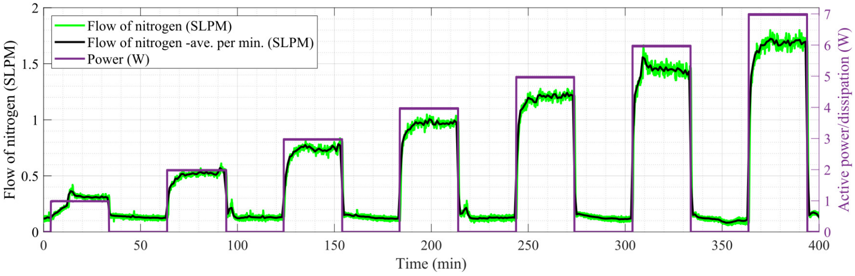

Figure 7.12: Measurement of the evaporation of nitrogen due to the dissipation in the calibration resistance.

7.2.2.2 Load cycle and post-processing technique

The measurements are structured in load cycles, by following a similar approach to the one introduced in [124]. Each load cycle represents one value of dissipated energy and lasts $60\,\mathrm{min}$. During the first 30 minutes, the DC voltage (or AC current in the coil) remains constant at a specific value and the evaporation of the cryogen related to the dissipated energy in the resistor (coil) is measured. Then the DC voltage (AC current in the coil) is reduced to zero. During the next $30\,\mathrm{min}$, the background flow is measured. This approach creates a clear distinction between load cycles, allows re-filling of liquid nitrogen between measurements and studying the background flow during the whole measurement time.

Figure 7.12 presents the behaviour of the flow of evaporated cryogen in one set of measurements done with the calibration resistors. The active power (purple line and right axis) in the resistors was changed from $1\,\mathrm{W}$ up to $7\,\mathrm{W}$. The flow of evaporated nitrogen (light green and left axis) shows a continuous fluctuation during the whole measurement range. Similar variations were reported in other application that followed the same measurement principle [124], [125]. This behaviour can be related to how the bubbles are created and collected in the measurement chamber. The dark green plot in figure 7.12 shows the behaviour of the average per minute flow of evaporated cryogen. There is still a significant fluctuation even if we take the average per minute. Therefore, a more complex

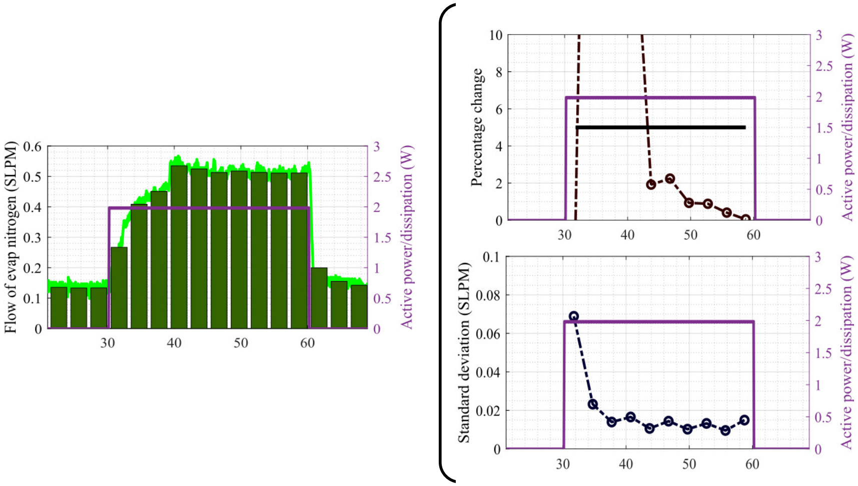

Figure 7.13: Post-processing of one load cycle of the evaporation of nitrogen due to the dissipation in the calibration resistance.

post-processing technique must be implemented to properly asses the uncertainty in the measurements.

For the post-processing of the data, each $30\,\mathrm{min}$ section of the load cycle was subdivided into 10 time slots of 3 minutes each. The average value of the evaporated nitrogen was calculated in each time slot, as shown on the left side of figure 7.13, where the instantaneous flow is in light green and the average values in dark green bars. In this plot, we can see a transient behaviour that starts once the arrangement of resistors is energized. The percentage variation of the average flow between time slots was calculated to establish the beginning and end of the transient behaviour. For this purpose, a $5\,\%$ criterion is used. If the percentage variation is lower than $5\,\%$, we can say that a steady state was reached. If the percentage variation is higher than $5\,\%$, we can say that we still have a transient behaviour.

The standard deviation (σ) is also calculated in each time slot to assess the uncertainty in the measurements. As shown in the bottom right corner of figure 7.13, the standard deviation also exhibits a transient behavior that ends once the percentage variation of the average flow is below $5\,\%$. After this point, it only has very small fluctuations. Finally, the measurements can be written as an average value plus and minus two times the standard deviation, which represents an uncertainty range that includes $95.4\,\%$ percent of the data in the last time slots if we assume a normal distribution [136].

7.2.2.3 Reproducibility

The measurements of evaporated nitrogen related to $1\,\mathrm{W}$ and $2\,\mathrm{W}$ of dissipation in the calibration resistors were repeated to verify the reproducibility of the results under different ambient conditions and resistors arrangements. Figure 7.14 shows the arrangements of resistors used to verify the reproducibility. The resistance of each arrangement is measured in cold (covered by liquid nitrogen) and warm (ambient temperature) conditions. For simplicity, the configuration of resistors shown in figure 7.11, and used in the set of measurements presented in figure 7.12, is named configuration A. This arrangement is modified by adding two small blocks of styrodur in configuration B. The main objective of this change is to raise the three resistors by $1.5\,\mathrm{cm}$ to allow liquid nitrogen at the bottom of the arrangement and test a different position of the resistors in the measurement chamber. Finally, configuration C is made with only one single resistor. This allows verifying whether changes in the number of resistors have an impact on the measurements. Each configuration is measured on different weeks. After each measurement, the whole setup is disassembled, dried, cleaned, and re-assembled.

Table 7.1 presents the results of the measurements of evaporation of cryogen due to the dissipation of energy in the configurations of resistors used to verify the reproducibility. All the measurements are in good agreement with each other. The differences between measurements are small and within the uncertainty range. These results confirm the reliability of the measurement setup by reproducing the same results under different ambient conditions, different weeks and with different configurations of calibration resistors.

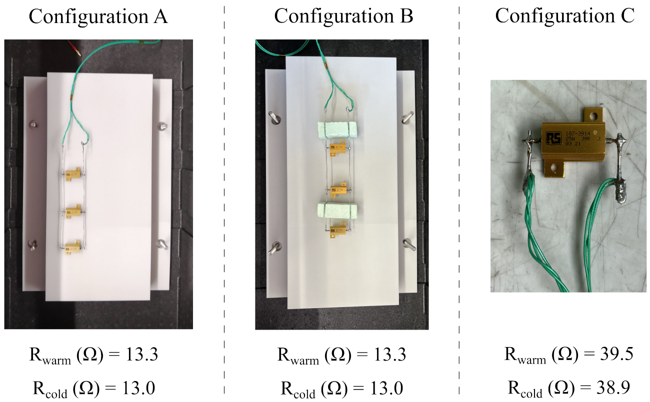
Configuration A

R_{warm} (Ω) = 13.3

R_{cold} (Ω) = 13.0

Configuration B

R_{warm} (Ω) = 13.3

R_{cold} (Ω) = 13.0

Configuration C

R_{warm} (Ω) = 39.5

R_{cold} (Ω) = 38.9

Figure 7.14: Configuration of resistors used to verify the reproducibility of the measurements.

Table 7.1: Evaporation of cryogen due to the dissipation of energy in the configurations of resistors used to verify the reproducibility.

Configuration	Power	Average flow	Uncertainty - $2 \cdot \sigma$
	(W)	(SLPM)	(SLPM)
A	1	0.31	0.02
	2	0.51	0.02
B	1	0.32	0.02
	2	0.52	0.02
C	1	0.31	0.02
	2	0.52	0.04

7.2.2.4 Calibration curve

After the reproducibility of the measurements is verified, we can proceed and build the calibration curve. For this purpose, the post-processing procedure described previously is followed to analyze the data shown in figure 7.12. The background flow was stable around an average value of 0.12 with an uncertainty of 0.02 standard litre per minute.

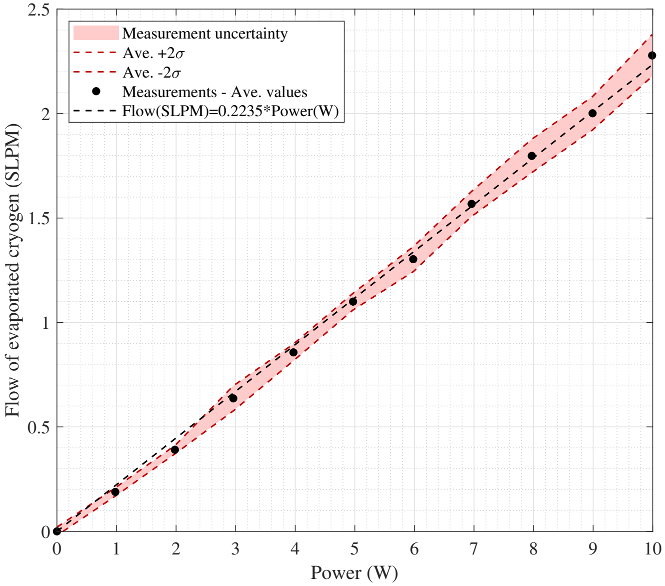

Figure 7.15: Calibration curve of the setup to measure AC transport losses.

Figure 7.15 presents a plot of the calibration curve once the background flow is subtracted from the measurements. The black dots represent the average values, and the dashed red lines and light red zone represent the uncertainty in the measurements. The dashed black line presents a linear fit to the experimental data with a coefficient of determination of 0.9985. This linear fit provides a practical relation between the dissipated energy in the measurement chamber and the average flow of evaporated nitrogen, which means that 1 W of dissipation inside the measurement chamber produces a flow of 0.2235 standard litres per minute of evaporated nitrogen.

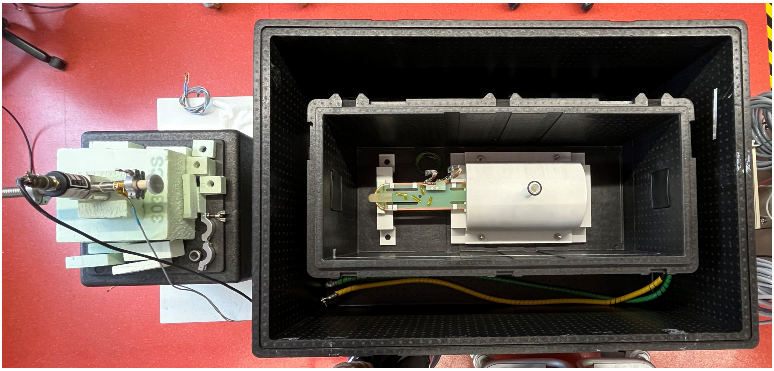

Figure 7.16: Setup to measure AC transport losses with an HTS racetrack coil inside. From left to right, we have the flow transducer, internal and external cryostat (black boxes), and bubble collector (white 3D printed parts).

7.2.3 Measurement of AC transport losses in HTS coils and comparison with simulations

Since the setup was already designed, built, and calibrated, the following step is to measure the AC transport losses in a coil. Figure 7.16 shows the setup layout with a HTS coil inside. The black boxes are the internal and external cryostats, and the white part is the 3D-printed bubble collector.

The first measured coil was coil A. It was energized with an AC sinusoidal transport current of variable amplitude and a frequency of $18\,\mathrm{Hz}$. The evaporation of the cryogen was measured and the data was post-processed by following the procedure described in the previous sub-sections.

The AC transport loss measurements in coil A are summarized in figure 7.17, which presents the AC losses as a function of the normalized current density (J/J_c). The measurement data was normalized by considering the measured critical current with a $1\,\mathrm{\mu V\,cm^{-1}}$ criterion $(44.27\,\mathrm{A})$ and the simulation results were normalized by considering the critical current calculated with the 2D model and average criterion $(46.89\,\mathrm{A})$. In this graph, the losses estimated with 3D

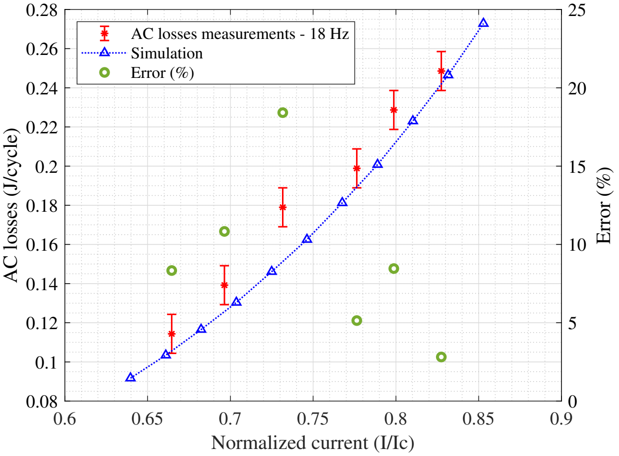

Figure 7.17: AC transport losses measurements in the coil A, and comparison with simulation results calculated with the homogenization of the T-A formulation in 3D.

simulations are presented in blue and the measurements in red. Each average flow measurement (F) was translated into watt by using the following equation,

$$P(\mathrm{W}) = \frac{2}{0.2235\,\frac{\mathrm{SLPM}}{\mathrm{W}}} \cdot F(\mathrm{SLPM}). \tag{7.2}$$

The propagation of the uncertainty (δP) was calculated as described in [136]:

$$\delta P = \frac{d(P)}{dF} \cdot \delta F \tag{7.3}$$

$$\delta P = \frac{4}{0.2235\,\frac{\mathrm{SLPM}}{\mathrm{W}}} \cdot \sigma_{\text{flow}}(\mathrm{SLPM}). \tag{7.4}$$

In these equations, δF represents the uncertainty in the flow measurements calculated as two times the standard deviation ($2 \cdot \sigma_{\text{flow}}$).

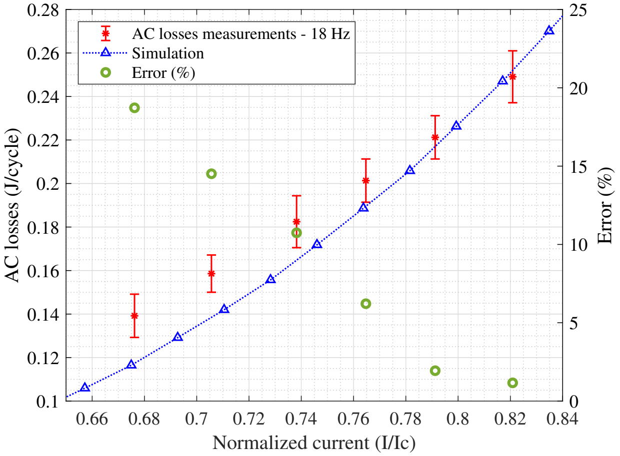

Figure 7.18: AC transport losses measurements in the coil B, and comparison with simulation results calculated with the homogenization of the T-A formulation in 3D.

Figure 7.17 also shows the relative error in the measurements by considering the 3D simulation results as the reference. The measurements are in good agreement with the simulations with a maximum error lower than $19\,\%$.

Figure 7.18 presents the results of the transport loss measurements in coil B. As it was done for coil A, the measurement data was normalized by considering the measured critical current with a $1\,\mu\mathrm{V\,cm^{-1}}$ criterion ($47.9\,\mathrm{A}$) and the simulation results were normalized by considering the critical current calculated with the 2D model and the average criterion ($56.26\,\mathrm{A}$). The measurements are in good agreement with the simulations with a maximum error lower than $19\,\%$. These differences between simulations and experimental results can have several causes, from the uncertainty in the measurements to the non-uniformities along the length of the tape, which is not considered in the simulations.

8 Conclusion and outlook

The 3D T-A homogenization modelling technique was developed for the analysis of coils with complex geometries. This modelling approach was used to study the behaviour of superconducting coils under different operating conditions. The proposed normal vector approach based on a curvilinear coordinate system definition allowed an easier implementation (in comparison with the currently available 3D H homogenization) despite the complexity of the geometry. Therefore, it represents a practical tool for the analysis of HTS devices with complex shapes at low frequencies. The modelling technique was validated first with the circular coils presented in [47]. In this first case study, the estimation of transport losses obtained with the homogenization of the T-A formulation in 3D was compared with 2D simulations (maximum error lower than $6.23\,\%$) and measurement results (maximum error lower than $35\,\%$). Then, the racetrack coil studied in [56] was modelled with the developed technique, and the results were compared with the 3D H homogenization. Subsequently, a saddle coil was analysed, which represented a case study with potential applications in the magnet and superconducting electrical machine sectors. The operating conditions under study were AC transport current and AC transport current with AC externally applied magnetic field. The results were compared with a 2D T-A homogenized model, which gave a good approximation of the losses for the first operating condition but cannot be used for the electromagnetic analysis of the second one. The validity of this 2D approximation can be affected by the length of the straight section of the coil, in comparison with the curved one. Therefore, 2D simulation results cannot be directly extrapolated to more complex geometries. Finally, the 3D simulation studies were complemented with the analyses of a twisted coil, a geometry without straight parts. This case has potential applications in the fusion energy sector.

The operating condition considered was DC transport current. For this reason, the ramp-up/down process was simulated.

For most of the coils considered in this work, the losses due to AC or the ramp-up/down process can be estimated with a 2D model. This approach provides a good approximation and offers a great reduction of degrees of freedom due to the reduction of dimension. Therefore, it represents a good compromise between accuracy and computation time. However, the behaviour of the coils due to transport current and external magnetic field can be more complex. For this operating condition, the 3D model can provide a better estimation of losses and detect zones with local saturation of current, as was seen in the saddle coil simulations. The operating conditions of HTS coils in the majority of applications (such as electrical machines and fusion experiments) involve transport current and magnetic field. In these cases, the study of the interaction with other coils, magnets, and materials in intricate 3D geometries is only feasible with a 3D model. The presented analyses show the versatility of the modelling approach and its efficiency for AC loss estimation in coils. Moreover, the studies support and encourage the modelling and development of HTS coils with complex geometries, necessary to overcome the technological challenges of superconducting devices in multiple fields and applications.

The electromagnetic behaviour of synchronous superconducting machines was analysed by using FEM models based on the T-A formulation. The current distribution in the stator winding was calculated by following a proposed methodology based on the building model process. This allows us to improve superconducting machine designs by reducing the losses in superconducting coils with a detailed analysis.

The modelling approach was implemented for a 10 MW generator with permanent magnets in the rotor and superconducting coils in the stator. Two designs were considered at the beginning of the study. First, a design with iron teeth and four coil layers per slot was analyzed. Then, a slotless solution was modelled and a small reduction in losses was achieved. Based on these two results, a new design was proposed with iron teeth and three coil layers per slot. Then, an AC loss reduction study in the stator HTS winding was done based on a comprehensive analysis of the electromagnetic behaviour of the coils. The AC loss reduction was classified into three main strategies: non-planar coils, tape width reduction, and temperature reduction. The first approach can provide up to an $80\,\%$ reduction in losses and a better average power density dissipation in the HTS coils of the synchronous machine under study. A reduction in the width of the tape from $4\,\mathrm{mm}$ to $2\,\mathrm{mm}$ can reduce the losses by $45\,\%$ for the typical arrangement. However, it can not improve the power density dissipation distribution. The analysis was complemented with a sensitivity study over lower temperatures as a strategy to increase the critical current and reduce AC losses in the coils. Particular interest was given to the typical arrangement and star configuration with $2\,\mathrm{mm}$ tape. From these calculations, it can be concluded that even if the critical current of the tape is doubled, or the operating temperature of the coils is decreased down to $5\,\mathrm{K}$, with the typical arrangement we still will not be able to reach the level of losses that were achieved with the star configuration at $65\,\mathrm{K}$. Moreover, we will keep potential hot spots in the cross-section of the coil, which could be avoided in the design stage with the uniform distribution of losses achieved with the star arrangement. This configuration allows better usage of the superconducting tape capacity by achieving a more uniform current penetration in tapes and avoiding saturation of individual coils. If the efficiency of the cooling system is considered, the level of losses in the typical arrangement can compromise the feasibility of the design by decreasing the efficiency and increasing the cost of the cooling system.

These findings encourage the development of non-planar and inclined coils for generators and can be used as a base for further research and development that will enable these and more complex coils arrangements to face the technical challenges of superconducting generators for wind turbine applications.

In the last part of this work, the design, construction, and test of a setup for the calorimetric measurement of AC transport losses were presented. The measurement approach is based on the boil-off method. A bubble collector was designed and 3D printed to guide the evaporation of the cryogen into a flow meter. A box-inside-a-box solution was implemented to minimize the influence of the environment, and a statistical analysis of the results was done. This statistical treatment of the fluctuations in the evaporated cryogen is new for this type of measurement, and it allows expressing the variability in the flow as uncertainty in the measurements.

The reproducibility of the measurements was verified with different arrangements of resistors during the calibration stage. The measurements were in good agreement with a maximum deviation of 0.01 SLPM. Each set of measurements was done in a different week after the whole setup was dissembled, dried, cleaned, and re-assembled. The reported deviations are within the uncertainty range of the measurements. The excellent reproducibility of the results under different conditions represents an exceptional outcome in the field of AC loss measurements based on a calorimetric approach (boil-off method) since the strong influence of the environment can cause fluctuations that are not easy to reproduce. These results can be related to the implemented creative solutions, such as the box-inside-a-box approach and the statistical analysis. The first reduces the influence of the environment and the second allows assessing the maximum level of deviation that can be accepted in the measurements to agree that the results are the same. Moreover, the 3D-printed bubble collector solution introduces flexibility in the measurement approach. Therefore, it can be easily extended to more complex geometries and applications.

The construction and characterisation of two HTS racetrack coils were introduced as the first measurement cases. The inductance and critical current of the coils were first estimated with finite-element models and compared with measurements. A good agreement between simulations and measurements was found in both cases. The critical current had a maximum deviation of $5.92\,\%$ in the case of coil A, and $17.45\,\%$ in the case of coil B. The inductance had a maximum deviation of $8.12\,\%$ in coil A, and $5.50\,\%$ in coil B. The coils were modelled by using the homogenization of the T-A formulation in 2D and 3D to estimate AC transport losses. The normalized current penetration and loss estimations were shown and compared between both models, where a maximum relative error lower than $7\,\%$ was found for the 2D AC loss approximation in coil A, and $4\,\%$ in coil B. Finally, the AC transport losses were measured in the coils and a good agreement with the simulations was found (maximum error lower than $19\,\%$). These results confirm the reliability and accuracy of the measurement setup. Moreover, the results of this thesis expand the current knowledge of HTS coils for electrical machines with the development of new simulation approaches, stator winding configurations with a substantial reduction of losses, and creative measurement methods, which will enable more compact and efficient solutions to face future technological challenges.

Based on the results presented in this work, the research can be extended in multiple directions to improve the current state of the art of HTS coils for electrical machine applications. The star configuration has great potential to achieve a significant reduction in AC losses, which can enable the future fully superconducting electrical machines with innovative stator winding. However, mechanical and thermal studies are necessary to ensure proper manufacturing and operation of this coil configuration. The developed homogenization of the T-A formulation in 3D can be combined with additional modeling strategies, such as multiscale approach, to analyze larger and more complex problems. This methodology may allow analyzing end-effects in small superconducting electrical machines and improve the overall electromagnetic study of superconducting devices in multiple fields. Finally, the calorimetric measurement technique of AC losses in HTS coils can be extended or improved in two main directions. The first one is based on the upgrading of the current setup either by improvements of individual components or incorporation of sensors and instrumentation that allows having more data, which will eventually lead to more detailed analysis and possible improvements. The second alternative is tied to the measurement of coils with different geometries, different operating conditions, or applications. In this case, the flexibility added by the 3D-printed bubble collector plays a key role, since it can be easily adapted for each geometry or application. Therefore, it can be concluded that this thesis not only improves the current state of the art but also provide the tools for further research and development of HTS coils.

A Applications for the estimation of losses in an infinite stack of tapes based on analytical solutions

Two applications were developed in MATLAB to estimate AC transport losses and AC losses due to uniform perpendicular applied magnetic field in infinite stacks of superconducting tapes. The calculations are based on analytical equations presented in [42]. The operating conditions considered for the AC loss estimations do not reflect the complex electromagnetic environment of the superconducting stator winding of an electrical machine. However, the implementation of these analytical equations in MATLAB applications provides practical tools to compute basic estimations and to understand the behaviour of the losses in infinite stacks of tapes. This appendix presents a brief summary of the applications, considerations of the calculations and main functions included in the MATLAB code.

A.1 Application for the estimation of AC losses in an infinite stack of superconducting tapes carrying AC transport current

This application solves the following equation developed by Y. Mawatari [40] to estimate the hysteretic AC loss in Joule per cycle per Meter in a superconducting strip in an infinite stack arrangement,

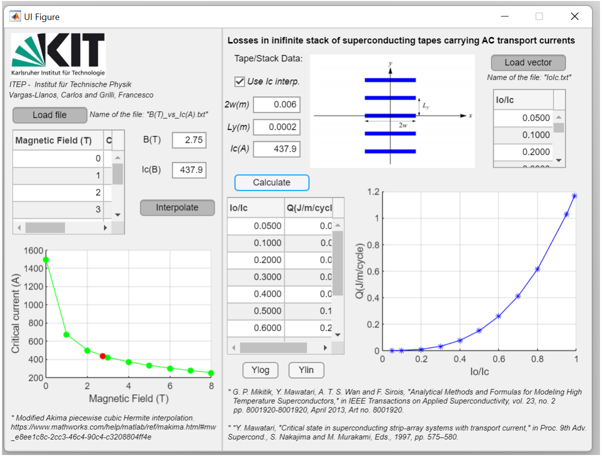

ITEP - Institut für Technische Physik
Vargas-Llanos, Carlos and Grilli, Francesco

Name of the file: "B(T)_vs_Ic(A).txt"

Magnetic Field (T)	C
0	
1	
2	
3	

B(T) 2.75
Ic(B) 437.9

* Modified Akima piecewise cubic Hermite interpolation. https://www.mathworks.com/help/matlab/ref/makima.html#mw_e8ee1c8c-2cc3-46c4-90c4-c3208804ff4e

Losses in inifinite stack of superconducting tapes carrying AC transport currents

Tape/Stack Data:
☑ Use Ic interp.
2w(m) 0.006
Ly(m) 0.0002
Ic(A) 437.9

Name of the file: "IoIc.txt"

Io/Ic
0.0500
0.1000
0.2000

Io/Ic	Q(J/m/cycl
0.0500	0.0
0.1000	0.0
0.2000	0.0
0.3000	0.0
0.4000	0.0
0.5000	0.1
0.6000	0.2

* G. P. Mikitik, Y. Mawatari, A. T. S. Wan and F. Sirois, "Analytical Methods and Formulas for Modeling High Temperature Superconductors," in IEEE Transactions on Applied Superconductivity, vol. 23, no. 2 pp. 8001920-8001920, April 2013, Art no. 8001920.

* *Y. Mawatari, "Critical state in superconducting strip-array systems with transport current," in Proc. 9th Adv. Supercond., S. Nakajima and M. Murakami, Eds., 1997, pp. 575–580.

Figure A.1: Graphical User Interface (GUI) of the application made to estimate AC losses in an infinite stack of superconducting tapes carrying AC transport current based on analytical solutions.

$$\frac{Q}{Q_c} = i_0^2 \int_0^1 (1-2s)\ln\left[\frac{\cosh^2(\pi\omega/L_y)}{\cosh^2(\pi i_0 s\omega/L_y)} - 1\right] ds. \tag{A.1}$$

The superconducting strips in the stack carry a transport current I_t that oscillates quasi-statically between $+I_0$ and $-I_0$, with $Q_c = \mu_0 I_c^2/\pi$ and $i_o = I_0/I_c < 1$. In these equations, $2w$ is the width of the strip, L_y the separation between strips and I_c the critical current.

Figure A.1 shows the Graphical User Interface (GUI) of the application, which is subdivided from left to right in two parts. First, a data file that contains the behaviour of the critical current as a function of the magnetic flux density can be uploaded to estimate the critical current of the tape, based on the magnetic field and an interpolation of the data. Then, a vector containing the normalized values of the transport current amplitudes and general dimensions of the arrangements can be uploaded on the top right side of the GUI. Finally, the computation of the losses can be done when the calculate bottom is pressed.

The MATLAB code of the function used to solve equation (A.1) is

```
function [Qi] = Q_YM(ic,ip,tape_w,separation)

w=tape_w/2;
Ic=ic;
io=ip;
Ly=separation;

mu0=4*pi*(10^-7);
Qc=mu0*(Ic^2)/pi;

fun = @(x) x;
Q = integral(fun,0,1);

funQ = @(s) (1-2*s).*log(((cosh(pi*w/Ly).^2).
    /(cosh(pi*io*s*w/Ly).^2))-1);
Qi = Qc*(io^2)*integral(funQ,0,1);
end .
```

A.2 Application for the estimation of AC losses in an infinite stack of superconducting tapes under perpendicular magnetic field

The development of this application and its user interface is very similar to the previous one. Figure A.2 presents the GUI. The left side is used to estimate the critical current of the tape based on measurement data, and the right side for AC loss calculation. The main difference is that the vector to be uploaded on the right side represents now perpendicular external magnetic field.

The equation used in this case was developed also by Y. Mawatari [41],

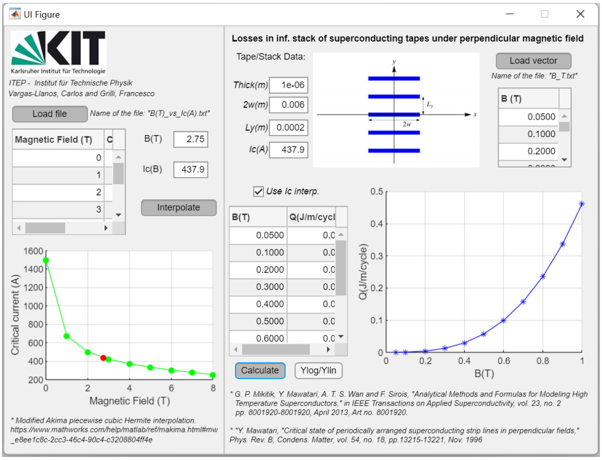

ITEP - Institut für Technische Physik
Vargas-Llanos, Carlos and Grilli, Francesco

Name of the file: "B(T)_vs_Ic(A).txt"

Magnetic Field (T)	C
0	
1	
2	
3	

B(T) 2.75

Ic(B) 437.9

Losses in inf. stack of superconducting tapes under perpendicular magnetic field

Tape/Stack Data:

Thick(m) 1e-06
2w(m) 0.006
Ly(m) 0.0002
Ic(A) 437.9

Name of the file: "B_T.txt"

B (T)
0.0500
0.1000
0.2000

☑ Use Ic interp.

B(T)	Q(J/m/cycl
0.0500	0.0
0.1000	0.0
0.2000	0.0
0.3000	0.0
0.4000	0.0
0.5000	0.0
0.6000	0.0

* Modified Akima piecewise cubic Hermite interpolation. https://www.mathworks.com/help/matlab/ref/makima.html#mw_e8ee1c8c-2cc3-46c4-90c4-c3208804ff4e

* G. P. Mikitik, Y. Mawatari, A. T. S. Wan and F. Sirois, "Analytical Methods and Formulas for Modeling High Temperature Superconductors," in IEEE Transactions on Applied Superconductivity, vol. 23, no. 2 pp. 8001920-8001920, April 2013, Art no. 8001920.

* *Y. Mawatari, "Critical state of periodically arranged superconducting strip lines in perpendicular fields," Phys. Rev. B, Condens. Matter, vol. 54, no. 18, pp.13215-13221, Nov. 1996

Figure A.2: Graphical User Interface (GUI) of the application made to estimate AC losses in an infinite stack of superconducting tapes under perpendicular magnetic field based on analytical solutions.

$$\frac{Q}{Q_{\mathrm{c}}} = \left(\frac{L_y}{\pi\omega}\right)^2 h_0^2 \int_0^1 (1-2s)\ln\left[1+\frac{\sinh^2(\pi\omega/L_y)}{\cosh^2(\pi h_0 s)}\right] ds. \tag{A.2}$$

The equation allows computing the hysteretic AC loss in Joule per cycle per Meter in a superconducting strip in an infinite stack arrangement under perpendicular magnetic field, when the applied field H_a quasi-statically oscillate between $+H_0$ and $-H_0$, with $Q_c = \mu_0 I_c^2/\pi$ and $h_0 = \pi H_0/j_c d$. In these equations, j_c is the critical current density, I_{c} is the critical current, d is thickness of the strip, $2w$ is the width of the strip and L_y the separation between strips.

The MATLAB code of the function used to solve equation (A.2) is

```
function [Qi] = Q_YM_M_Fi(ic,H0,tape_w,thickness,separation)

w=tape_w/2;
Ic=ic;
Ho=H0;
```

```
Ly=separation;
d=thickness;

mu0=4*pi*(10^-7);
Qc=mu0*(Ic^2)/pi;

jc=Ic/(2*w*d);

ho=(pi*Ho)/(jc*d);

funQ = @(s) (1-2*s).*log(((sinh(pi*w/Ly)^2).
    /(cosh(ho*s).^2))+1);
Qi = Qc*((Ly/(pi*w))^2)*(ho^2)*integral(funQ,0,1);

end .
```

List of Figures

List of Tables

Bibliography

[1] A. Anisie, E. Bianco, H. Blanco, F. Boshell, X. Casals, J. Feng, C. Guadarrama, D. Hawila, S. Kang, A. Lopez-Pena, D. Nagpal, B. Parajuli, G. Pragada, G. Prakash, F. Rana, M. Renner, G. Sokhna Seck, E. Taibi, and A. Vaid, "World Energy Transitions Outlook 2022: 1.5°C Pathway," tech. rep., International Renewable Energy Agency (IRENA), Abu Dhabi, United Arab Emirates, 2022. ISBN: 978-92-9260-429-5.

[2] D. Hawila, F. Rana, A. Abou Ali, A. Khalid, C. Strinati, S. Diab, M. Munoz Cabre, D. Jacobs, and C. Toby, "Renewable energy targets in 2022: A guide to design," tech. rep., International Renewable Energy Agency (IRENA), Abu Dhabi, United Arab Emirates, 2022. ISBN: 978-92-9260-480-6.

[3] G. Prakash, H. Anuta, D. Gielen, and R. Gorini, "FUTURE OF WIND Deployment, investment, technology, grid integration and socio-economic aspects," tech. rep., International Renewable Energy Agency (IRENA), Abu Dhabi, United Arab Emirates, 2019. ISBN 978-92-9260-155-3.

[4] P. Veers, L. Sethuraman, and J. Keller, "Wind-Power Generator Technology Research Aims to Meet Global-Wind Power Ambitions," *Joule Cell*, vol. 4, pp. 1861–1863, Sept. 2020.

[5] "WIND ENERGY. Accomplishments & Midyear Performance Report: FISCAL YEAR 2022," 2022. [Online]. Available: https://www.nrel.gov/docs/fy22osti/83261.pdf.

[6] C. Lewis and J. Muller, “A Direct Drive Wind Turbine HTS Generator,” in *2007 IEEE Power Engineering Society General Meeting*, (Tampa, FL, USA), p. 10300962, June 2007. ISSN: 1932-5517.

[7] H. Polinder, J. A. Ferreira, B. B. Jensen, A. B. Abrahamsen, K. Atallah, and R. A. McMahon, “Trends in Wind Turbine Generator Systems,” *IEEE Journal of Emerging and Selected Topics in Power Electronics*, vol. 1, pp. 174–185, Sept. 2013.

[8] M. E. Khalil, “High temperature superconducting generator design for offshore wind turbine application,” in *2015 International Conference on Electrical Engineering and Information Communication Technology (ICEEICT)*, (Savar, Bangladesh), p. 15570570, IEEE, May 2015.

[9] E. J. Lantz, O. Roberts, J. Nunemaker, E. DeMeo, K. Dykes, and G. Scott, “Increasing Wind Turbine Tower Heights: Opportunities and Challenges,” Tech. Rep. NREL/TP-5000-73629, National Renewable Energy Laboratory (NREL), US, May 2019.

[10] S. S. Kalsi, “Superconducting Wind Turbine Generator Employing MgB2 Windings Both on Rotor and Stator,” *IEEE Transactions on Applied Superconductivity*, vol. 24, p. 5201907, Feb. 2014.

[11] G. Snitchler, B. Gamble, C. King, and P. Winn, “10 MW Class Superconductor Wind Turbine Generators,” *IEEE Transactions on Applied Superconductivity*, vol. 21, pp. 1089–1092, June 2011.

[12] J. Lloberas, A. Sumper, M. Sanmarti, and X. Granados, “A review of high temperature superconductors for offshore wind power synchronous generators,” *Renewable and Sustainable Energy Reviews*, vol. 38, pp. 404–414, May 2014.

[13] B. B. Jensen, N. Mijatovic, and A. B. Abrahamsen, “Development of superconducting wind turbine generators,” *Journal of Renewable and Sustainable Energy*, vol. 5, p. 023137, Mar. 2013.

[14] J. Frauenhofer, J. Grundmann, G. Klaus, and W. Nick, “Basic concepts, status, opportunities, and challenges of electrical machines utilizing high-temperature superconducting (HTS) windings,” *Journal of Physics: Conference Series*, vol. 97, p. 012189, 2008.

[15] I. K. Okakwu, P. E. Orukpe, and E. A. Ogujor, “Application of Superconducting Fault Current Limiter (SFCL) in Power Systems: A Review,” *European Journal of Engineering Research and Science*, vol. 3, pp. 28–32, July 2018.

[16] E. Berrospe-Juarez, V. M. R. Zermeno, F. Trillaud, A. Gavrilin, F. Grilli, D. V. Abraimov, D. K. Hilton, and H. W. Weijers, “Estimation of Losses in the (RE)BCO Two-Coil Insert of the NHMFL 32 T All-Superconducting Magnet,” *IEEE Transactions on Applied Superconductivity*, vol. 28, p. 4602005, Apr. 2018.

[17] C. C. Rong and P. N. Barnes, “Developmental Challenges of SMES Technology for Applications,” *IOP Conference Series: Materials Science and Engineering*, vol. 279, p. 012013, Dec. 2017.

[18] W. H. Fietz, M. J. Wolf, A. Preuss, R. Heller, and K.-P. Weiss, “High-Current HTS Cables: Status and Actual Development,” *IEEE Transactions on Applied Superconductivity*, vol. 26, p. 4800705, June 2016.

[19] I. Marino, A. Pujana, G. Sarmiento, S. Sanz, J. M. Merino, M. Tropeano, J. Sun, and T. Canosa, “Lightweight MgB2 superconducting 10 MW wind generator,” *Superconductor Science and Technology*, vol. 29, p. 024005, Dec. 2015.

[20] “INNOVATIVE WIND CONVERSION SYSTEMS (10-20MW) FOR OFFSHORE APPLICATIONS (INNWIND.EU),” Feb. 2018. [Online]. Available:http://www.innwind.eu/publications/deliverable-reports.

[21] A. Bergen, R. Andersen, M. Bauer, H. Boy, M. t. Brake, P. Brutsaert, C. Bührer, M. Dhallé, J. Hansen, H. ten Kate, J. Kellers, J. Krause, E. Krooshoop, C. Kruse, H. Kylling, M. Pilas, H. Pütz, A. Rebsdorf, M. Reckhard, E. Seitz, H. Springer, X. Song, N. Tzabar, S. Wessel, J. Wiezoreck,

T. Winkler, and K. Yagotyntsev, “Design and in-field testing of the world’s first ReBCO rotor for a 3.6 MW wind generator,” *Superconductor Science and Technology*, vol. 32, p. 125006, Oct. 2019.

[22] I. Kolchanova and V. Poltavets, “Superconducting generators for wind turbines,” in *2021 International Conference on Electrotechnical Complexes and Systems (ICOECS)*, (Ufa, Russian Federation), pp. 529–533, IEEE, Nov. 2021.

[23] R. Wesche, *Physical Properties of High-TemperatureSuperconductors*. United Kingdom: John Wiley & Sons, Ltd, 2015.

[24] M. Saruwatari, K. Yun, M. Iwakuma, K. Tamura, Y. Hase, Y. Sasamori, and T. Izumi, “Design Study of 15-MW Fully Superconducting Generators for Offshore Wind Turbine,” *IEEE Transactions on Applied Superconductivity*, vol. 26, p. 5206805, June 2016.

[25] T.-K. Hoang, L. Quéval, C. Berriaud, and L. Vido, “Design of a 20-MW Fully Superconducting Wind Turbine Generator to Minimize the Levelized Cost of Energy,” *IEEE Transactions on Applied Superconductivity*, vol. 28, p. 5206705, June 2018.

[26] Y. Li, F. Feng, Y. Li, P. Song, S. Zou, M. Wu, C. Gu, P. Zeng, and T. Qu, “Numerical Study on AC Loss Characteristics of REBCO Armature Windings in a 15-kW Class Fully HTS Generator,” *IEEE Transactions on Applied Superconductivity*, vol. 27, p. 5200206, June 2017.

[27] Y. Xu, L. An, B. Jia, and N. Maki, “Study on Electrical Design of Large-Capacity Fully Superconducting Offshore Wind Turbine Generators,” *IEEE Transactions on Applied Superconductivity*, vol. 31, p. 5201305, Aug. 2021.

[28] M. Zhang, M. Chudy, W. Wang, Y. Chen, Z. Huang, Z. Zhong, W. Yuan, J. Kvitkovic, S. V. Pamidi, and T. A. Coombs, “AC Loss Estimation of HTS Armature Windings for Electric Machines,” *IEEE Transactions on Applied Superconductivity*, vol. 23, p. 5900604, June 2013.

[29] V. Zermeño, F. Sirois, M. Takayasu, M. Vojenciak, A. Kario, and F. Grilli, “A self-consistent model for estimating the critical current of superconducting devices,” *Superconductor Science and Technology*, vol. 28, p. 085004, Aug. 2015.

[30] H. K. Onnes, “Further experiments with Liquid Helium. G. On the Electrical Resistance of Pure Metals, etc. VI. On the Sudden Change in the Rate at which the Resistance of Mercury Disappears.,” *KNAW, Proceedings*, vol. 14, pp. 818–821, 1911. Series Title: Boston Studies in the Philosophy of Science.

[31] D. Delft, “History and significance of the discovery of superconductivity by Kamerlingh Onnes in 1911,” *Physica C: Superconductivity*, vol. 479, pp. 30–35, Mar. 2012.

[32] W. Meissner and R. Ochsenfeld, “Ein neuer Effekt bei Eintritt der Supraleitfaehigkeit,” *Naturwissenschaften*, vol. 21, pp. 787–788, Nov. 1933.

[33] M. Wilson, *Superconducting Magnets*, vol. 2 of *Monographs on cryogenics*. Oxford University Press, 1983.

[34] A. A. Abrikosov, “On the magnetic properties of superconductors of the second group,” *Soviet Phys. JETP-USSR*, vol. 5, pp. 1174–1182, Dec. 1957.

[35] A. C. Rose-Innes and E. H. Rhoderick, *Introduction to Superconductivity*. Great Britain: Pergamon Press, second edition ed., 1994.

[36] J. G. Bednorz and K. A. Mueller, “Possible High Tc Superconductivity in the Ba - La- Cu- 0 System,” *Zeitschrift für Physik B Condensed Matter*, vol. 64, pp. 189–193, Apr. 1986.

[37] D. Larbalestier, A. Gurevich, D. M. Feldmann, and A. Polyanskii, “High-Tc superconducting materials for electric power applications,” *Nature*, vol. 414, pp. 368–377, 2001.

[38] W. T. Norris, “Calculation of hysteresis losses in hard superconductors carrying ac: isolated conductors and edges of thin sheets,” *Journal of Physics D: Applied Physics*, vol. 3, pp. 489–507, Apr. 1970.

[39] E. H. Brandt and M. Indenbom, "Type-II-superconductor strip with current in a perpendicular magnetic field," *Physical Review B*, vol. 48, pp. 12893–12906, Nov. 1993.

[40] Y. Mawatari, "Critical state of periodically arranged superconducting-strip lines in perpendicular fields," *Physical Review B*, vol. 54, pp. 13215–13221, Nov. 1996.

[41] Y. Mawatari, "Critical State in Superconducting Strip-Array Systems with Transport Current," in *Advances in Superconductivity IX*, (Japan), pp. 575–580, Springer-Verlag, Oct. 1997.

[42] G. P. Mikitik, Y. Mawatari, A. T. S. Wan, and F. Sirois, "Analytical Methods and Formulas for Modeling High Temperature Superconductors," *IEEE Transactions on Applied Superconductivity*, vol. 23, p. 8001920, Apr. 2013.

[43] L. Yingzhen, *Design of a superconducting DC wind generator*. Ph.D. dissertation, Karlsruhe Institute of Technology, Karlsruhe, Germany, Jan. 2018.

[44] F. Schreiner, *Development and test of a technology wind generator demonstrator with no insulation field coils applying high temperature superconductors*. Ph.D. dissertation, Karlsruhe Institute of Technology, Karlsruhe, Germany, Mar. 2022.

[45] N. Amemiya, S.-i. Murasawa, N. Banno, and K. Miyamoto, "Numerical modelings of superconducting wires for AC loss calculations," *Physica C: Superconductivity*, vol. 310, pp. 16–29, Dec. 1998.

[46] E. H. Brandt, "Superconductors of finite thickness in a perpendicular magnetic field: Strips and slabs," *PHYSICAL REVIEW B*, vol. 54, pp. 4246 – 4264, Aug. 1996.

[47] E. Pardo, J. Šouc, and L. Frolek, "Electromagnetic modelling of superconductors with a smooth current–voltage relation: variational principle and coils from a few turns to large magnets," *Superconductor Science and Technology*, vol. 28, p. 044003, Feb. 2015.

[48] V. Sokolovsky, L. Prigozhin, and A. B. Kozyrev, “Chebyshev spectral method for superconductivity problems,” *Supercond. Sci. Technol.*, vol. 33, p. 085008, July 2020.

[49] B. Shen, F. Grilli, and T. Coombs, “Overview of H-Formulation: A Versatile Tool for Modeling Electromagnetics in High-Temperature Superconductor Applications,” *IEEE Access*, vol. 8, pp. 100403–100414, 2020.

[50] H. Zhang, M. Zhang, and W. Yuan, “An efficient 3D finite element method model based on the T–A formulation for superconducting coated conductors,” *Superconductor Science and Technology*, vol. 30, p. 024005, Dec. 2016.

[51] R. Ando, R. Fujimoto, T. Nakayama, and M. Abe, “Development of a Design Method for Superconducting Electromagnets Using Racetrack Coils,” *IEEE Transactions on Applied Superconductivity*, vol. 18, pp. 1525–1528, June 2008.

[52] Z. Zhao, K. Liu, C. Wang, W. Zhang, J. Li, L. Han, X. Song, and G. Ma, “The Establishment of an Analytical Model for Coreless HTS Linear Synchronous Motor With a Generalized Racetrack Coil as the Secondary,” *IEEE Transactions on Applied Superconductivity*, vol. 29, p. 5203105, Aug. 2019.

[53] T. Gong, G. Ma, R. Wang, S. Li, K. Liu, and Z. Zhao, “Three-dimensional analysis of the magnetic fields and forces in a coreless HTS linear synchronous motor,” *Physica C: Superconductivity and its Applications*, vol. 568, p. 1353577, Jan. 2020.

[54] H. Zhang, P. Machura, K. Kails, H. Chen, and M. Mueller, “Dynamic loss and magnetization loss of HTS coated conductors, stacks, and coils for high-speed synchronous machines,” *Superconductor Science and Technology*, vol. 33, p. 084008, Aug. 2020.

[55] X. Xu, Z. Huang, W. Li, X. Huang, M. Wang, Z. Hong, and Z. Jin, “3D finite element modelling on racetrack coils using the homogeneous T-A formulation,” *Cryogenics*, vol. 119, p. 103366, Oct. 2021.

[56] V. M. R. Zermeño and F. Grilli, “3D modeling and simulation of 2G HTS stacks and coils,” *Superconductor Science and Technology*, vol. 27, p. 044025, Mar. 2014.

[57] X. Huang, Z. Huang, X. Xu, W. Li, and Z. Jin, “Effective 3-D FEM for large-scale high temperature superconducting racetrack coil,” *KoreaScience*, vol. 21, pp. 32–37, Sept. 2019.

[58] F. Liang, S. Venuturumilli, H. Zhang, M. Zhang, J. Kvitkovic, S. Pamidi, Y. Wang, and W. Yuan, “A finite element model for simulating second generation high temperature superconducting coils/stacks with large number of turns,” *Journal of Applied Physics*, vol. 122, p. 043903, July 2017.

[59] J. Rhyner, “Magnetic properties and AC-losses of superconductors with power law current—voltage characteristics,” *Physica C*, vol. 212, pp. 292–300, July 1993.

[60] E. Berrospe-Juarez, V. M. R. Zermeño, F. Trillaud, and F. Grilli, “Real-time simulation of large-scale HTS systems: multi-scale and homogeneous models using the T–A formulation,” *Superconductor Science and Technology*, vol. 32, p. 065003, Apr. 2019.

[61] F. Grilli, E. Pardo, A. Morandi, F. Gömöry, M. Solovyov, V. M. R. Zermeño, R. Brambilla, T. Benkel, and N. Riva, “Electromagnetic Modeling of Superconductors With Commercial Software: Possibilities With Two Vector Potential-Based Formulations,” *IEEE Transactions on Applied Superconductivity*, vol. 31, p. 5900109, Jan. 2021.

[62] V. M. R. Zermeno, A. B. Abrahamsen, N. Mijatovic, B. B. Jensen, and M. P. Sørensen, “Calculation of alternating current losses in stacks and coils made of second generation high temperature superconducting tapes for large scale applications,” *Journal of Applied Physics*, vol. 114, p. 173901, Nov. 2013.

[63] E. Berrospe-Juarez, F. Trillaud, V. M. R. Zermeño, and F. Grilli, “Advanced electromagnetic modeling of large-scale high-temperature superconductor systems based on H and T-A formulations,” *Superconductor Science and Technology*, vol. 34, p. 044002, Feb. 2021.

[64] B. Sjodin, “Using Curvilinear Coordinates,” Nov. 2021. [Online]. Available: https://www.comsol.com/blogs/using-curvilinear-coordinates/.

[65] P. Zhou, G. Ma, and L. Quéval, “Transition frequency of transport ac losses in high temperature superconducting coated conductors,” *Journal of Applied Physics*, vol. 126, p. 063901, Aug. 2019.

[66] A. Musso, M. Breschi, P. L. Ribani, and F. Grilli, “Analysis of AC Loss Contributions From Different Layers of HTS Tapes Using the A-V Formulation Model,” *IEEE Transactions on Applied Superconductivity*, vol. 31, p. 5900411, Mar. 2021.

[67] P. Zhou, C. Wang, H. Qian, L. Queval, Z. Luo, Y. Deng, J. Li, Y. Li, and G. Ma, “Frequency-Dependent Transport AC Losses of Coated Superconductors Up To Tens of Kilohertz,” *IEEE Transactions on Applied Superconductivity*, vol. 29, p. 8201705, Aug. 2019.

[68] K. Kajikawa, T. Hayashi, R. Yoshida, M. Iwakuma, and K. Funaki, “Numerical evaluation of AC losses in HTS wires with 2D FEM formulated by self magnetic field,” *IEEE Transactions on Applied Superconductivity*, vol. 13, pp. 3630–3633, June 2003. Conference Name: IEEE Transactions on Applied Superconductivity.

[69] R. Pecher, M. Mcculloch, S. Chapman, L. Prigozhin, and C. Elliott, “3D-modelling of bulk type-II superconductors using unconstrained H-formulation,” *Proc. 6th EUCAS, Sorrento, Italy*, Sept. 2003.

[70] R. Brambilla, F. Grilli, and L. Martini, “Development of an edge-element model for AC loss computation of high-temperature superconductors,” *Superconductor Science and Technology*, vol. 20, pp. 16–24, Nov. 2006.

[71] Z. Hong, A. M. Campbell, and T. A. Coombs, “Numerical solution of critical state in superconductivity by finite element software,” *Superconductor Science and Technology*, vol. 19, pp. 1246–1252, Oct. 2006.

[72] B. Shen, F. Grilli, and T. Coombs, “Review of the AC loss computation for HTS using H formulation,” *Supercond. Sci. Technol.*, vol. 33, no. 3, p. 033002, 2020.

[73] V. M. Rodriguez Zermeno, *Computation of Superconducting Generators for Wind Turbine Applications*. Ph.D. dissertation, Technical University of Denmark (DTU), Lyngby, Denmark, Mar. 2012.

[74] E. Pardo, J. Šouc, and J. Kováč, “AC loss in ReBCO pancake coils and stacks of them: modelling and measurement,” *Superconductor Science and Technology*, vol. 25, p. 035003, Jan. 2012.

[75] F. Grilli, F. Sirois, V. M. R. Zermeño, and M. Vojenčiak, “Self-Consistent Modeling of the Ic of HTS Devices: How Accurate do Models Really Need to Be?,” *IEEE Transactions on Applied Superconductivity*, vol. 24, p. 8000508, Dec. 2014. Conference Name: IEEE Transactions on Applied Superconductivity.

[76] A. Abrahamsen, N. Magnusson, B. Jensen, and M. Runde, “Large Superconducting Wind Turbine Generators,” *Energy Procedia*, vol. 24, pp. 60–67, 2012.

[77] Y. Liu, J. Ou, F. Grilli, F. Schreiner, V. M. R. Zermeno, M. Zhang, and M. Noe, “Comparison of 2D simulation models to estimate the critical current of a coated superconducting coil,” *Superconductor Science and Technology*, vol. 32, p. 014001, Nov. 2018.

[78] L. Rossi and C. Senatore, “HTS Accelerator Magnet and Conductor Development in Europe,” *Instruments*, vol. 5, p. 8, Feb. 2021.

[79] M. P. Oomen, M. Leghissa, N. Proelss, and H. Neumueller, “Transposed-Cable Coil & Saddle Coils of HTS for Rotating Machines: Test Results at 30 K,” *IEEE Transactions on Applied Superconductivity*, vol. 19, pp. 1633–1638, June 2009.

[80] C. R. Vargas-Llanos, S. Lengsfeld, M. Noe, T. Arndt, and F. Grilli, “Influence of Coil Position on AC Losses of Stator Superconducting Windings of a

Synchronous Machine for a 10 MW Wind Turbine," *IEEE Transactions on Applied Superconductivity*, vol. 31, p. 5206509, Oct. 2021.

[81] T. Rummel, M. Nagel, V. Bykov, D. Birus, A. Carls, C. P. Dhard, E. Köster, T. Mönnich, K. Riße, M. Schneider, and H.-S. Bosch, "Commissioning Results of the Superconducting Magnet System of Wendelstein 7-X," *IEEE Transactions on Applied Superconductivity*, vol. 27, p. 4200307, June 2017.

[82] A. Almagri, D. Anderson, F. Anderson, P. Probert, J. Shohet, and J. Talmadge, "A helically symmetric stellarator (HSX)," *IEEE Transactions on Plasma Science*, vol. 27, pp. 114–115, Feb. 1999.

[83] T. Benkel, M. Lao, Y. Liu, E. Pardo, S. Wolfstädter, T. Reis, and F. Grilli, "T–A-Formulation to Model Electrical Machines With HTS Coated Conductor Coils," *IEEE Transactions on Applied Superconductivity*, vol. 30, p. 5205807, Sept. 2020.

[84] X. Huang, Z. Huang, X. Xu, L. Wang, W. Li, and Z. Jin, "A Fully Coupled Numerical Method for Coated Conductor HTS Coils in HTS Generators," *IEEE Transactions on Applied Superconductivity*, vol. 30, p. 5206406, June 2020.

[85] Y. Yang, H. Yong, X. Zhang, and Y. Zhou, "Numerical Simulation of Superconducting Generator Based on the T–A Formulation," *IEEE Transactions on Applied Superconductivity*, vol. 30, p. 5207611, Dec. 2020.

[86] Y. Gao, W. Wang, X. Wang, H. Ye, Y. Zhang, Y. Zeng, Z. Huang, Q. Zhou, X. Liu, Y. Zhu, and Y. Lei, "Design, Fabrication, and Testing of a YBCO Racetrack Coil for an HTS Synchronous Motor With HTS Flux Pump," *IEEE Transactions on Applied Superconductivity*, vol. 30, p. 4601005, June 2020.

[87] Y. Liu, M. Noe, J. Ou, P. Breining, M. Veigel, and M. Doppelbauer, "Measurement of Magnetic Materials at Room and Cryogenic Temperature for Their Application to Superconducting Wind Generators," *IEEE Transactions on Applied Superconductivity*, vol. 28, p. 5206006, Apr. 2018.

[88] D. Hazelton, “Status of 2G HTS Wire for Electric Power Applications,” Apr. 2013. [Online]. Available: http://www.superpower-inc.com/system/files/2013_0426+CIGRE+WG38+Wksp_SuperPower.pdf.

[89] S. Zou, V. M. R. Zermeno, and F. Grilli, “Simulation of Stacks of High-Temperature Superconducting Coated Conductors Magnetized by Pulsed Field Magnetization Using Controlled Magnetic Density Distribution Coils,” *IEEE Transactions on Applied Superconductivity*, vol. 26, p. 8200705, Apr. 2016.

[90] A. Fatemi, D. M. Ionel, N. A. O. Demerdash, D. A. Staton, R. Wrobel, and Y. C. Chong, “A computationally efficient method for calculation of strand eddy current losses in electric machines,” in *2016 IEEE Energy Conversion Congress and Exposition (ECCE)*, Sept. 2016.

[91] F. Chauvicourt, P. Romanazzi, D. Howey, A. Dziechciarz, C. Martis, and C. T. Faria, “Review of Multidisciplinary Homogenization Techniques applied to Electric Machines,” in *Eleventh International Conference on Ecological Vehicles and Renewable Energies (EVER)*, p. 9, Apr. 2016.

[92] P. Nirmal, “How to Analyze an Induction Motor: A TEAM Benchmark Model.” [Online]. Available: https://www.comsol.jp/blogs/how-to-analyze-an-induction-motor-a-team-benchmark-model/.

[93] Y. Liu, *Design of a superconducting DC wind generator*. Ph.D. dissertation, Karlsruhe Institute of Technology, Karlsruhe, Germany, Jan. 2018.

[94] H. ter Brake and G. Wiegerinck, “Low-power cryocooler survey,” *Cryogenics*, vol. 42, pp. 705–718, Oct. 2002.

[95] F. Grilli, E. Pardo, A. Stenvall, D. N. Nguyen, Weijia Yuan, and F. Gomory, “Computation of Losses in HTS Under the Action of Varying Magnetic Fields and Currents,” *IEEE Transactions on Applied Superconductivity*, vol. 24, p. 8200433, Feb. 2014.

[96] R. Radebaugh, “Cryocoolers: the state of the art and recent developments,” *Journal of Physics: Condensed Matter*, vol. 21, p. 164219, Mar. 2009.

[97] R. Gupta, M. Anerella, J. Cozzolino, J. Escallier, G. Ganetis, M. Harrison, and P. Wanderer, "Next generation IR magnets for hadron colliders," *IEEE Transactions on Applied Superconductivity*, vol. 13, pp. 1351–1354, June 2003.

[98] G. Kirby, L. Rossi, A. Badel, M. Bajko, A. Ballarino, L. Bottura, M. Dhallé, M. Durante, P. Fazilleau, J. Fleiter, W. Goldacker, E. Härö, J. Himbele, A. Kario, S. Langeslag, C. Lorin, J. Murtzomaki, J. van Nugteren, G. de Rijk, T. Salmi, C. Senatore, A. Stenvall, P. Tixador, A. Usoskin, G. Volpini, Y. Yang, and N. Zangenberg, "Status of the Demonstrator Magnets for the EuCARD-2 Future Magnets Project," *IEEE Transactions on Applied Superconductivity*, vol. 26, p. 4003307, Apr. 2016.

[99] J. van Nugteren, G. Kirby, J. Murtomäki, G. DeRijk, L. Rossi, and A. Stenvall, "Toward REBCO 20 T+ Dipoles for Accelerators," *IEEE Transactions on Applied Superconductivity*, vol. 28, p. 4008509, June 2018.

[100] C. Paz-Soldan, "Non-planar coil winding angle optimization for compatibility with non-insulated high-temperature superconducting magnets," *Journal of Plasma Physics*, vol. 86, p. 815860501, Oct. 2020.

[101] J. S. Murtomäki, J. van Nugteren, A. Stenvall, G. Kirby, and L. Rossi, "3-D Mechanical Modeling of 20 T HTS Clover Leaf End Coils—Good Practices and Lessons Learned," *IEEE Transactions on Applied Superconductivity*, vol. 29, p. 4004608, Aug. 2019.

[102] J. v. Nugteren, G. A. Kirby, G. d. Rijk, L. Rossi, H. H. J. t. Kate, and M. M. J. Dhallé, "Study of a 5 T Research Dipole Insert-Magnet Using an Anisotropic ReBCO Roebel Cable," *IEEE Transactions on Applied Superconductivity*, vol. 25, pp. 1–5, June 2015.

[103] G. Nielsen, N. Zangenberg, D. Hazelton, N. Hauge, B. R. Nielsen, S. P. Møller, and A. Baurichter, "Dipole Magnet from High Tc Superconductor," *Physics Procedia*, vol. 36, pp. 824–829, 2012.

[104] M. Durante, C. Lorin, T. Lecrevisse, M. Segreti, G. Kirby, and J. Van Nugteren, “Manufacturing of the EuCARD2 Roebel-Based Cos-Theta Coils at CEA Saclay,” *IEEE Transactions on Applied Superconductivity*, vol. 30, p. 4602505, June 2020.

[105] M. Takayasu, L. Chiesa, L. Bromberg, and J. V. Minervini, “HTS twisted stacked-tape cable conductor,” *Superconductor Science and Technology*, vol. 25, p. 014011, Jan. 2012.

[106] G. Celentano, A. Vannozzi, G. De Marzi, M. Marchetti, A. Augieri, A. Di Zenobio, F. Fabbri, L. Muzzi, A. Rufoloni, and A. della Corte, “Bending Behavior of HTS Stacked Tapes in a Cable-in-Conduit Conductor With Twisted Al-Slotted Core,” *IEEE Transactions on Applied Superconductivity*, vol. 29, p. 4801205, Aug. 2019.

[107] M. Takayasu, “Development of REBCO Twisted Stacked-Tape Cables for Magnet Application,” May 2014. [Online]. Available: https://indico.cern.ch/event/308828/contributions/1680713/attachments/589814/811821/WAMHTS-1_Takayasu.pdf.

[108] A. Molodyk, S. Samoilenkov, A. Markelov, P. Degtyarenko, S. Lee, V. Petrykin, M. Gaifullin, A. Mankevich, A. Vavilov, B. Sorbom, J. Cheng, S. Garberg, L. Kesler, Z. Hartwig, S. Gavrilkin, A. Tsvetkov, T. Okada, S. Awaji, D. Abraimov, A. Francis, G. Bradford, D. Larbalestier, C. Senatore, M. Bonura, A. E. Pantoja, S. C. Wimbush, N. M. Strickland, and A. Vasiliev, “Development and large volume production of extremely high current density YBa2Cu3O7 superconducting wires for fusion,” *Scientific Reports*, vol. 11, p. 2084, Dec. 2021.

[109] Fujikura-Ltd., “Introduction of Fujikura RE-based High-Temperature Superconductor,” June 2022. https://www.fujikura.co.jp/eng/products/newbusiness/superconductors/01/superconductor.pdf, Last accessed on 11-08-2022.

[110] D. Liu, J. Xia, H. Yong, and Y. Zhou, “Estimation of critical current distribution in $\mathrm{Bi}_2\mathrm{Sr}_2\mathrm{CaCu}_2\mathrm{O}_x$ cables and coils using a self-consistent

model," *Superconductor Science and Technology*, vol. 29, p. 065020, May 2016.

[111] T. Gong, G. Ma, L. Xiao, J. Li, P. Zhou, P. Xie, and B. Liu, "Critical Current Estimation of HTS Coil Considering the Tape Inhomogeneity and Different Criteria," *IEEE Transactions on Applied Superconductivity*, vol. 32, p. 4601505, Sept. 2022.

[112] T. Matsushita, *Flux Pinning in Superconductors*, vol. 178 of *Springer Series in Solid-State Sciences*. Berlin, Germany: Springer Berlin Heidelberg, 2nd ed., 2014.

[113] Yinshun Wang, Xiaojin Guan, and Jingshu Dai, "Review of AC Loss Measuring Methods for HTS Tape and Unit," *IEEE Transactions on Applied Superconductivity*, vol. 24, p. 9002306, Oct. 2014.

[114] H. Zhang, Z. Wen, F. Grilli, K. Gyftakis, and M. Mueller, "Alternating Current Loss of Superconductors Applied to Superconducting Electrical Machines," *Energies*, vol. 14, p. 2234, Apr. 2021.

[115] L. Frolek and J. Šouc, "Measurement of AC transport current loss in different kinds of superconducting tapes and wires in liquid helium," *Superconductor Science and Technology*, vol. 24, p. 105016, Sept. 2011.

[116] Y. Yang, T. Hughes, C. Beduz, D. M. Spiller, R. G. Scurlock, and W. T. Norris, "The influence of geometry on self-field AC losses of Ag sheathed PbBi2223 tapes," *Physica C: Superconductivity*, vol. 256, pp. 378–386, Jan. 1996.

[117] F. Grilli and S. P. Ashworth, "Measuring transport AC losses in YBCO-coated conductor coils," *Superconductor Science and Technology*, vol. 20, pp. 794–799, June 2007.

[118] J. Šouc, E. Pardo, M. Vojenčiak, and F. Gömöry, "Theoretical and experimental study of AC loss in high temperature superconductor single pancake coils," *Superconductor Science and Technology*, vol. 22, p. 015006, Nov. 2008.

[119] J. J. Rabbers, *AC loss in superconducting tapes and coils*. Ph.D. dissertation, University of Twente, Twente, Netherlands, Oct. 2001.

[120] J.-H. Kim, C. H. Kim, G. Iyyani, J. Kvitkovic, and S. Pamidi, “Transport AC Loss Measurements in Superconducting Coils,” *IEEE Transactions on Applied Superconductivity*, vol. 21, pp. 3269–3272, June 2011.

[121] H. Okamoto, F. Sumiyoshi, K. Miyoshi, and Y. Suzuki, “The Nitrogen Boil-Off Method for Measuring AC Losses in HTS Coils,” *IEEE Transactions on Applied Superconductivity*, vol. 16, pp. 105–107, June 2006.

[122] J. Eikelboom, “Test results of an apparatus for calorimetric measurement of AC losses in superconductors,” *IEEE Transactions on Magnetics*, vol. 28, pp. 817–821, Jan. 1992.

[123] G. Coletta, L. Gherardi, F. Gomory, E. Cereda, V. Ottoboni, D. Daney, M. Maley, and S. Zannella, “Application of electrical and calorimetric methods to the AC loss characterization of cable conductors,” *IEEE Transactions on Applied Superconductivity*, vol. 9, pp. 1053–1056, June 1999.

[124] D. Kottonau, “Untersuchung der Machbarkeit eines dreiphasigen CroCo-Leitersystems für supraleitende Energiekabel,” Master’s thesis, University of Duisburg-Essen, Duisburg, Germany, Oct. 2018.

[125] D. Kottonau, M. Wolf, W. Fietz, J. Stammen, and H. Hirsch, “Feasibility of ultra-compact HTS CrossConductor based Power Transmission Cables,” *Journal of Physics: Conference Series*, vol. 1559, p. 012084, June 2020.

[126] H. Okamoto, H. Hayashi, F. Sumiyoshi, M. Iwakuma, T. Izumi, Y. Yamada, and Y. Shiohara, “Nitrogen boil-off method of measuring AC losses in YBCO coils,” *Physica C: Superconductivity and its Applications*, vol. 463-465, pp. 795–797, Oct. 2007.

[127] H. Okamoto, H. Hayashi, A. Tomioka, M. Konno, M. Owa, A. Kawagoe, F. Sumiyoshi, M. Iwakuma, K. Suzuki, T. Izumi, Y. Yamada, and Y. Shiohara, “AC loss properties in YBCO model coils for loss reduction,” *Physica C: Superconductivity*, vol. 468, pp. 1731–1733, Sept. 2008.

[128] S. Kawabata, R. Motomura, and T. Hirayama, “AC Loss Measurement of High-Tc Superconducting Coils Wound With Stacked Conductors,” *IEEE Transactions on Applied Superconductivity*, vol. 23, p. 5900904, June 2013.

[129] J. Lu, H. Bai, A. V. Gavrilin, G. Zhang, W. D. Markiewicz, and H. W. Weijers, “AC Losses of ReBCO Pancake Coils Measured by a Calorimetric Method,” *IEEE Transactions on Applied Superconductivity*, vol. 25, p. 4701005, June 2015.

[130] W. Funakoshi, T. Hirayama, and S. Kawabata, “Measurement of AC Loss Characteristics of HTS Sample Coils Under the Conditions Assumed for use in Power Electronics Devices,” *IEEE Transactions on Applied Superconductivity*, vol. 32, p. 5901104, Sept. 2022.

[131] J. Weisend II, ed., *Cryostat Design: Case Studies, Principles and Engineering*. International Cryogenics Monograph Series, Switzerland: Springer International Publishing, 2016.

[132] I. Lake Shore Cryotronics, “Appendix I: Cryogenic Reference Tables.” https://www.lakeshore.com/docs/default-source/product-downloads/literature/lstc_appendixi_l.pdf?sfvrsn=5f2ab85b_4, Last accessed on 27-06-2022.

[133] R. L. Garwin, “Calculation of Heat Flow in a Medium the Conductivity of which Varies with Temperature,” *Review of Scientific Instruments*, vol. 27, pp. 826–828, Oct. 1956.

[134] H. S. Lee, *Thermal Design: Heat Sinks, Thermoelectrics, Heat Pipes, Compact Heat Exchangers, and Solar Cells*. Hoboken, New Jersey: John Wiley & Sons, Inc., 1 ed., Nov. 2010.

[135] “NALL mass flowmeters,” Product manual 111-122010, Teledyne Hastings Instruments, Hampton, Virginia, USA, Dec. 2022. Revision G.

[136] J. R. Taylor, *An Introduction to Error Analysis: The Study of Uncertainties in Physical Measurements*. Mill Valley, California, USA: University Science Books, 1st ed., 1982.